KU LEUVEN

ARENBERG DOCTORAL SCHOOL
FACULTY OF ENGINEERING SCIENCE

Fatigue crack initiation and facet formation in Ti-6Al-4V wires

Joris EVERAERTS

Supervisors:
Prof. dr. ir. Martine Wevers
Prof. dr. ir. Bert Verlinden

Dissertation presented in partial
fulfilment of the requirements for the
degree of Doctor of Engineering
Science (PhD): Materials Engineering

February 2017

FATIGUE CRACK INITIATION AND FACET FORMATION IN TI-6AL-4V WIRES

Joris EVERAERTS

Supervisor:
Prof. dr. ir. Martine Wevers
Co-supervisor:
Prof. dr. ir. Bert Verlinden

Members of the Examination Committee:
Prof. dr. ir. Patrick Wollants, Chairman
Prof. dr. ir. Ludo Froyen
Prof. dr. ir. Thomas Pardoen
Prof. dr. ir. Marc Seefeldt
Prof. dr. ir. Patricia Verleysen

Dissertation presented in
partial fulfilment of the
requirements for the degree
of Doctor of Engineering
Science (PhD): Materials
Engineering

February 2017

Uitgegeven in eigen beheer, Joris Everaerts, Kasteelpark Arenberg 44 bus 2450, B-3001 Heverlee (Belgium)

Preface

“La science, mon garçon, est faite d'erreurs, mais d'erreurs qu'il est bon de commettre, car elles mènent peu à peu à la vérité.”

Jules Verne

It is interesting how the first part of a thesis is the last part you actually write. Because I have now experienced the whole process first-hand, I would like to start this preface somewhat unconventionally by attempting to describe what it felt like to do a PhD. Roughly four and a half years ago, I boarded the last wagon of a train to an unknown destination. As soon as I had stepped in, the doors closed behind me and the train slowly started accelerating out of the station. After some time, I got curious about where I was heading. In order to find out where exactly this train was taking me, my only option was to try to reach the locomotive at the front. Unfortunately, I soon figured out that each door in between compartments was locked. Every time I wanted to progress to the next compartment, I had to find the key that could open the door. With some guidance from other passengers, I managed to slowly make my way through this curious vehicle. I could see other trains through the windows, running on parallel tracks. Some were overtaking me, while others were slower. More worryingly, however, a few trains appeared to have derailed and crashed along the way. At this point, I started noticing that the train I was on was also gaining speed. After a brief moment of panic, and considering pulling the emergency brake, I decided that I had to redouble my efforts to get to the front of the train before it would crash, even though opening the compartment doors was becoming more and more challenging as I progressed. In spite of these difficulties, I finally managed to break through the final door, and I entered the locomotive, only to find that there was no driver. Then the truth finally dawned on me: there was no final destination. My purpose on this train was to prepare myself while I was making my way to the locomotive, so that once I reached it I would be able to figure out how the train could be stopped. After accepting this peculiar faith, and after a period of hard work, I have now finally gotten the train to come to a complete standstill. The end result of this educational journey is the thesis you are now reading.

I wouldn’t have been able to finish this work without the guidance of my promotor, **Prof. Martine Wevers**. In fact, I wouldn’t even have been able to start it if she hadn’t presented me with the opportunity. Therefore, I would like to express my sincere gratitude to her, for giving me the proverbial train ticket at a time when I thought all trains had left the station. Her expertise in the field of fatigue fracture was one of the things that kept me on track. At the same time, she gave me a lot of freedom to explore my own ideas, which I know is not always the case during a PhD. I experienced this freedom as being the result of a high amount of trust, for which I would also like to thank her.

In a way, this thesis is a conglomeration of fatigue failure on the one hand and crystallographic texture on the other hand. Because of his expertise on the latter subject, I have been very fortunate that **Prof. Bert Verlinden** agreed to be my co-promotor. He was very closely involved with my work, and I would also like to thank him for his patience and advice during my PhD.

Besides my promotors, I would like to thank the other members of my supervisory committee: **Prof. Thomas Pardoen**, for his input on, for example, mechanical behaviour and for coordinating the IAP network, and **Prof. Ludo Froyen**, for his constructive comments on my work and for sometimes providing a different point of view. I am very grateful to them for helping me to improve this thesis in several ways. Next, I would like to express my gratitude to the rest of my examination committee: **Prof. Marc Seefeldt**, for giving me opportunities to present my work at GLADD and ASTRO meetings and for the detailed comments regarding, for example, dislocation mechanisms, and **Prof. Patricia Verleysen**, for always showing interest in my results and for the stimulating discussions at several meetings. I would also like to thank the chairman of my examination committee, **Prof. Patrick Wollants.** It can be difficult to stay motivated during a PhD, which is why I'm grateful that all of these people showed appreciation for my work.

There are a lot of colleagues that I would like to mention. You could say that they were the trains running on parallel tracks, although I'm probably taking this train analogy a bit too far. I will start with the people with whom I shared an office during my PhD: **Ioannis, Nikos, Katie, Sneha, Ilya, Yuliya, Franziska, Masoud** and **Panagiotis**. I would like to thank you for all the laughs, support and advice. Next, I am incredibly grateful to have met **Gokula, Diarmuid** and **Xiaodong**. We all started a PhD more or less around the same time, which means that we also went through all the different stages around the same time. I won't ever forget the scientific and non-scientific discussions, the mutual complaining and sharing of despair, and the overall support that I got from you. All three of you have reached the front of your respective trains, and I am confident that you will soon manage to stop them successfully. I would also like to thank **Gregory, Greet, Helge, Jeroen, Ling, Xiebin, Philip, Bram, Annabel, Lore, Stijn, Lieven, Lieven, Bey, Nicholas, Nicolò, Nachiketa, Sam, Karel, Lesley, Lies, Iñigo, Andrea, Andrea, Maria, Mahoor, Gijs, Laurien, Sabrina, Amy, Jurgen, Pavel, Katleen, Delphine, Steve, Jolien, Suraj, Gaurav, Matteo, Thomas, Lukas, Pierre, Bensu, Aljaz and Fei,** for either helping me with my experiments, for the frequent or sporadic small talk, or for the occasional culinary discoveries. It has been an enriching experience, and I wish you all the best of luck in the future. Additionally, I would like to thank **Prof. Jef Vleugels** and **Prof. Kim Vanmeensel**, with whom I might have done a PhD if things had gone differently.

Next, I would like to express my gratitude to a group of people that unfortunately is often not mentioned, even though they are a crucial part of the department: the technical staff. I’m pushing the train story to its limits, but you could say that without these people the train engines would simply not work. The research in this thesis would not have been possible without the help of **Paul, Tom, Britt, Iris, Bart, Kris, Pieter, Louis, Joop, Gert, Eddy, Johan, Wout, Danny** and **Marc**. I would also like to thank the administrative staff: **Huberte, Nadine, Kevin, Jennifer, Mia, Mieke** and **Dirk**.

Ik zou graag mijn ouders bedanken voor hun onvoorwaardelijke steun in alles wat ik doe. Daarnaast wil ik bij uitbreiding ook mijn hele ***familie*** *bedanken voor hun steun, maar ook om af en toe te proberen achterhalen waar ik zoal mee bezig was in mijn doctoraat. Hopelijk heb ik het min of meer kunnen uitleggen tijdens mijn publieke verdediging. Zo niet, dan probeer ik het nog wel eens op een luie zondag of op een volgend familiefeest.*

Finally, I would like to address you, the reader, directly. During writing, you tend to realise that, most probably, only very few people will actually read your PhD thesis. However, I hope that my thesis will not be subjected to any floccinaucinihilipilification for this reason, and I sincerely hope you will get something worthwhile out of it. In fact, if you are reading this, the chances are high that you are also doing a PhD, in which case I can only recommend that you try to appreciate the journey, rather than worrying about the destination. As for me, I will be trying to do the same thing when I board the next train.

Joris Everaerts

Leuven, February 2017

Abstract

In Ti-6Al-4V, fatigue cracks can nucleate internally instead of at the surface. Internal or subsurface cracks in titanium alloys are found to initiate at faceted features, which can be seen on the fracture surface after failure. These facets are fractured primary α (hcp) grains, which have broken in a very planar manner. The main purpose of this work is to study internal fracture in drawn Ti-6Al-4V wires, which has not been done before, since all published studies use forged or rolled samples. Fatigue tests with load ratio R=0.1 and a frequency of 60 Hz have been performed on wires with average α grain sizes of approximately 1, 2, 5 and 10 µm. In total, 50 samples were successfully tested.

Four samples broke due to an internally initiated crack after testing at a maximum stress of 750 MPa: three samples with average alpha grain size 5 µm, which failed after 2.6 x 10^7, 5.7 x 10^7 and 9.6 x 10^7 cycles, and one sample with average alpha grain size 10 µm, which failed after 7.6 x 10^6 cycles. In general, an increase in grain size resulted in lower fatigue lives. In the four samples with internal crack initiation, a cluster of facets was observed at the initiation site on the fracture surface. The projected area size of the facet-containing area was not related to the fatigue life, and the estimated threshold stress intensity factor range was between 6 and 8 $\text{MPa}\sqrt{\text{m}}$. The actual surface area, taking into account the roughness, was correlated to the fatigue life. The facets were not smooth, but showed some nano-roughness with linear markings. As a result of the crystallographic texture, the facets were highly inclined, at angles mostly between 50° and 70°. Nearly all facets were parallel to a prismatic lattice plane. The linear markings on these facets were parallel to the direction of the prismatic slip system, which means that facet formation most likely occurred by a prismatic slip band mechanism. One anomalous facet was observed in the sample with an average grain size of 10 µm. This facet coincided with a near-basal plane, and displayed a fan-shaped pattern instead of linear markings, which indicates that a cleavage mechanism took place. These observations suggest that both a slip-based and a cleavage-based mechanism are possible, depending on the grain size, local texture and possibly other parameters.

A local comparison of Taylor factors showed that the Taylor factor of each faceted grain had a tendency towards being higher than the Taylor factors of its corresponding neighbouring grains. It is suggested that the Taylor factor may be used to distinguish between plastically hard and soft grain orientations, and therefore could be capable of explaining the stress distribution between grains, which is the root cause for facet formation. Fracture surface cross-sections revealed secondary facets, which in some cases extended through more than one grain. Short crack growth through a grain boundary occurred when two compatible slip systems were

present in these grains. This compatibility could be expressed by calculating alignment factors.

Additionally, a limited number of dwell fatigue tests have been performed, with a hold time of 30 or 120 s at maximum load. Introducing a hold time at maximum load drastically reduced the amount of cycles to failure by two to three orders of magnitude compared to regular fatigue tests, and promoted surface crack initiation. This was caused by strain accumulation due to cold creep, which occurred during each maximum load hold. A recovery process took place during each minimum load hold, which caused an increased initial strain rate during each following maximum load hold.

Samenvatting

In Ti-6Al-4V kunnen vermoeiingsscheuren intern ontstaan in plaats van aan het oppervlak. In titaanlegeringen gebeurt deze interne scheurinitiatie door de vorming van facetten, die na faling op het breukoppervlak waargenomen kunnen worden. Deze facetten zijn primaire α (hdp) korrels, die op een planaire manier gebroken zijn. Het hoofddoel van dit onderzoek is het bestuderen van interne scheurinitiatie in getrokken Ti-6Al-4V draden. Het vermoeiingsgedrag van dit soort draden was nog niet onderzocht, aangezien er meestal gewerkt wordt met gewalst of gesmeed Ti-6Al-4V. De vermoeiingstesten werden uitgevoerd op draden met een gemiddelde primaire α korrelgrootte van 1, 2, 5 en 10 µm, met een spanningsratio van 0.1 en een frequentie van 60 Hz. In totaal werden 50 draden succesvol getest.

Vier monsters vertoonden interne scheurinitiatie. Drie van deze monsters hadden een gemiddelde α korrelgrootte van 5 µm en zijn gebroken na 2.6 x 10^7, 5.7 x 10^7 en 9.6 x 10^7 cycli. Het andere monster had een gemiddelde α korrelgrootte van 10 µm en is gebroken na 7.6 x 10^6 cycli. Over het algemeen resulteerde een verhoging van de korrelgrootte in een verlaging van de levensduur. Op de breukoppervlakken van de vier monsters met interne scheurinitiatie was een gebied met facetten aanwezig op de plaats van de scheurinitiatie. De grootte van het geprojecteerde oppervlak van dit gebied was niet gecorreleerd met de levensduur, en de geschatte drempelwaarde van het bereik van de spanningsintensiteitsfactor voor lange scheurgroei was tussen 6 en 8 MPa√m. De werkelijke oppervlakte van dit gebied, die ook de oppervlakteruwheid in rekening brengt, was wel gecorreleerd met de levensduur. De facetten vertoonden ruwheid op de nanoschaal, met lineaire markeringen. Als gevolg van de kristallografische textuur lagen de facetvlakken onder steile hoeken, voornamelijk tussen 50° en 70°. Bijna alle facetvlakken waren parallel met een prismatisch kristalvlak. De lineaire markeringen op de facetten waren evenwijdig met de sliprichting voor prismatische slip van dislocaties. Dit is een sterke aanwijzing dat deze facetten gevormd werden als gevolg van prismatische slip. Het breukoppervlak van het monster met de grootste korrels bevatte een afwijkend facet. Dit facetvlak was quasi parallel met een basaal kristalvlak, en vertoonde markeringen volgens een waaierpatroon, hetgeen wijst op een kliefbreukmechanisme. Dit toont aan dat facetten mogelijks gevormd kunnen worden door verschillende mechanismes, afhankelijk van onder andere de korrelgrootte.

Een analyse van de lokale textuur toonde aan dat de Taylor factor van elke facetvormende korrel over het algemeen hoger was dan de Taylor factoren van de buurkorrels. De Taylor factor kan gebruikt worden om te differentiëren tussen plastisch harde en zachte korrels, en zou bijgevolg een indicatie kunnen zijn voor de spanningsverdeling tussen korrels. Op doorsnedes van de breukoppervlakken

werden ook secundaire facetten waargenomen, die soms doorheen meer dan één korrel liepen. Deze korte scheurgroei doorheen een korrelgrens bleek mogelijk indien er twee compatibele slipsystemen aanwezig waren. Deze compatibiliteit kon beschreven worden met een uitlijningsfactor.

Bijkomend werden vermoeiingstesten uitgevoerd waarbij de maximale belasting tijdens elke cyclus werd aangehouden gedurende 30 of 120 s. Het aantal cycli tot breuk bij deze testen was twee tot drie ordes van grootte kleiner in vergelijking met gewone vermoeiingstesten, en de breuk was steeds geïnitieerd aan het oppervlak. Dit werd veroorzaakt door de accumulatie van rek als gevolg van kruipverschijnselen tijdens de periodes van aangehouden belasting.

List of abbreviations

hcp – Hexagonal close-packed
bcc – Body-centred cubic
CP – Commercially pure
CRSS – Critical resolved shear stress
CT – Computer tomography
EPFM – Elastic-plastic fracture mechanics
EBSD – Electron backscatter diffraction
FCT – Facet
FGA – Fine granular area
FIB – Focused ion beam
GBF – Granular bright facet
HCF – High cycle fatigue
LCF – Low cycle fatigue
LEFM – Linear elastic fracture mechanics
ODA – Optically dark area
SEM – Scanning electron microscope
UHCF – Ultra-high cycle fatigue
UTS – Ultimate tensile stress
VHCF – Very high cycle fatigue

List of symbols

ε_f – Fracture strain
ϑ – Tilt angle
ϕ_1, Φ, ϕ_2 – Euler angles
σ_a – Stress amplitude
σ_m – Mean stress
σ_{max} – Maximum applied stress
σ_{min} – Minimum applied stress
$\sigma_{y,0.2\%}$ - 0.2% yield stress
τ – Resolved shear stress
ω – Twist angle
A – Alignment factor
b – Burgers vector
ΔK – Stress intensity factor range
ΔK_{eff} – Effective stress intensity factor range
ΔK_{th} – Threshold stress intensity factor range
K_c – Fracture toughness
K_{max} – Maximum stress intensity factor
K_{min} – Minimum stress intensity factor
m – Schmid factor
N – Loading cycles
N_f – Fatigue life
n – Slip plane normal
R – Load ratio
S_a – Average area height (roughness parameter)
S_q – Root mean square area height (roughness parameter)
S_{dr} – Developed interfacial area ratio (roughness parameter)
Y – Geometric factor

Table of Contents

1 Introduction and outline

1.1 Introduction

Structural components are very often subjected to cyclic loads, which can be caused by thermal cycles or by variable mechanical loads. Ever since the Industrial Revolution in the 19th century, it has been known that these cyclic loading conditions can lead to fatigue failure of such components. For metallic materials, the problem of fatigue failure became apparent in this period due to many catastrophic railroad accidents, which were caused by fractured axles. One of the first documented cases is a train crash on the railway between Versailles and Paris on the 5th of October 1842, which was caused by a fractured locomotive axle. This accident, which was the first French railway accident, is reported to have claimed the lives of 60 people.[1] Because these accidents resulted in numerous casualties and also economic losses, it became clear that research needed to be done in order to understand this phenomenon. It is generally claimed that fatigue research was started around 1860 by a German railroad engineer called Wöhler, who performed systematic rotating-bending fatigue tests on railway axles and found that, indeed, repeated loading at stresses below the static strength of the material could ultimately lead to failure.[1] Now, roughly 150 years later, fatigue failure in metals is still a topic of high interest, because of both safety considerations and the economic impact.

One of the main purposes of fatigue research in general is to be able to safely predict when a component will fail. This means that it is necessary to understand the mechanisms that control fatigue life, and to recognize which parameters have an influence. Furthermore, from a materials science point of view, if the mechanisms of fatigue failure in a material can be clarified, it is sometimes possible to improve the fatigue life by changing specific material properties. For a long time, fatigue testing was limited by the loading frequency, which means that the amount of loading cycles that could be applied within a reasonable timeframe was limited. For this reason most tests were stopped after 10^7 cycles. As a result, it was found that many materials exhibited a so-called fatigue limit, which is the stress below which the material was presumed to have an infinite fatigue life. However, because of the development of higher frequency fatigue testing equipment in recent years, the traditional fatigue limit has been found to not exist.[2, 3] In this very high cycle fatigue regime, which involves failure after more than 10^7 cycles, the fatigue behaviour also appears to be governed by different mechanisms. One important difference with low cycle fatigue is that the crack initiation phase takes up most of the fatigue life, even up to 99%.[4] Once a crack has been formed, its growth throughout the material occurs comparatively fast. Therefore, in order to understand the variability of fatigue life in the very high cycle fatigue regime, it is necessary to understand how crack initiation takes place. The problem of very high cycle fatigue failure is particularly important for the aerospace sector, because many aircraft components experience cyclic or vibrational loads at high frequencies. Additionally, in the last 60 years new materials have been developed in this sector, because of weight limitations, which has logically created the need to understand the fatigue properties of these relatively new materials. Titanium alloys are one example of materials that were developed specifically for aerospace applications, because of their good strength-to-weight ratio and corrosion resistance. The so-called workhorse titanium alloy in the aerospace sector is Ti-6Al-4V, which can be used in nearly all sections of an aircraft and accounts for approximately 60% of the total titanium production.[5] For instance, titanium alloys are often the choice for critical components in modern turbine engines, which undergo high-frequency cyclic loading. Fatigue is still the main life-limiting factor for these components.[6]

In most cases, fatigue crack initiation takes place at the surface of a material. However, in the very high cycle fatigue regime, certain materials, including Ti-6Al-4V and also high-strength steels, can develop internal cracks. In high-strength steels, these internal cracks initiate at inclusions.[7] Ti-6Al-4V, on the other hand, does not normally contain inclusions.[5] The reason why internal cracks can nucleate in this material is somewhat more complicated. Observations of internal fatigue crack initiation sites in Ti-6Al-4V have revealed the presence of faceted features. These facets are in fact fractured grains of the α phase, which have broken in a transcrystalline and highly planar manner.[8] The α phase in titanium has a hexagonal crystal structure, and consequently shows very anisotropic mechanical properties.[5] It is generally believed that this anisotropic behaviour at the microscale is the root cause for facet formation and consequently internal crack initiation in Ti-6Al-4V.[8, 9] However, the exact conditions that are necessary for the occurrence of facet formation, and the micromechanisms that control this formation are not yet fully understood. Regarding the suggested facet formation mechanisms, two general concepts can be discerned in literature. The first possibility is that facets are formed by a sudden cleavage mechanism,[10] while the second possibility is that they are preceded by slip band formation.[11] Which of these suggested mechanisms is correct is still under debate. It is necessary to clarify this facet formation behaviour in order to explain the fatigue life variability and to possibly improve the very high cycle fatigue life of Ti-6Al-4V.

Facets at internal fatigue crack initiation sites are found to coincide with certain crystallographic planes.[12, 13] Therefore, it is logical to assume that the crystallographic texture has an influence on this crack initiation behaviour. The crystallographic texture, which describes the distribution of the crystallographic orientations of grains in a metal, is primarily determined during production. With this in mind, it is remarkable that most research on internal fatigue crack initiation in Ti-6Al-4V has been done on samples from forged plates or bars, or rolled plates, and no fatigue testing has been performed on drawn Ti-6Al-4V wires, to the author's knowledge. Because of the textural differences between drawn wires and forged or rolled material forms, fatigue testing of drawn wires could provide new insights into the facet formation mechanisms. Additionally, only a very limited amount of research has been published on the effect of the microstructure, and in particular the effect of the α grain size, on the occurrence of internal crack initiation.[14, 15]

Furthermore, for several applications a special type of fatigue loading occurs, in which the maximum load is maintained for longer periods. This for example happens for fan discs in turbine engines when the rotation speed is constant during the cruise stage.[16] This so-called dwell fatigue can be regarded as an interaction between fatigue and creep loading. Interestingly, dwell fatigue loading of Ti-6Al-4V also leads to facet formation and internal crack initiation.[16, 17] Therefore, it is likely that the mechanisms of crack initiation during dwell fatigue are closely related to the mechanisms of crack initiation during very high cycle fatigue. This relation has not yet been clarified.

1.2 Research objectives and approach

The main goal of this study is to investigate internal crack initiation and facet formation in drawn Ti-6Al-V wires. The objectives of this study are:

- To investigate the influence of the α grain size on the occurrence of internal crack initiation in these wires
- To perform an in-depth analysis of the characteristics of facets that are present at internal crack initiation sites
- To determine what are the facet formation mechanisms in this case
- To understand in which way the crystallographic texture affects both how and why facets are formed
- To clarify the possible link with dwell fatigue phenomena

In this work, an experimental approach is used in order to obtain these objectives. The drawn wires are subjected to different heat treatments in order to change the α grain size. Fatigue and dwell fatigue tests are then performed on these wires. The fatigue test parameters and wire preparation method are carefully tuned in order to achieve internal crack initiation within a sensible timeframe. The fracture surfaces, and in particular the facets at internal crack initiation sites, are characterized in detail by using advanced microscopy techniques. These observations are then used to reflect on the facet formation mechanisms, and compared with the observations on forged or rolled Ti-6Al-4V that are described in literature.

1.3 Outline

Chapter 2 contains a literature review, which first describes the properties of titanium alloys and Ti-6Al-4V. Next, a brief overview of fatigue in metals is provided, in order to explain certain important concepts and definitions. In the third section of this chapter, the literature on internal fatigue crack initiation in Ti-6Al-4V is discussed extensively. Chapter 3 provides details on the materials preparation and experimental methods that are used in this work. In chapter 4, the influence of the α grain size on the fatigue behaviour is studied. This includes a comparison of the fatigue lives and a quantitative fractographic analysis. Chapter 5 contains a detailed investigation of the characteristics of facets at internal crack initiation sites. The observations of surface markings, facet angles and crystallographic grain orientations are then used to discuss the possible facet formation mechanisms. In other words, this chapter provides an answer to the question of how facets are formed. In chapter 6, the influence of the local texture on the susceptibility to facet formation and short crack growth is investigated. By analysing the orientations of neighbouring grains, in terms of Schmid or Taylor factors, an answer is sought to the question of why facets are formed in certain grains. Additionally, it is examined whether facets can also extend into a neighbouring grain by short crack growth, if certain orientation requirements are fulfilled. Chapter 7 contains the results of dwell fatigue tests, which includes a comparison of fatigue lives and fracture surfaces. Finally, the general conclusions are provided in chapter 8, together with suggestions for future work.

1.4 References

[1] W. Schütz (1996). *A history of fatigue.* Engineering Fracture Mechanics, 54(2), p. 263-300.

[2] C. Bathias (1999). *There is no infinite fatigue life in metallic materials.* Fatigue & Fracture of Engineering Materials & Structures, 22(7), p. 559-565.

[3] C. Bathias, L. Drouillac, and P. Le Francois (2001). *How and why the fatigue S-N curve does not approach a horizontal asymptote.* International Journal of Fatigue, 23, p. S143-S151.

[4] V. Kazymyrovych (2009). *Very high cycle fatigue of engineering materials: A literature review.* Karlstad University Studies, 22.

[5] G. Lütjering and J.C. Williams (2007). *Titanium.* 2nd ed, ed. B. Derby. Springer Berlin Heidelberg New York

[6] R.R. Boyer (1996). *An overview on the use of titanium in the aerospace industry.* Materials Science and Engineering A, 213(1-2), p. 103-114.

[7] K. Lambrighs (2010). *Fatigue properties of heavily drawn steel wires.* Ph.D. Thesis. Leuven, Katholieke Universiteit Leuven.

[8] D.F. Neal and P.A. Blenkinsop (1976). *Internal fatigue origins in alpha-beta titanium-alloys.* Acta Metallurgica, 24(1), p. 59-63.

[9] F.P.E. Dunne and D. Rugg (2008). *On the mechanisms of fatigue facet nucleation in titanium alloys.* Fatigue & Fracture of Engineering Materials & Structures, 31(11), p. 949-958.

[10] N.E. Paton, J.C. Williams, J.C. Chesnutt, and A.W. Thompson (1975). *The effects of microstructure on the fatigue and fracture of commercial titanium alloys.* AGARD Conference Proceedings, 185, p. 4-1 - 4-14.

[11] I. Bantounas, D. Dye, and T.C. Lindley (2009). *The effect of grain orientation on fracture morphology during high-cycle fatigue of Ti-6Al-4V.* Acta Materialia, 57(12), p. 3584-3595.

[12] F. Bridier, P. Villechaise, and J. Mendez (2008). *Slip and fatigue crack formation processes in an alpha/beta titanium alloy in relation to crystallographic texture on different scales.* Acta Materialia, 56(15), p. 3951-3962.

[13] S.K. Jha, C.J. Szczepanski, P.J. Golden, W.J. Porter, and R. John (2012). *Characterization of fatigue crack-initiation facets in relation to lifetime variability in Ti-6Al-4V.* International Journal of Fatigue, 42, p. 248-257.

[14] Y. Furuya and E. Takeuchi (2014). *Gigacycle fatigue properties of Ti-6Al-4V alloy under tensile mean stress.* Materials Science and Engineering A, 598, p. 135-140.

[15] H. Oguma and T. Nakamura (2010). *The effect of microstructure on very high cycle fatigue properties in Ti-6Al-4V.* Scripta Materialia, 63(1), p. 32-34.

[16] M.R. Bache (2003). *A review of dwell sensitive fatigue in titanium alloys: the role of microstructure, texture and operating conditions.* International Journal of Fatigue, 25(9-11), p. 1079-1087.

[17] W.J. Evans (2004). *Time dependent effects in fatigue of titanium and nickel alloys.* Fatigue & Fracture of Engineering Materials & Structures, 27(7), p. 543-557.

2 Literature review

2.1 Titanium alloys

Because of their excellent strength-to-weight ratio, corrosion resistance and biocompatibility, titanium alloys have been increasing in popularity ever since they were first developed for aerospace applications in the 1950s.[1] However, since these alloys have a higher cost relative to competitive materials, their use remains limited to applications in which performance is more important than cost.[2] They can be used at maximum operating temperatures up to 600°C, which is higher than aluminium alloys but lower than steels.[1] Interestingly, titanium is actually the ninth most abundant element on the planet, and the fourth most abundant structural metal, with a concentration of approximately 0.6%.[3, 4] The relatively high cost can be explained by the fact that it is not often found in economically extractable concentrations,[3] and the extraction process to obtain pure titanium from its highly stable oxide is costly.[1] Besides aerospace applications such as airframes and gas turbines, titanium is often used for biomedical products such as fracture fixation devices, dental implants and joint replacements,[5] for applications in corrosive environments in the chemical and power industries and in offshore structures[1, 3] and for consumer products such as spectacle frames, high-end sporting goods and high performance cars.[1]

For pure titanium there are two stable crystal structures. At low temperatures the stable structure is hexagonal close-packed (hcp), with a c/a ratio of 1.587, which is called the α phase. At temperatures above 882°C the stable structure is body-centred cubic (bcc), which is called the β phase.[1, 3] Alloying elements are added to alter this general behaviour. The transformation temperature can be increased by adding α-stabilisers such as Al, and it can be decreased by adding β-stabilisers such as Mo, V, Nb and Fe.[2, 5] The concentration of interstitial elements like O, N and C also affects the transformation temperature, and they generally act as α-stabilisers.[1] Depending on which alloying elements are added, titanium alloys can then be categorized in three groups: near-α alloys, α+β alloys and near-β alloys. Near-α alloys, as the name implies, contain predominantly the α phase, while α+β alloys contain some retained β phase at room temperature. Near-β alloys are composed of mostly the β phase, and are generally capable of retaining 100% β at room temperature after quenching.[2] Besides the thermodynamically stable α and β phases, there are some metastable phases that can be formed by rapid cooling from the beta region. These metastable phases are hexagonal martensite (α'), which occurs in low-alloy titanium, orthorhombic martensite (α''), which occurs in titanium alloys with a higher solute content, and the ω phase, which can occur if the martensitic reaction is suppressed by certain alloying elements.[1]

The different alloying elements, combined with different heat treatments, result in a large variety of possible microstructures and consequently properties. The most commonly used titanium alloys are commercially pure (CP) titanium, which took up about 25% of the USA market in 1998,[1] and Ti-6Al-4V, which accounts for approximately 50-60% of the total titanium production.[1-4] CP titanium is used for applications in which corrosion resistance is the most important requirement.[2, 4] Ti-6Al-4V is the most used titanium alloy because of its excellent strength and good fatigue properties.[2, 4] Additionally, its properties can be fine-tuned to specific applications by thermomechanical treatments, which can yield many microstructures because of the presence of both an α-stabiliser, Al, and a β-stabiliser, V. In the next sections, the properties of Ti-6Al-4V are discussed in more detail and the mechanisms that control deformation in this type of α-β alloy are described.

2.1.1 Ti-6Al-4V alloy

As mentioned in the previous paragraph, the most widely used titanium alloy is Ti-6Al-4V, which is also known as "grade 5" titanium. The typical chemical composition of Ti-6Al-4V is shown in Table 2-1. Its popularity is mostly due to its extensive use in the aerospace industry, where this alloy is used for critical components. Some examples are static and rotating parts in the gas turbine engines such as blades, fan discs and housings,[3, 6] airframes, fuselage, floor support structures, landing gear parts, wings and tail assemblies.[2] In the biomedical sector, Ti-6Al-4V is often used for joint replacement parts such as hip, knee and jaw implants as well as for bone screws.[3, 5]

Table 2-1: Chemical composition specification for Ti-6Al-4V (ASTM B863 Grade 5—UNS R56400)[3]

Al	C	Fe	H	N	O	V	Ti
5.5-6.75%	≤0.1%	≤0.4%	≤0.015%	≤0.05%	≤0.2%	3.5-4.5%	bal

The wide variety of applications is based on the fact that Ti-6Al-4V can be processed to improve specific properties by thermomechanical treatments. The link between properties and thermomechanical processing is the microstructure. In Ti-6Al-4V, the presence of Al will stabilize and strengthen the α phase, while V will stabilize the β phase. Figure 2-1 shows three isothermal sections of the ternary Ti-Al-V phase diagram, with the black dot representing Ti-6Al-4V. Above approximately 1000°C, the β phase is stable. At lower temperatures there is a two-phase region in which both the α and β phase are present.

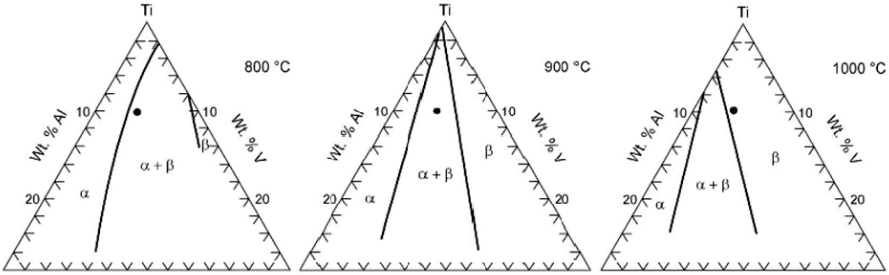

Figure 2-1: Isothermal sections at 800, 900 and 1000°C of the Ti-rich corner of the ternary Ti-Al-V phase diagram, the black dot represents Ti-6Al-4V[1]

It should be noted that even at room temperature, Ti-6Al-4V is still inside this two-phase region. Figure 2-2 shows a pseudo-binary phase diagram that clarifies the effect of V addition to Ti-6Al on the phase transformation and martensite start (Ms) temperatures. By adding 4% V to Ti-6Al, the two-phase region becomes the stable region at room temperature.

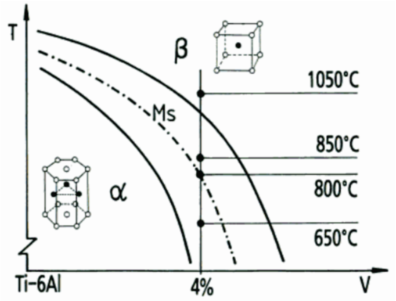

Figure 2-2: Pseudo-binary phase diagram showing the effect of V content on transformation temperatures of Ti-6%Al[3]

Ti-6Al-4V microstructures can generally be classified into three categories. These are lamellar, equiaxed and bimodal,[1, 3] as shown in Figure 2-3. Lamellar microstructures are obtained by annealing above the β transus temperature followed by cooling. During cooling, the α-phase nucleates at the β grain boundaries and forms plates. Higher cooling rates will lead to finer lamellar structures.[1, 3] It is important to note that a cooling rate faster than 1000 °C/min is needed in order to obtain a martensitic structure, which therefore does not often occur in structural Ti-6Al-4V components.[1] Equiaxed microstructures can be produced by a mechanical deformation step in the α+β region and recrystallization annealing just under the β transus temperature, followed by slow cooling.[3] The cooling rate should be low in order to prevent the growth of α platelets (secondary α) in the β phase. In this case, only the primary alpha (α_p) grains can grow.[1] If the recrystallization temperature is relatively low, for example 700 °C, a so-called mill-annealed microstructure is obtained, in which the shape of the α_p grains still shows the influence of the mechanical deformation.[3] Ti-6Al-4V is very commonly used in the mill-annealed condition, although this microstructure is not well-defined.[1, 3] The thermomechanical treatment needed in order to produce bimodal microstructures is very similar to that used to obtain equiaxed microstructures. The main difference is the cooling rate after recrystallization annealing under the β transus, which should be higher so that secondary α platelets can form in the β grains. The higher cooling rate is achieved by water quenching or air cooling.[1, 3] An additional aging treatment, to further allow growth of primary and secondary α grains, leads to the often used “solution treated and aged” condition.[3] During aging, Ti_3Al precipitates will form if the aging temperature is below the Ti_3Al solvus temperature, which is between 550°C and 600°C, depending on the precise Al and O content. These precipitates cause an increase in yield strength, but they are also known to promote the formation of intense, planar slip bands on prismatic $\{10\bar{1}0\}$ planes[1, 3] (see also section 2.1.2). Annealing at a temperature above the Ti_3Al solvus temperature is done for stress relieving.[1]

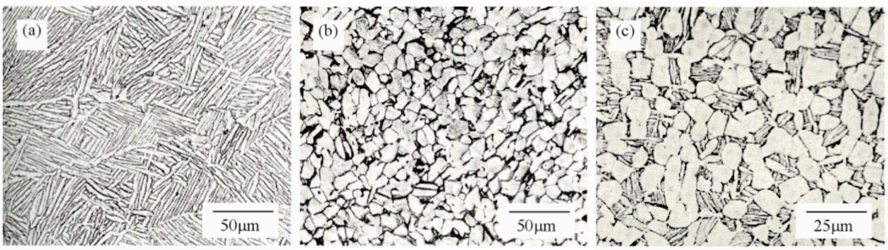

Figure 2-3: (a) Lamellar, (b) equiaxed and (c) bimodal Ti-6Al-4V[7]

The mechanical properties of Ti-6Al-4V are highly dependent on the microstructure and the crystallographic texture. A typical value of the modulus of elasticity is approximately 114 GPa for wrought Ti-6Al-4V.[8] The 0.2% yield strength lies between 830 and 1100 MPa, the ultimate tensile strength between 900 and 1200 MPa and the elongation between 10% and 15%.[8] For cast Ti-6Al-4V, the 0.2% yield strength lies approximately between 870 and 1050 MPa, the ultimate tensile strength between 960 MPa and 1100 MPa and the elongation between 8% and 10%.[9] Amongst the three categories of microstructures, equiaxed microstructures have a high strength and ductility but relatively low fracture toughness, lamellar microstructures have a lower strength and ductility but higher fracture toughness, and bimodal structures have a high strength and the best high cycle fatigue resistance.[5, 10] In general, for all three types of microstructures the strength improves if the grain size is decreased.[10] The fatigue properties of Ti-6Al-4V will be discussed in more detail in section 2.2.4.

2.1.2 Deformation mechanisms in α-β titanium alloys

This section describes some important characteristics of elastic and plastic deformation in α-β titanium alloys such as Ti-6Al-4V. This includes the inherent elastic anisotropy, which is caused by the hexagonal α phase, the different slip systems in the α and β phase and the possibility of twinning.

As is shown in Figure 2-4, the elastic modulus of a single grain of the α phase is highly dependent on the loading direction, because of the intrinsically anisotropic hcp lattice. If the loading axis is parallel to the c-axis, the modulus is the highest, 145 GPa, and if the loading axis is perpendicular to the c-axis (and in this case parallel to a <1000> direction), it is only 100 GPa. The elastic modulus of the β phase at room temperature can only be measured in alloys containing a high amount of β-stabilising elements. From measurements on quenched Ti-V alloys containing between 20% and 40% V, the modulus of elasticity of the β phase at room temperature is found to be approximately between 85 and 110 GPa.[1] At the macroscale, the large variation in elastic modulus of the α phase, depending on the crystallographic orientation, causes large differences in stiffness in textured polycrystals. For example, a rolled Ti-6Al-4V sheet can have a Young's modulus of 100 GPa in the rolling direction and 135 GPa in the transverse direction, simply because of the crystallographic texture.[3] At the microscale, the local misorientation between two neighbouring α grains can also give rise to a local redistribution of stress, or so-called "load shedding", which leads to a higher stress in the stiffer grains.[6] This will be discussed in more detail in section 2.3.8.

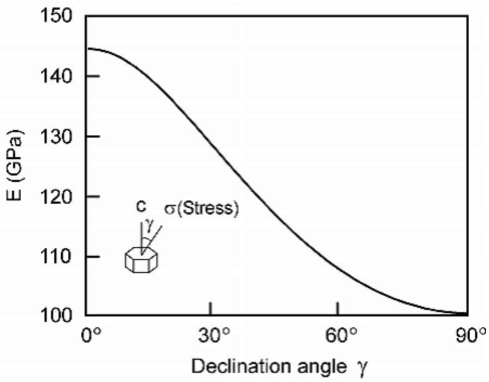

Figure 2-4: Elastic modulus of an α-Ti single crystal as a function of the angle between the c-axis and the loading axis[11]

Plasticity in the α phase can occur by dislocation slip in four groups of slip systems: basal, prismatic, pyramidal 1st order and pyramidal 2nd order. The different slip planes and directions in these slip systems are illustrated in Figure 2-5 and Table 2-2. Prismatic slip has the lowest critical resolved shear stress (CRSS), which means that it requires the smallest shear stress to be activated during deformation, followed by pyramidal 1st order and basal slip. The exact values of the CRSS are dependent on the concentration of alloying elements, such as Al, and interstitials, such as O and N, and on the temperature. For unalloyed titanium with a combined O and N concentration of 0.10%, CRSS values of 90, 97 and 107 MPa are reported for prismatic, pyramidal 1st order and basal slip, respectively.[12] An increase in alloying elements or interstitial levels leads to higher CRSS values and smaller differences between the slip systems. An increase in temperature leads to lower CRSS values.[1] For titanium with 5% Al, the CRSS at room temperature is approximately 160 and 190 MPa for prismatic and basal slip, respectively, while titanium with 6.6% Al shows a CRSS of approximately 200 MPa for both prismatic and basal slip.[13] Pyramidal 2nd order slip has a much higher CRSS, approximately 800 MPa for Ti-6.6%Al at room temperature,[13] and therefore it needs a high shear stress to be activated. The Burgers vector for this slip system is the only one of the $\vec{c} + \vec{a}$ type, which means that the slip direction is not in the basal plane. As a consequence, plastic deformation of the α phase is also highly anisotropic. If for example the loading direction is along the c-axis, only pyramidal 2nd order slip can accommodate plastic deformation, which requires a high stress. This can alternatively be explained using Schmid's law[14], which is:

$$\tau = \cos \phi \cdot \cos \lambda \cdot \sigma \tag{2.1}$$

$$m = \cos \phi \cdot \cos \lambda \tag{2.2}$$

In this equation, τ is the resolved shear stress in the slip system, σ is the applied stress to the material, φ is the angle with the slip plane, λ is the angle with the slip direction and m is called the Schmid factor. If the loading direction is along the c-axis, the Schmid factors for the prismatic, pyramidal 1st order and basal slip systems are zero, which means that the resolved shear stress in these slip systems is zero. Only the pyramidal 2nd order slip system has a non-zero Schmid factor (m≈0.45), but it requires a very high shear stress to be activated. As a result, α grains which are loaded in the c-direction are both elastically and plastically difficult to deform. Plasticity in the β phase can occur by dislocation slip in the usual slip systems for bcc materials, which are on the {110}, {112} and {123} planes, all with a <111> slip direction.[1, 12] Because of its cubic structure, the β phase is much less anisotropic compared to the α phase.

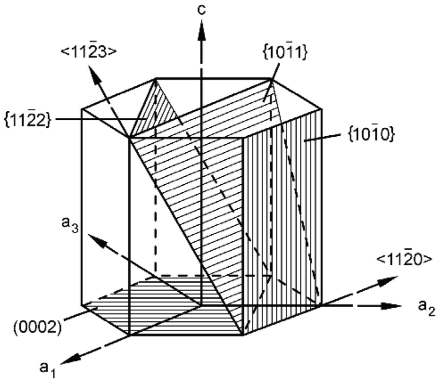

Figure 2-5: Illustration of slip planes and directions in alpha titanium[1]

Table 2-2: Slip directions and planes for four groups of slip systems in alpha titanium, with critical resolved shear stress (CRSS) values for Ti-6.6%Al at room temperature

Slip system	Burgers vector type	Slip direction	Slip plane	CRSS (MPa)[13]
Basal	$\vec{a}$	$\langle 11\bar{2}0\rangle$	(0002)	≈ 200
Prismatic	$\vec{a}$	$\langle 11\bar{2}0\rangle$	$\{10\bar{1}0\}$	≈ 200
Pyramidal 1st order	$\vec{a}$	$\langle 11\bar{2}0\rangle$	$\{10\bar{1}1\}$	≈ 200
Pyramidal 2nd order	$\vec{c}+\vec{a}$	$\langle 11\bar{2}3\rangle$	$\{11\bar{2}2\}$	± 800

In high purity titanium the plastic anisotropy of the α phase is somewhat compensated by the possibility of mechanical twinning, because this can occur if the loading direction is along the c-axis.[1, 12] The main twinning planes in pure titanium are $\{10\bar{1}2\}$, $\{11\bar{2}1\}$ and $\{11\bar{2}2\}$. Because the addition of alloying elements such as Al and the presence of interstitial elements such as O suppress twinning, it generally only plays a major role for high purity titanium or commercially pure titanium with a low O content.[1] Tests on single Ti-Al crystals showed that there is extensive twinning for lower Al concentrations (1.4%), but rarely any twinning for higher Al concentrations (5% and 6.6%).[13] However, recent publications have shown that a low volume fraction of $\{10\bar{1}2\}$ twins can be formed in Ti-6Al-4V during compression at a slow strain rate,[15] compression at a very high strain rate,[16] and during tensile testing at a cryogenic temperature.[17] The twinning mechanism in Ti-6Al-4V becomes more active during dynamic high strain rate tests compared to quasi-static tests, but it occurs in both cases.[16] It has also been suggested that entire α grains in Ti-6Al-4V rotate by twinning during deformation, causing an alignment of the c-axis to the loading direction.[15, 16] Nevertheless, twinning in Ti-6Al-4V is not considered to be a major deformation mechanism at strain rates and temperatures of practical interest.[18]

2.2 Fatigue of metals

Fatigue, coming from the Latin word “fatigare” which means “to tire”, is a progressive and localised accumulation of damage in a material when it is cyclically loaded. The purpose of this section is to explain some more general definitions and phenomena that occur when metals undergo fatigue loading. This will not be an exhaustive review of fatigue of metals, but instead will focus on some concepts that are important for understanding the work described in this thesis. First, the differences between certain fatigue regimes will be discussed. Next, the existence of fatigue limits and crack growth thresholds will be explained, followed by a closer look at the short crack growth problem. Finally, some selected fatigue data of Ti-6Al-4V will be presented, to get an impression of the general fatigue behaviour of this alloy, which depends on the microstructure and on other parameters.

2.2.1 High and low cycle fatigue

Fatigue can be categorized in different regimes, depending on the amount of cycles it takes for the material to fail, which is called the fatigue life N_f. The fatigue life of a material depends first and foremost on the maximum and minimum stress that is applied. At high stresses, when the maximum stress is usually higher than the yield stress, the fatigue life is relatively short and the term low cycle fatigue (LCF, $N_f < 10^5$ cycles) is used. The high cycle fatigue regime (HCF, $10^5 < N_f < 10^7$ cycles) is reached for intermediate stresses. At low stresses, the very high cycle fatigue regime (VHCF, $N_f > 10^7$ cycles) is reached.[19] The term very high cycle fatigue is sometimes replaced by the term ultra-high cycle fatigue (UHCF), and some authors also use the term gigacycle fatigue ($N_f > 10^9$ cycles).[20] During load-controlled fatigue testing in a lab environment generally a sinusoidal waveform is applied between a maximum and a minimum load. The ratio between the minimum and the maximum stress is called the R ratio, which can be positive (tension-tension fatigue), zero (zero minimum stress) or negative (tension-compression fatigue). The obtained data are usually represented in a Wöhler or S-N graph, in which N is the fatigue life (N_f) and S either the maximum or the mean stress.

The reason why cracks initiate in metals during cyclic loading, even when the applied stresses are in the elastic range, is localization of plasticity. Localized plasticity may occur because of the presence of defects which act as stress risers, such as notches or scratches at the surface. Without such stress risers, a sufficiently high stress is needed in order to create cyclic plastic strain, which for example happens in the LCF regime. The local plasticity takes place by dislocation slip, which is usually not perfectly reversible, because it occurs on multiple planes. Slip irreversibility means that dislocations cannot move back in the opposite direction upon reverse loading. As a result, slip steps are created on the surface, leading to surface roughness. The accumulation of slip steps leads to intrusions and extrusions, and persistent slip bands, which are local bands of very extensive plastic deformation. From these features a microcrack can then form.[21] This whole process is considered as the crack initiation stage.

Internal defects such as inclusions or pores are also stress risers, and therefore can lead to nucleation of cracks, again because of localized plasticity.[21] Whether a fatal crack initiates from the surface or from the interior of the material depends on the surface roughness, applied stress, the environment, the presence and size of inclusions or pores and the material properties. In relatively soft metals with high plasticity, such as copper or aluminium alloys, surface roughening by accumulated slip occurs readily, which means that even in the VHCF regime fatigue cracks tend to initiate at the surface.[22] These metals are generally categorized as type I materials.[20, 22] Materials with a high yield stress and lower ductility, such as certain high-strength steels and titanium alloys, are more prone to internal crack initiation and are categorized as type II materials.[20, 22] Similarly, type I and type II materials have been distinguished as showing “plastic” and “pseudo-elastic” fatigue behaviour, respectively. The “plastic” group of materials show extensive and diffuse micro-slip, and as a result crack nucleation will take place at the surface because of surface roughening. The “pseudo-elastic” behaviour occurs in strong materials in which micro-slip is blocked or sharply localized, so that cracks nucleate at locations where there is some microstructural incompatibility.[23] In the case of high-strength steel, the internal cracks nucleate from non-metallic inclusions, resulting in a so-called fish-eye fracture pattern (see section 2.3.1).[19] In the case of titanium alloys there are generally no inclusions or pores and the internal crack initiation is caused by certain microstructural features, which is one of the main topics in this thesis. The internal initiation sites on fatigue fracture surfaces of titanium alloys reveal facetted features, which will be discussed in more detail in section 2.3.3.

2.2.2 Fatigue limits and threshold

For a long time, fatigue testing was limited by the loading frequency that could be applied, which means that testing in the VHCF regime was impractical because it would simply take too much time. For this reason, most tests were stopped after 10^7 cycles. As a result, many materials exhibited a horizontal asymptote or fatigue limit, which is the stress below which the material was presumed to have an infinite fatigue life. This is illustrated by the “S” curve in Figure 2-6 (type A). However, with the development of higher frequency fatigue testing equipment, up to ultrasonic frequencies in the kHz range, the shape of the S-N curve beyond 10^7 cycles can now be determined, and the traditional fatigue limit has been found to not exist.[24, 25] First of all, for type I materials, the fatigue strength steadily decreases between 10^6 and 10^9 cycles, usually by about 50 MPa. For type II materials, which includes titanium alloys, the difference in fatigue strength between 10^6 and 10^9 cycles is higher, usually between 50 and 300 MPa.[22] This larger difference is observed to occur stepwise, which leads to so-called duplex S-N curves (Figure 2-6 type B and C). In this case the fatigue strength decreases again after a plateau, which was the traditional fatigue limit. This behaviour is coupled to the location of crack initiation, which is at the surface for short fatigue lives, but becomes internal at longer fatigue lives.[26] These competing failure modes can be assumed to have a certain probability of occurring, as is illustrated in Figure 2-6. Depending on which failure mode is active for specific test parameters, different types of S-N curves will be measured. The probability distributions will of course also depend on many other factors, such as surface roughness, internal defect size etc.

The traditional fatigue limit has been shown to not exist.[25] However, the concept of infinite fatigue life, which also does not exist according to some authors,[24] cannot yet be disregarded. The traditional fatigue limit is related to surface cracks, and could therefore be called the surface fatigue limit. The mechanism of internal crack initiation might also exhibit some kind of limit, i.e. the internal fatigue limit. This limit, if it exists, would present itself as a second plateau in the S-N curve, after a fatigue life of 10^9 cycles or more.[22] For type I materials there could be a fatigue limit if the stress value is so low that the fraction of irreversible slip becomes negligible.[20] Taking this one step further, if the applied stress levels are low enough to avoid any localized plasticity, at the surface or internal, there does not seem to be a reason why infinite fatigue life should not exist.

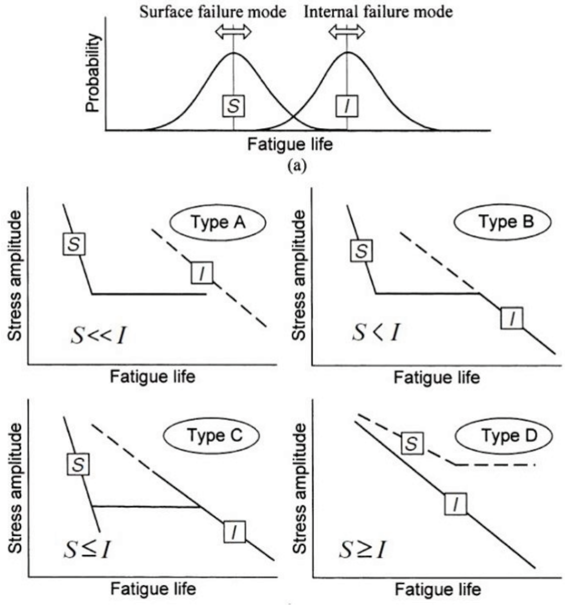

Figure 2-6: Schematic overview of different theoretically possible S-N curves, depending on the probability of surface and internal failure[27]

To describe the stage after crack initiation, which is crack growth, the stress intensity factor range ΔK is generally utilized. The approach of using a stress intensity factor to describe crack growth originates from linear elastic fracture mechanics (LEFM), and implies the assumption that the plastic zone, which is formed at the crack tip, is sufficiently small to be neglected. For a crack with length a and an applied stress range $\Delta\sigma=\sigma_{max}-\sigma_{min}$, ΔK can be calculated as follows:

$$\Delta K = Y\Delta\sigma\sqrt{\pi a} = K_{max} - K_{min} = Y\sigma_{max}\sqrt{\pi a} - Y\sigma_{min}\sqrt{\pi a} \qquad (2.3)$$

Y is a geometric factor that depends on the crack and sample geometry. For a fixed applied stress range, ΔK increases as the crack grows.

The crack growth rate da/dN, in which N represents the amount of loading cycles, can be plotted as a function of ΔK, which typically results in a curve like the one that is shown in Figure 2-7. The crack growth behaviour can be divided in three regions. In region 1, at low ΔK values, the crack growth rate approaches a vertical asymptote. This represents the threshold stress intensity factor range for crack propagation ΔK_{th}, which is the value of ΔK below which cracks do not propagate. For practical reasons, because crack growth rate measurements have certain detection limits, ΔK_{th} is usually the point at which the crack growth rate drops below 10^{-10} m/cycle.[19] However, in the VHCF regime the early crack growth rates can actually be lower, for example as slow as 10^{-13} to 10^{-11} m/cycle for heavily drawn steel wires,[19] which means that the arbitrary threshold value of 10^{-10} m/cycle is not valid in this regime. Additionally, short cracks show a different growth rate behaviour and in some cases can grow even when ΔK is smaller than ΔK_{th}. This will be discussed in section 2.2.3.

In region 2 there is a linear relationship between log(da/dN) and log(ΔK), which is given by the Paris law:

$$\frac{da}{dN} = C(\Delta K)^n \qquad (2.4)$$

In this equation, C and n are constants. In region 3 the crack growth rate continues to increase, until the crack reaches a critical length, at which point K_{max} exceeds the fracture toughness K_c of the material and overload fracture takes place.

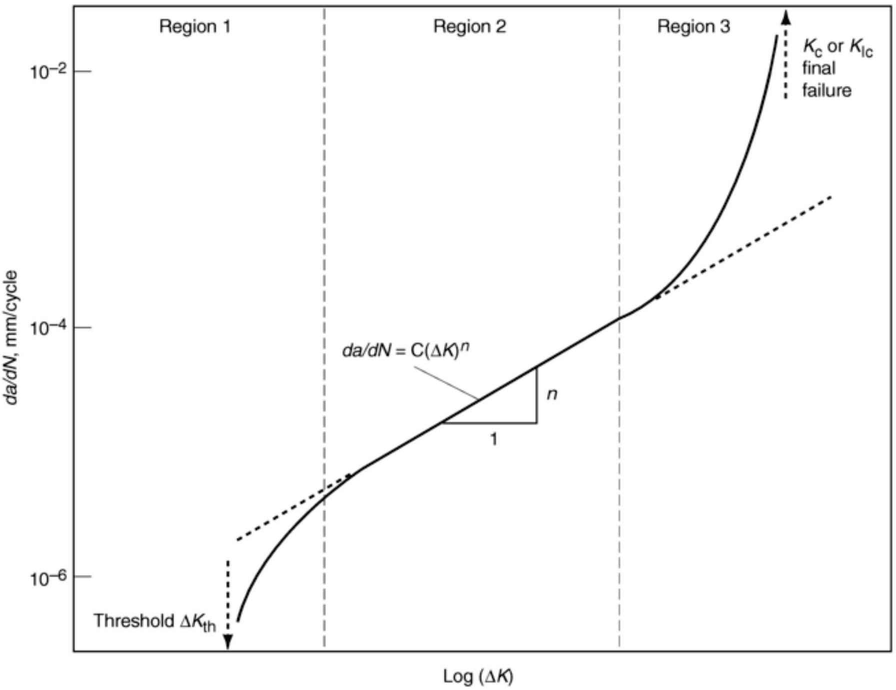

Figure 2-7: Crack growth rate as a function of stress intensity factor range ΔK, indicating the threshold stress intensity factor range ΔK_{th} and the fracture toughness K_c [28]

The crack growth rate and ΔK_{th} also depend on the R ratio because of crack closure. As already mentioned, a plastic zone exists around the crack tip. Because the deformation in this zone is plastic, it remains present after the crack has grown further into the material, and the crack flanks can come into contact with each other during unloading before the minimum stress is reached. In other words, the crack closes during unloading, or opens during loading, at a stress level that is in between σ_{min} and σ_{max}. This is called plasticity-induced crack closure.[29] Other phenomena can also lead to crack closure, for example the formation of an oxide layer on the crack surface, or wear between both crack faces, which leads to roughness-induced crack closure. The stress level at which a crack opens is sometimes referred to as σ_{op}, which can be used to calculate the effective stress intensity factor range ΔK_{eff} as follows[30]:

$$\Delta K_{eff} = K_{max} - K_{op} = Y\sigma_{max}\sqrt{\pi a} - Y\sigma_{op}\sqrt{\pi a} \quad (if\ K_{op} > K_{min}) \quad (2.5)$$

$$\Delta K_{eff} = K_{max} - K_{min} \quad (if\ K_{op} \leq K_{min}) \quad (2.6)$$

By measuring ΔK_{eff} the effect of the R ratio on ΔK_{th} can be explained, because it is clear that crack closure can lower the driving force from ΔK to ΔK_{eff}. At high R ratios there is basically no crack closure and ΔK_{eff}= ΔK. At lower R ratios there is crack closure and $\Delta K_{eff} < \Delta K$, which leads to slower crack growth rates. As a result, the threshold stress intensity factor range ΔK_{th} decreases if the R ratio increases.[30]

2.2.3 Short crack growth

The approach of describing crack growth with LEFM relies on certain assumptions. First of all, the plastic zone size at the crack tip should be sufficiently small, typically fifty times smaller than the crack length.[31] Secondly, the material is assumed to be homogeneous. However, these assumptions are not valid for short fatigue cracks, which as a result can grow below ΔK_{th} and are sometimes observed to grow faster than large cracks.[32] A distinction can be made between microstructurally short cracks and mechanically (or physically) short cracks. A crack is microstructurally short when its size is small compared to the characteristic dimension of the microstructure, which is generally the grain size. In this case, the crack can be growing inside a single grain or through only a few grains. A mechanically short crack is small compared to the characteristic mechanical dimensions, which is usually the plastic zone size. In most cases, microstructurally short cracks are also mechanically small.[32]

The difference in behaviour between short and long fatigue cracks can be visualized in a Kitagawa-Takahashi diagram (see Figure 2-8). In the long crack growth region, LEFM can be used and ΔK_{th} is constant. For short cracks there is a horizontal asymptote of which the value, $\Delta\sigma_e$, is approximately equal to the fatigue limit of an unnotched smooth specimen.[19] For mechanically short cracks, the growth behaviour in this region can be described by elastic-plastic fracture mechanics (EPFM).[31] The transition between short and long crack growth is indicated by crack length a_0, which is called the El Haddad parameter.[33] This parameter can be calculated by the following equation[33]:

$$a_0 = \left(\frac{\Delta K_{th}}{\Delta\sigma_e}\right)^2 \frac{1}{\pi} \tag{2.7}$$

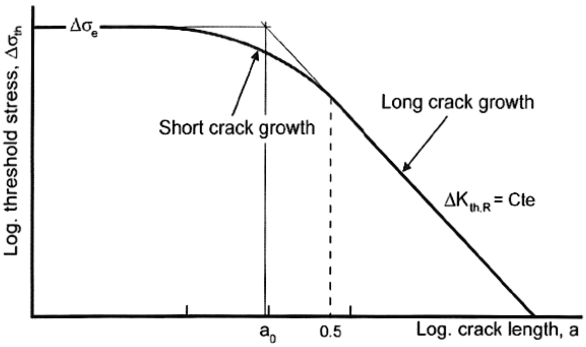

Figure 2-8: Schematic representation of the Kitagawa-Takahashi diagram[19]

The growth rate of short cracks can be different to that of long cracks, as is shown in Figure 2-9. As already mentioned, in some cases cracks can grow below the threshold length and at a much higher growth rate than is predicted by LEFM.[32, 34] However, there can also be non-propagating short cracks, which start growing at a high rate and then become non-propagating,[31] usually when their length is on the order of the grain size.[32] This can happen when the crack encounters a grain boundary.

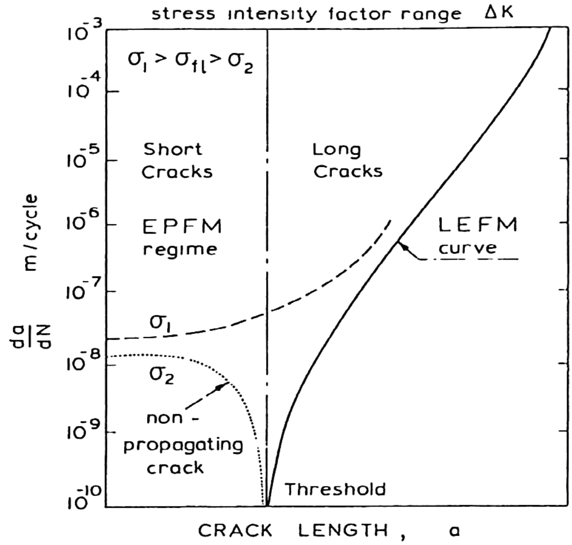

Figure 2-9: Possible crack growth rates of short cracks compared to long cracks[31]

The interaction of a short crack with a grain boundary is highly influenced by the crystallographic orientation of both grains, the activity of secondary slip and cross-slip and the planarity of slip.[32] The α phase in Ti-6Al-4V has a strong tendency for planar slip because of the presence of Al,[1] and short cracks are generally crystallographic in nature, which means that they grow on certain crystallographic planes.[35] This means that the interaction of short cracks with grain boundaries becomes a question of slip plane compatibility between the neighbouring grains, for which a model has been proposed by Zhai et al.[36] In this model, which has been validated for short surface cracks in high strength aluminium alloys[37] and nickel-based superalloys,[38, 39] the compatibility of the active slip systems in both grains, described by the tilt and twist angle, determines if a short surface crack can easily pass through the grain boundary. Figure 2-10 shows a schematic representation of the tilt and twist model to quantify the compatibility of the boundary between two grains. The slip (or crack) planes can be described by unit vectors of the plane normal [N_1] and [N_2], which can be calculated from EBSD measurements. These two planes intersect the sample surface, described by normal unit vector [Z], which results in crack traces that are visible on the surface. The angle between those traces is called the tilt angle ϑ. The grain boundary can be described by a unit vector [E] that is normal to the grain boundary plane. The two crack (slip) planes intersect the grain boundary plane (lines ab and ac in Figure 2-10), and the angle between those intersects is called the twist angle ω. If all the planes are described by known unit vectors normal to the planes, the tilt and twist angles can be calculated as:[37]

$$\omega = \cos^{-1}([E] \times [N_1] \cdot [E] \times [N_2]) \tag{2.8}$$

$$\vartheta = \cos^{-1}([Z] \times [N_1] \cdot [Z] \times [N_2]) \tag{2.9}$$

Cracks that transfer through a grain boundary propagate along the most compatible slip plane, which is the plane with the lowest tilt and twist angles, and not necessarily the plane with the lowest Schmid factor.[40] If there is no suitable low tilt and low twist plane, there is a high resistance to crack growth across the boundary, and cracks can even arrest completely.[36, 37] The twist angle is more important than the tilt angle as a parameter controlling crack transfer, because a high twist angle means that a large part of the grain boundary would have to be fractured if the crack has to pass through the boundary. A high tilt angle would simply lower the driving force at the crack tip.[36] However, in reality a crack can still transfer through a grain boundary if there is a high twist angle, by growing alternately on different slip planes which leads to the formation of steps on the fracture surface. The energy required to do this is lower than the energy required to fracture a large part of the grain boundary. The crack growth resistance in this case is still high, because the crack stepping leads to a longer crack path and crack growth on unfavourable planes.[38] The main difficulty with this model, especially for equiaxed microstructures, is determining the orientation of the grain boundary plane, which generally requires 3D information.[36] Attempts have been made to do in-situ 3D observations of short fatigue crack growth by X-ray computer tomography (CT) techniques, for example in magnesium,[41] but the resolution is not yet adequate to obtain reliable data on short cracks.

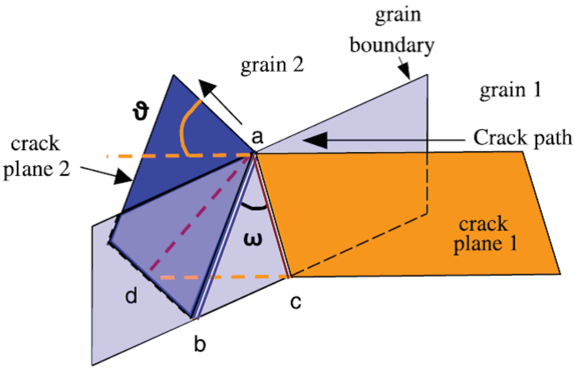

Figure 2-10: Schematic representation of the tilt (ϑ) and twist (ω) model[37]

An adaptation to the tilt and twist model by Zhai et al.[36] has been suggested by King et al.[41], because the original model is only applicable when there are crack or slip traces visible on the sample surface, i.e. for surface cracks. In 3D, for internal cracks, there is no sample surface plane and a more general definition is required, which is illustrated in Figure 2-11. In this case, the twist angle is defined as a rotation about the grain boundary plane normal, which brings the intersects of both slip planes on the grain boundary plane into alignment. The tilt angle is the remaining rotation about a rotation axis that lies in the grain boundary plane.[41]

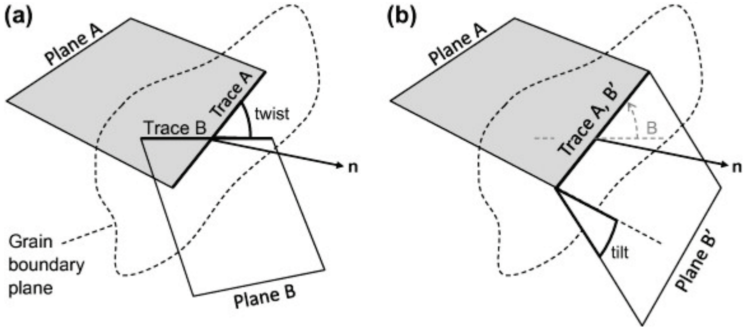

Figure 2-11: More general definition of the tilt and twist model: (a) twist angle and (b) tilt angle calculation[41]

2.2.4 Fatigue of Ti-6Al-4V

In this section, the effect of the microstructure and texture of Ti-6Al-4V on its general fatigue properties is discussed. The influence of the microstructure on internal crack initiation specifically will be discussed in section 2.3.4.

Regarding the different behaviour of equiaxed, bimodal and lamellar Ti-6Al-4V, a useful review study has been performed by Wu et al.[42], who combined the results from 21 references to show that in general, a bimodal microstructure leads to better fatigue properties, followed by lamellar and equiaxed microstructures (see Figure 2-12a). In all three cases, the HCF strength decreases with increasing α grain size or α lamellae width, which is illustrated for the case of an equiaxed microstructure in Figure 2-12b. A different behaviour has been observed from crack growth measurements, in which bimodal microstructures exhibit a higher crack growth rate compared to lamellar microstructures.[43-46] However, for microstructurally short cracks, in the HCF regime, Nalla et al.[44] reported only small differences in fatigue behaviour between bimodal and lamellar Ti-6Al-4V. In order to understand these observations, it is necessary to consider the difference between crack initiation and crack growth. Crack growth rates in lamellar Ti-6Al-4V are generally much lower because the crack path is often deflected and branched. These deflections occur because the crack has to grow through boundaries between colonies, which are regions with different lamellar orientations. On the other hand, this microstructure tends to be sensitive to crack initiation, much more so than equiaxed microstructures. Therefore, bimodal microstructures generally have a good overall fatigue performance in the LCF and HCF regime, because they combine both resistance to crack initiation and resistance to crack growth.[47, 48] Additionally, it has been shown that a lower R ratio can increase the microstructural sensitivity of the fatigue behaviour, most likely due to closure effects.[49]

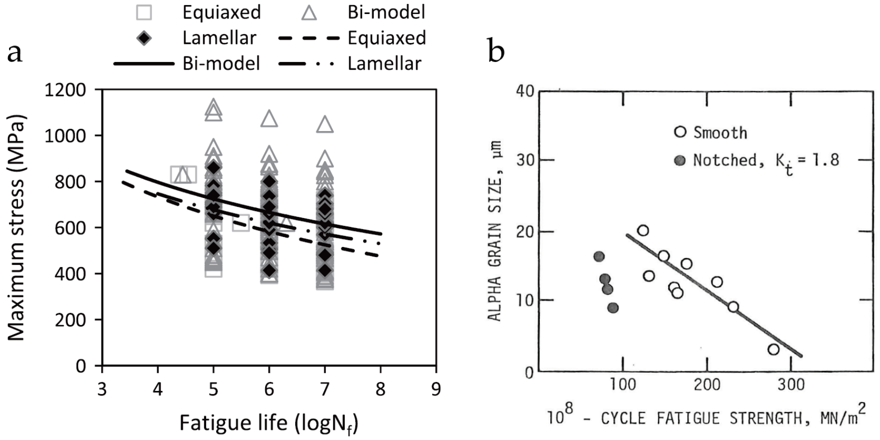

Figure 2-12: a) Comparison of fatigue behaviour of equiaxed, bimodal and lamellar Ti-6Al-4V, with fitted exponential curves[42]; b) Influence of alpha grain size on 10^8-cycle fatigue strength[50]

2.3 Internal fatigue crack initiation in Ti-6Al-4V

In the VHCF regime, the crack initiation phase takes up most of the fatigue life,[43, 51, 52] even up to 99%.[22] Moreover, it has been found that the location of crack initiation tends to shift from the surface towards the subsurface and interior of the material.[53] This shift is coupled with a knee or sudden drop in the S-N curve around 10^7-10^8 cycles, which means that the fatigue strength becomes much lower at these long lifetimes.[45, 54] Similar behaviour is found in certain high-strength steels and nickel alloys.[19, 22] In this section, the phenomenon of internal fatigue crack initiation is discussed. First, the typical case of fish-eye failure in high strength steels is briefly considered, as it has already been investigated more thoroughly compared to titanium, which behaves similarly in certain aspects. However, the origins of internal cracks in titanium are not inclusions, as is the case in high strength steels,[19] but so-called facets, which are α grains that have broken in a planar way.[43, 55, 56] The properties of these facets and the different formations mechanisms that have been suggested in literature, are discussed secondly. Thirdly, the occurrence of internal crack initiation and facets is influenced by several parameters, such as the microstructure, crystallographic texture, residual stress, testing environment, R-ratio (mean stress) and the testing frequency. Finally, this section describes the dwell sensitivity of Ti-6Al-4V, which causes peculiar effects on fatigue life and on the appearance of fracture surfaces when periods of load holding are introduced.

2.3.1 Fish-eye failure in high strength steels

Internal fatigue crack initiation in the VHCF regime in structural steels is always linked to the presence of a non-metallic inclusion.[26] The fracture surfaces in this case reveal a typical "fish-eye" pattern, which is illustrated in Figure 2-13. Around the inclusion, short crack growth leads to the formation of a rough zone, which is called the facet (FCT) area,[19] fine granular area (FGA),[26] granular bright facet (GBF),[27] or optically dark area (ODA).[57] Around this rough short crack growth area, a long crack growth region is formed, which has a lower roughness. When this region reaches a critical size, which depends on the stress level and the fracture toughness of the material, the sample fails by sudden overload fracture. Observations of the microstructure beneath the FCT area have shown that the grain size is much smaller in this region, up to a depth of approximately 400 nm.[26, 58] A plausible theory for the formation of the FCT area is that, even though the inclusion size is smaller than the threshold defect size for fatigue crack growth, it can cause local plasticity in the surrounding material. This leads to the formation of dislocation cells and subgrains. The gradual grain refinement causes a decrease of the crack growth threshold value, which allows the crack to grow.[58] This would explain the fact that the crack growth rate per cycle in the FCT area is smaller than the lattice spacing, since the grain refinement process also takes time.[26, 59] Another theory considers the possibility that the hydrogen concentration around inclusions is higher, which causes local hydrogen embrittlement and consequently a lower crack growth threshold, i.e. hydrogen embrittlement assisted fatigue.[59]

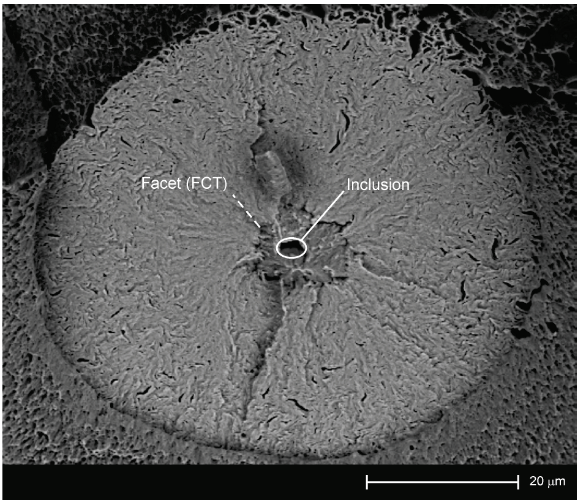

Figure 2-13: Typical fish-eye pattern on the fracture surface of a heavily drawn steel wire[19]

The transition from the rough FCT area to the surrounding smooth region is linked to the transition from short to long crack growth.[19] Therefore, the size of the FCT area can be related to the threshold for long fatigue crack growth. Murakami et al.[57] derived the following equations to estimate ΔK_{th} for surface and internal cracks, with an arbitrary shape, from inclusions in high strength steels:

$$\Delta K_{th} = 0.65 \cdot \Delta\sigma \cdot \sqrt{\pi\sqrt{area}} \qquad (surface) \tag{2.10}$$

$$\Delta K_{th} = 0.5 \cdot \Delta\sigma \cdot \sqrt{\pi\sqrt{area}} \qquad (internal) \tag{2.11}$$

In these formulas, $\Delta\sigma=\sigma_{max}-\sigma_{min}$ is the applied stress range and "area" is the FCT area projected on the plane perpendicular to the sample axis. Experimental data, for example on heavily drawn steel wires and high carbon chromium bearing steel, have confirmed that the value of ΔK_{th} obtained by these formulas is approximately constant and not dependent on the fatigue life.[19, 26]

However, if the size of the inclusion is used as area parameter instead of the FCT area, the obtained values for ΔK_{th} are not constant and there is a tendency of a decreasing fatigue life with increasing inclusion size.[19, 26] Additionally, for a given inclusion size the fatigue life of samples with surface initiated cracks tends to be lower compared to samples with internally initiated cracks.[19]

2.3.2 Crack initiation in Ti-6Al-4V

Internal fatigue crack initiation in Ti-6Al-4V is not caused by inclusions, as titanium alloys normally do not contain inclusions.[1] However, fractographic inspections of internal fatigue crack initiation sites in Ti-6Al-4V instead also reveal a rough area, which contains faceted features, as is illustrated in Figure 2-14. These facets are in fact fractured α grains, which have broken in a transcrystalline and very planar manner.[53] Typically a cluster of many facets is found at the internal crack initiation site, while only one or a few facets are sometimes present in the case of surface initiation.[56, 60] In literature, these features have been called cleavage facets,[47, 53] quasi-cleavage facets,[61-63] shear facets,[48] or low ΔK faceted growth.[64] The difference in nomenclature already suggests the lack of consensus on the formation mechanism of these facets.

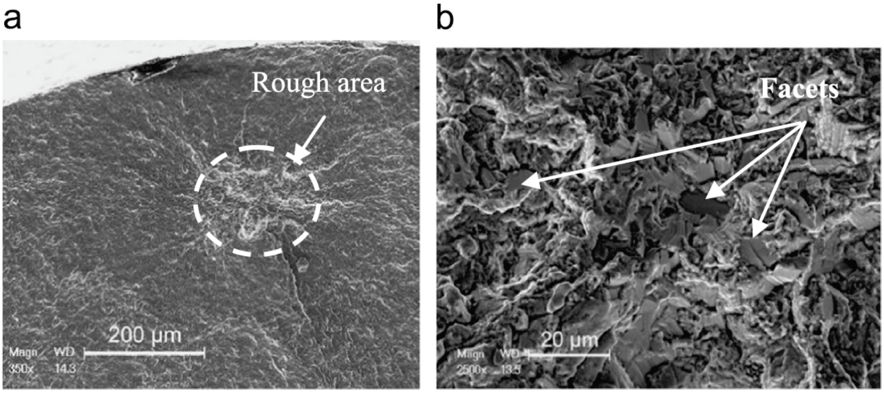

Figure 2-14: Fracture surface of bimodal Ti-6Al-4V sample; a) Rough area at the crack initiation location; b) Magnification of the rough area, revealing the presence of facets[65]

Before discussing the characteristics and formation mechanisms of α facets, it is useful to first consider the overall fractographic appearance of crack initiation sites in Ti-6Al-4V. In the case of crack initiation at the surface, there are generally either no facets, one facet or only a few facets. Samples that fail due to surface crack initiation without facets have the shortest fatigue life, plausibly because the crack develops from a pre-existing surface defect.[56, 65] Furthermore, Jha et al.[56] distinguish samples with surface-initiated cracks with one facet as "life-limiting", and samples with surface-initiated cracks with multiple facets as "long-lifetime", because the latter generally have longer fatigue lives.

In the case of internal crack initiation, there is a distinction between subsurface initiation and fish-eye failure. Subsurface crack initiation is characterized by a cluster of facets that is internal but still very close to the surface of the specimen. This means that when the rough area with facets is formed, the crack grows through to the surface relatively fast, at which point it starts to behave as a regular surface crack. If the initiation location lies further away from the specimen surface, the crack remains internal even after the rough facet area has formed, which leads to the formation of a smooth circular region of long crack growth, thereby forming a fish-eye failure.[66, 67] Additionally, Liu et al.[68] reported the occurrence of multiple subsurface initiation sites in some samples. These different types of internal crack initiation sites in Ti-6Al-4V are illustrated in Figure 2-15.

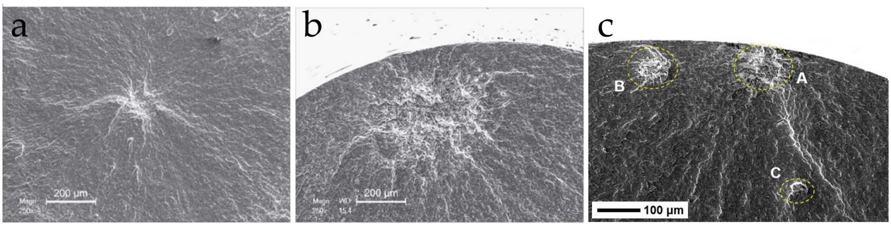

Figure 2-15: Three types of internal crack initiation in Ti-6Al-4V; a) Fish-eye[65]; b) Subsurface[65]; c) Multiple subsurface[68]

Internal crack initiation always leads to longer fatigue lives compared to surface crack initiation.[56] However, in the case of internal initiation, there is some disagreement in literature whether the fatigue life is correlated to the initiation depth, i.e. the distance of the initiation location to the sample surface. Heinz et al.[67] and Zuo et al.[43] reported that the fatigue life was higher if the initiation occurred further away from the sample surface. However, Yokoyama et al.[69] found no correlation between the initiation location and the fatigue life. It is important to consider that the formation of the rough area with facets, which is the crack initiation and short crack growth region, generally occupies over 90% of the total fatigue life.[22] From this point of view, it is logical that the location of this region does not affect the fatigue life drastically.

Besides the location of the rough area, its size can be measured in order to estimate ΔK_{th} using equation 2.11. However, the area parameter in this equation can be interpreted in different ways. For example, Umezawa and Nagai[54] used the length of the projected area of the initiation site on the main crack propagation plane instead of the $\sqrt{}$area parameter, while Liu et al.[65] used the size of the rough area, approximated by an ellipse. The latter reported ΔK_{th} values between 6 and 8 MPa$\sqrt{}$m, regardless of R ratio or fatigue life. Similar values can be calculated from other data in literature.[43, 65, 66] This is higher than the ΔK_{th} values that are obtained from standard fatigue crack growth measurements, which are generally between 2 and 4 MPa$\sqrt{}$m.[70] However, this can be explained by the fact that internal cracks experience a vacuum environment.[65] In fact, crack growth tests on Ti-6Al-4V at different levels of vacuum showed an increase in ΔK_{th} for lower pressures, for example 7.8 MPa$\sqrt{}$m at 3.0×10^{-7} Pa compared to 4 MPa$\sqrt{}$m in air.[71] The effect of different environments on crack initiation and short crack growth behaviour will be discussed in more detail in section 2.3.6.

2.3.3 Alpha facets

As already mentioned, the facets that are seen at fatigue crack initiation locations in Ti-6Al-4V are α grains that have fractured in a planar manner. Some research has been done to characterize certain facet properties such as the crystallographic orientation and spatial distribution of the facet planes. In general, the facets are found to form on specific crystallographic planes (see also Figure 2-5). In most cases, this is reported to be the basal plane[35, 72-76] or a plane only 10-15° off the basal plane, i.e. so-called near-basal.[44, 53, 77] In other cases, the facet planes coincide with prismatic[74, 78] or pyramidal[79] planes. Other publications mention fracture surfaces with facet planes that have formed on either basal or prismatic planes.[56, 60] Interestingly, in the latter case Bridier et al.[60] found that samples with basal facets had a lower fatigue life than samples with prismatic facets, although they only investigated samples with surface crack initiation. The spatial distribution of the facet planes, which can be described as the angle between the facet plane normal and the loading direction, is also variable. Jha et al.[56] reported that the majority of facet angles for a fish-eye sample were between 30° and 60°, with an average of 49°, while Bantounas et al.[77] found that the angles of initiation facets for a subsurface-initiated sample were between 15° and 40°.

This information is useful when considering the loading conditions that were present during facet formation. For this reason, Jha et al.[56] argue that the faceted grains are suitably oriented for shear, which means they have a high Schmid factor, whereas other authors suggest that facets occur when there is a combination of a moderate Schmid factor and a high tensile stress perpendicular to the plane on which the facet forms.[60, 77] Given the fact that facets form on certain crystallographic planes, it is obvious that the texture will also influence the spatial distribution of the facet planes. The influence of texture on faceted crack initiation will be discussed in section 2.3.4. The appearance of alpha facets is usually described as flat and smooth, without any noticeable roughness.[43, 53, 55, 56, 69, 80-83] In a few publications, facets with a radial pattern or featherlike features, as illustrated in Figure 2-16, are observed.[47, 51, 54, 84] Tokaji et al. also mention the presence of slip-like markings on facets on the fracture surface of a Ti-22V-4Al alloy sample.[85]

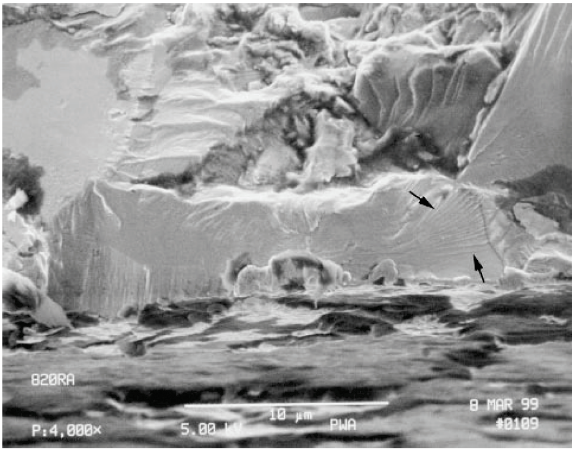

Figure 2-16: Alpha facet with featherlike features (indicated by arrows)[84]

Based on these various observations, several authors have suggested different mechanisms to explain how alpha facets are formed. Only the root cause, which is the highly anisotropic nature of the α phase, is generally agreed upon (see also section 2.1.2). Because the α phase is more difficult to deform along the c-axis both elastically and plastically, grains with their c-axis close to the loading axis behave as hard or strong grains. Grains that are oriented for easy dislocation slip are considered soft or weak grains. During loading, there is a local stress redistribution depending on the local microstructure and texture, i.e. the presence and position of stronger and weaker grains.[53, 63] The result of this stress redistribution is faceted crack initiation, for which several explanations have been given in literature. These can generally be categorized in two groups: those who suspect that facets are formed by cleavage of single α grains[43, 47, 53, 65, 68, 80, 84] and those who suspect that dislocation slip in certain grains leads to facets.[23, 45, 54, 56, 60, 63, 64, 72, 82, 83, 85, 86]

Neal and Blenkinsop[53] were the first to propose the possibility that the facets found at internal fatigue crack initiation sites in Ti-6Al-4V are the result of simple cleavage of α grains. Under normal conditions, the cleavage plane in the α phase is a $\{10\bar{1}7\}$ plane, which lies approximately 15° from the basal plane.[87] It is suggested that during cyclic loading there is dislocation movement on the prismatic planes of certain grains, leading to dislocation pile-ups at grain boundaries.[53] This causes stress fields, with the maximum normal stress on a plane at 70.5° to the prismatic plane that contains the pile-up, according to Stroh.[88] Because the angle between the prismatic and the cleavage plane is approximately 75°, dislocation pile-ups on prismatic planes cause a high normal stress on the cleavage plane of the same grain, as is illustrated in Figure 2-17. If this stress localization becomes high enough, cleavage facets are formed.[43, 53] The featherlike features that are sometimes observed on facets (see Figure 2-16)[47, 84] and the near-basal orientation of facet planes[44, 53, 77] support the possibility of a cleavage formation mechanism. Additionally, local chemical inhomogeneity has been suggested to facilitate the formation of cleavage facets.[47]

It should be questioned whether the local stress can indeed exceed the stress that is necessary for cleavage to occur. The theoretical cleavage stress of titanium (99.97% pure) on the basal plane is approximately 21 GPa.[89] It seems unlikely that such a high stress would be reached as a result of dislocation pile-ups. However, the presence of alloying elements and impurities, such as hydrogen and oxygen, lead to a strong decrease in surface energy,[90] which means that the actual required stress for cleavage is most probably smaller. Furthermore, the theoretical cleavage stress does not take into account any defects. The experimentally determined cleavage stress of CP titanium has been found to be only 1200 MPa.[63] It is reasonable to assume that this stress level could indeed be exceeded locally.

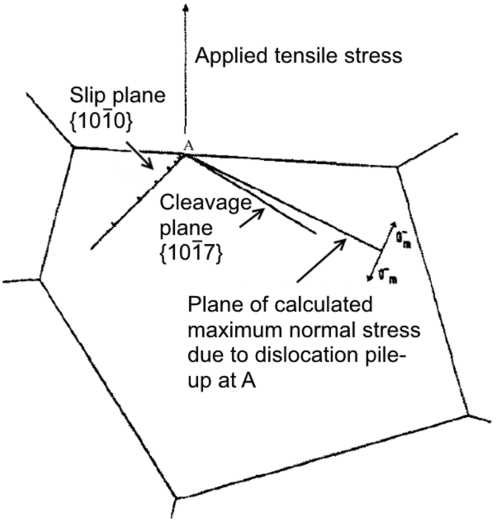

Figure 2-17: Cleavage facet formation due to dislocation pile-up[53]

Several mechanisms have been proposed in which facets are formed by slip band formation in α grains. The term "quasi-cleavage" facets is often used in this case, because the facets have a cleavage-like appearance but are not actually thought to be formed by cleavage fracture.[61-63] Evans and Bache[86, 91] found facets that are perpendicular to the loading axis, which is why they suggest a mechanism in which "source" slip bands in weak grains induce "failure" slip bands in strong grains, which then form facets. This is illustrated in Figure 2-18. A slip band is formed in a weak α grain, which causes shear and tensile stresses on the basal plane of the neighbouring strong grain. This way a slip band can form in the strong grain, even though it is not suitably oriented for dislocation slip, considering the loading axis. The combination of the induced shear stress and the applied normal stress leads to facet formation in the strong grain.[86] Certain worst case grain orientation combinations exist, for which this mechanism would take place very easily.[63]

Other work has shown that facet formation seems to happen in grains that have a combination of a moderate Schmid factor (resolved shear stress) and a high tensile stress on the basal plane. The moderate Schmid factor allows for dislocation slip on the basal plane, while the high tensile stress causes decohesion of the so-formed slip band.[60, 77] This is somewhat in contrast with the mechanism suggested by Evans and Bache, [86, 91] in which the faceted grain actually has a Schmid factor of zero for basal slip and the shear stress is supposedly provided by a slip band in a neighbouring grain. In support of a slip based facet formation mechanism, it was found that introducing spike loads during fatigue testing causes markings to appear on the facets, which means that they form gradually cycle by cycle, and not by sudden cleavage.[45, 64]

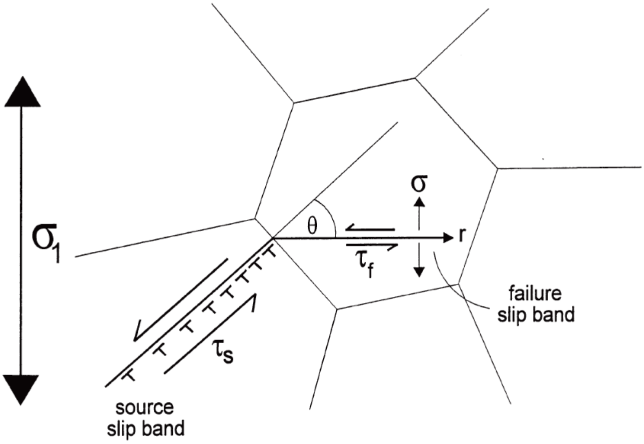

Figure 2-18: Facet nucleation due to slip band formation in a strong grain[86]

The possibility of slip transfer from a β grain to an α grain, which can take place for certain Burger orientation relationships, should also be considered, because slip most likely occurs earlier in the softer β phase.[43, 92] Pilchak et al.[92] also noticed short basal cracks in α colonies which were favourably oriented for slip transfer with the pyramidal slip system in the neighbouring α colony. This indicates possible slip transfer between α grains, even though the pyramidal slip has a high CRSS (see section 2.1.2). Additionally, the distribution of the α and β phase can also play a role in facet formation. A higher local fraction of β was measured by Heinz et al.[67] at the subsurface crack initiation site, and therefore they conclude that a phase inhomogeneity is the reason for internal crack initiation. However, it is not clear why a higher fraction of β should be unfavourable.

Finally, some authors mention that there is a distinction between initiation facets and growth facets. At low ΔK values, cracks in Ti-6Al-4V can grow along basal planes, hence the term "low ΔK faceted growth".[64] There appears to be a transition from structure sensitive crack growth, with the formation of facets, to a structure insensitive crack growth, with striations,[61] and this transition plausibly takes place when the reverse plastic zone size becomes comparable to the α grain size.[49] Jha et al.[56] suspect that not all the facets they observed are crack initiation facets, but that some are formed during small crack growth, which would explain their wide range of measured facet plane angles. Faceted crack growth along the basal plane seems to happen more easily in α grains which are oriented with their c-axis close to the loading axis.[72, 93]

2.3.4 Influence of microstructure and crystallographic texture

Internal fatigue crack initiation in Ti-6Al-4V has been reported to occur in lamellar, bimodal and equiaxed microstructures.[54] In the case of lamellar Ti-6Al-4V, the internal crack origin consists of a colony of faceted α lamellae with a similar orientation,[43, 44] whereas in equiaxed and bimodal microstructures the facets are primary α grains.[84] In the latter case, it is generally agreed that the α grain size should affect the internal crack initiation behaviour, although the amount of experimental data on this topic is limited.[43, 45, 49, 65, 76, 82]

Some authors suggest that large primary α grains are weak sites in the microstructure, because these have a larger boundary area on which dislocations from the surrounding grains can pile up, leading to higher stresses.[43, 47] Additionally, the effective slip length is longer in a coarse microstructure, which means that higher stress fields can form ahead of pile-ups.[43] Another logical reason for the detrimental effect of large grains is the fact that the facets are larger, which means that if one facet is formed, it will cause a higher local stress concentration.[76] Paton et al.[45] mention that the normal stress that is required to cause facets by a cleavage mechanism would depend on the slip length and thus the grain size as well. As already mentioned, the α grain size would also play a role in faceted crack growth, as it is suggested that there is a transition from structure sensitive, i.e. faceted, crack growth to structure insensitive crack growth when the reverse plastic zone size becomes comparable to the size of the grains.[49, 65]

However, the amount of experimental data to confirm the influence of the α grain size on internal crack initiation is limited. Oguma et al.[82] found that the VHCF strength decreases with increasing grain size, which is also the trend in the HCF regime.[50] More interestingly, the α grain size appears to correlate with the probability of internal crack initiation, although only two microstructures were compared.[82] Some evidence of a grain size effect has been reported by Szczepanski et al.,[94] who found that the facets at subsurface crack initiation sites in Ti-6246 were formed in primary α grains that were slightly larger than average. On the other hand, microscale fatigue tests on a Ti-6246 alloy did not reveal any particular microstructural anomalies or larger grains to be linked with facet formation.[95] Furuya et al.[55] did not observe a dependence of the VHCF strength on the grain size. Therefore they suggest that the size of the cluster of facets, or equivalently the rough area, limits the fatigue strength, and not the size of single facets. This would mean that the grain size only affects the fatigue strength when it approaches the size of the rough area, and grain refinement will lead to saturation of the fatigue strength at a certain point.

Besides the α grain size, the primary α volume fraction also affects the crack initiation behaviour in bimodal microstructures. In a Ti-10V-2Fe-3Al alloy, the probability of subsurface crack initiation was correlated to the primary α volume fraction. More specifically, a high α volume fraction caused a sharp transition from surface initiation to subsurface initiation at a specific stress level.[80] The spatial distribution or clustering of primary α grains, on the other hand, does not appear to play a role in determining the crack initiation location in Ti-6246.[94] The α volume fraction also affects the impact that the α texture has on the fatigue behaviour.[76]

The crystallographic texture of the α phase has a major influence on fatigue crack initiation and short crack growth.[40, 76] It is clear from the discussion on facet formation mechanisms in section 2.3.3 that the local texture is specifically important. For this reason there have already been suggestions on what the optimal texture should be in order to delay crack initiation and prolong the fatigue life. Bache et al.[75, 86] state that instead of minimising the texture, as has been done for Ti-6Al-4V in the past, it can be tailored for specific applications. In this respect, cracks are easily initiated on basal planes in α grains when they are subjected to a large shear stress, so this should be avoided.[76, 86] Interestingly, this means that the texture which results in the highest static properties, does not automatically produce the best fatigue properties.[86] Dunne & Rugg[63] constructed a crystal plasticity model to search for combinations of grain orientations which lead to rapid crack nucleation, and they found that facets form easily on basal planes when they are subjected to high normal stresses, caused by the external load and by the local stress field arising from a specific orientation of neighbouring grains. A microstructure-dependent model proposed by Herasymchuk et al.[96] comes to a similar conclusion, and predicts that the orientation of neighbouring grains can cause variations in fatigue life of an order of magnitude. Even though these suggestions and predictions are useful in order to further understand the crack initiation mechanisms, putting them into practice is not straightforward, because texture control in Ti-6Al-4V is generally quite difficult.[45]

One specific case of the influence of texture on crack initiation in Ti-6Al-4V that should be mentioned, is the effect of macrozones. In forged or rolled Ti-6Al-4V products, a so-called ghost structure is sometimes present. This structure consists of macrozones, which contain primary α grains that have approximately the same crystallographic orientation. These macrozones correspond to prior β grains that were present during the production process. The primary α grains that grow from a parent β grain fulfil a certain orientation relationship with this β grain, and therefore have similar orientations.[72, 74, 97] This is illustrated in Figure 2-19, which shows an EBSD orientation map of a microstructure with α grains of roughly 11 μm in size, but macrozones of 500 μm or more.[97] In several cases, it has been found that faceted crack initiation occurs easily in macrozones in which the α grains are oriented with their c-axis close to the loading axis,[72, 74, 77] or at the interface between two macrozones.[97] The orientation of the macrozone in which the main crack initiates is therefore related to the fatigue life.[73] However, it is important to mention that internal crack initiation is not always related to the presence of macrozones.[68]

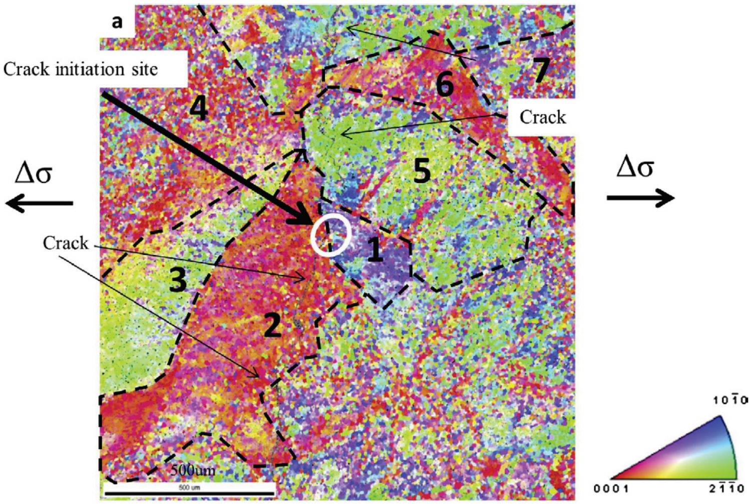

Figure 2-19: Illustration of crack initiation in macrozones in forged Ti-6Al-4V (EBSD orientation map)[97]

It is clear that the microstructure and texture both have a profound effect on internal fatigue crack initiation in Ti-6Al-4V. Both are determined primarily by thermomechanical treatment steps during the production process. More specifically in the case of equiaxed and bimodal microstructures, the texture is strongly influenced by the temperature and deformation that is applied during the working step in the α+β region (see also section 2.1.1).[1] From this point of view, it is important to remark that most research on internal fatigue crack initiation in Ti-6Al-4V has been done on samples from forged plates or bars[51, 56, 60, 65, 68, 74, 77, 82, 97-99] or rolled plates.[75-77, 82]

2.3.5 Influence of residual stress

The fatigue performance of titanium alloys is often enhanced by certain surface treatments, such as shot peening, laser shock peening or deep rolling. These treatments lead to residual compressive stress in the surface region of the material, which delays surface crack initiation.[1, 100, 101] This compressive stress is compensated by the introduction of residual tensile stress in the subsurface zones, which is known to cause subsurface crack initiation.[1, 102-109] More generally, surface preparation has a large effect on fatigue crack initiation in Ti-6Al-4V. Even low stress grinding can introduce a shallow compressive residual stress layer, which leads to an improved fatigue life compared to electrochemically polished samples.[110] On the other hand, addition of surface layers by physical vapor deposition or plasma nitriding, for added wear resistance, generally reduces the fatigue strength because of induced tensile stresses and the brittleness of the formed layers.[111, 112] Because the occurrence of subsurface crack initiation is influenced by surface treatments, the most important ones will be briefly discussed.

Shot peening, which involves shooting the material surface with a stream of hard particles in a controlled way, can result in compressive residual stresses up to 800-1000 MPa, depending on the intensity.[1, 101, 102] Generally, this leads to a shift from surface crack initiation to subsurface crack initiation.[103, 104, 107, 109] The depth of crack initiation can even be linked to the intensity of the shot peening process, because this also determines the depth of the maximum compressive stress.[107] The fatigue life or strength can also be increased, if the process parameters are optimized.[1, 104, 107-109] On the other hand, with the wrong parameters shot peening can also cause a drastic increase in surface roughness, which deteriorates the fatigue properties because it leads to easy surface crack nucleation.[1, 103, 105] Exposure to high temperatures after shot peening can negatively impact the fatigue performance as well, because not only is there stress relaxation, there is also an increased oxygen ingress in the surface layer.[106]

Laser shock peening is a process in which the material surface is exposed to a high energy pulsed laser, which creates a localized high pressure that leads to stresses in the material exceeding the yield stress.[1] As a result, compressive residual stresses can be generated at a larger depth than is possible by shot peening.[100, 113] The surface roughness does not tend to increase as much compared to shot peening, which means that the increase in fatigue life is generally more significant, although laser shock peening is more expensive.[1, 102, 114] Finally, deep rolling is a technique that can be applied to axisymmetric objects, which involves moving a ball or roller tool across the rotating object whilst applying an axial force.[102] This creates compressive residual stresses in the outer layers, like the peening techniques, but additionally lowers the surface roughness and causes grain refinement near the surface.[102, 114] This fine grained layer leads to improved fatigue strength at higher temperatures, when the residual stresses are relaxed.[114] The beneficial effect of different surface treatments on the fatigue strength of Ti-6Al-4V is illustrated in Figure 2-20.

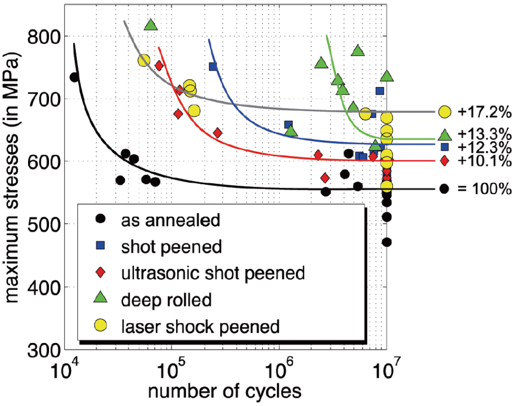

Figure 2-20: Influence of surface treatments on the fatigue strength of Ti-6Al-4V[102]

2.3.6 Influence of testing environment

One of the key differences between internal and surface cracks is the environment that they are exposed to. The environment for an internal crack is presumably some level of vacuum, because it is isolated from the air by the surrounding material.[52] The measurement of ΔK_{th} values for internal cracks, as mentioned in section 2.3.2, provides some evidence for this presumption, seeing as these values are comparable to those obtained from crack growth tests in vacuum.[65, 71] The internal vacuum environment has been indicated by some authors as being the reason why short cracks are able to grow in Ti-6Al-4V. Oguma et al.[82] believe that there is a crack size dependence of ΔK_{th} in vacuum. In other words, for short cracks in Ti-6Al-4V the value of ΔK_{th} in vacuum becomes smaller compared to the value in air, which allows for crack propagation. On the other hand, McEvily et al.[81] propose that due to the lack of oxygen for short internal cracks a local erosion or wear process can take place between the crack faces, because no oxide layer is formed. This leads to a gradual reduction in crack closure and consequently an increase of ΔK_{eff} (see equation 2.5), until the threshold value for crack propagation is reached. In support of this theory, they point to the presence of rounded fractographic features as shown in Figure 2-21. Similar features were found by Oguma & Nakamura[71] on fracture surfaces obtained from crack growth tests at different levels of vacuum, but only on those samples that were tested in high vacuum conditions, which supports the suggestion of an internal wear mechanism.

In order to try simulating internal crack initiation and growth, it is thus logical to do fatigue testing in vacuum conditions. This has provided some interesting insights, because internal cracks are difficult to observe during testing, while surface cracks in a vacuum environment can be more easily monitored. First of all, the crack growth rate at low ΔK values is much lower in vacuum,[35, 71, 115, 116] up to three orders of magnitude compared to tests in air.[70] Secondly, crack initiation is delayed, resulting in higher fatigue lives in vacuum.[93, 116] Thirdly, the fracture surface appearance is affected by testing in vacuum, although the reported changes are not in agreement. Sarrazin-Baudoux[35] found a more crystallographic or faceted crack path in vacuum in the near-threshold regime, because of a stronger localization of deformation in separate grains. Oguma & Nakamura[71] contradictorily noticed a decrease in facets and increase in more ductile features as the vacuum level was increased. In any case, the changes caused by testing in vacuum are generally explained by the absence of oxygen, which prevents the formation of a brittle oxide layer.[71, 115, 116] A different theory by Demulsant & Mendez[93] is that the concentration of hydrogen, which would be one of the products when titanium reacts with water vapour, is lower in vacuum. Tests in air with high humidity indeed seem to lead to accelerated crack growth on basal planes.[1, 35] However, it is very important to remark that tests in vacuum do not entirely simulate internal cracking conditions, because from a thermodynamic point of view titanium already oxidizes at a partial oxygen pressure of only 1.6 x 10^{-155} Pa at room temperature.[117] This is confirmed by Chapman et al.[116], who found that the growth rate of a surface crack in vacuum was still faster than the growth rate of a subsurface crack.

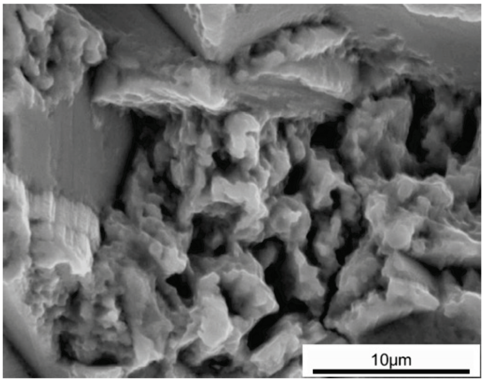

Figure 2-21: Rounded fractographic features as indication of a wear process for internal cracks in Ti-6Al-4V[118]

Another important discussion point regarding environmental effects is hydrogen embrittlement. Apart from hydrogen from external sources, titanium alloys always contain a certain concentration of hydrogen, which is normally kept under 125-150 ppm to avoid embrittlement.[1] However, the vacuum created by an internal crack could locally increase the hydrogen concentration, and the hydrostatic stress field that is caused by dislocation pile ups might also lead to higher hydrogen concentrations at shear bands because of accelerated hydrogen diffusion.[93] Hydrogen alters the slip behaviour and at high concentrations also the preferred cleavage plane.[87, 119] Regarding fatigue crack initiation in Ti-6Al-4V, internal crack initiation was still found to occur even when the hydrogen concentration was reduced to less than 5 ppm,[45] which shows that hydrogen is not the main cause for this phenomenon.[48] Other gases can also affect fatigue crack growth in titanium alloys. For example, Evans et al.[61] found that chlorine gas significantly increased the crack growth rate because of easier formation of quasi-cleavage facets on basal planes. Even inert gas environments such as helium, neon, argon, krypton or xenon seem to affect the crack growth rate and fracture surface appearance in CP titanium.[120]

Besides the composition of the testing environment, the temperature also affects the VHCF behaviour of Ti-6Al-4V. First of all, the fatigue strength increases as the temperature decreases, plausibly because the quasi-static strength also increases.[121, 122] A second interesting observation is the fact that the occurrence or probability of internal crack initiation increases at cryogenic temperatures.[83, 123] Fatigue tests on a

Ti-5Al-2.5Sn ELI alloy at 4 K showed that even with a notch with a stress concentration factor of 1.5, crack initiation occurs subsurface. This effect is linked to the fact that the slip behaviour is different at low temperatures. More specifically, less slip systems are available which leads to a more planar slip behaviour.[123] Additionally, twinning can become active in Ti-6Al-4V at these temperatures.[17]

2.3.7 Frequency and mean stress effects

Internal crack initiation in Ti-6Al-4V generally only occurs in the VHCF regime. Therefore ultrasonic fatigue equipment is often used in order to limit testing time, because cyclic loading can be applied in the kilohertz frequency range.[22] This means that the deformation speed is higher, which results in heating of the material.[124, 125] The test specimens have to be cooled to avoid a temperature increase that would affect the measured fatigue properties. When excessive heating of the material is prevented by proper cooling, it is generally found that there is no clear frequency effect on the fatigue properties of Ti-6Al-4V.[66, 70, 94, 125, 126]

However, a test parameter that does affect crack initiation in Ti-6Al-4V is the mean stress, which can also be described by the R ratio. As already explained in section 2.2.2, crack closure at low R ratios can decrease ΔK_{eff} and consequently retard crack growth. Crack closure in Ti-6Al-4V can start to play a role at R ratios lower than 0.5.[34, 116] Generally, the relation between the fatigue strength at high and low R ratios can be estimated by the Goodman equation[127]:

$$\sigma_a = \sigma_{f\,(R=-1)} \cdot [1 - (\sigma_m/UTS)] \tag{2.12}$$

In this equation, σ_a is the stress amplitude, σ_m is the mean stress, $\sigma_{f(R=-1)}$ is the fatigue limit for fully reversed loading (R=-1) and UTS is the ultimate tensile strength. If the fatigue limit at R=-1 and the ultimate tensile strength are known, the fatigue limit at different R ratios can be estimated. In a constant-life diagram (σ_a versus σ_m), the Goodman equation can be represented by a straight line between $\sigma_{f\,(R=-1)}$ and the UTS. Normally, for most structural materials such as steels and aluminium alloys, this is actually an underestimation and the experimental fatigue limit tends to be somewhat higher.[128] This is illustrated in Figure 2-22a, which shows a typical constant-life diagram for metallic materials. In this graph, the Goodman equation would be a straight line between points A and B, for a constant life of 10^7 cycles, or between points A and D, for a constant life of 10^5 cycles. It can be observed that the typical constant-life curves have a convex shape, which means that the Goodman equation generally underestimates the fatigue limit. However, Ti-6Al-4V and other α+β titanium alloys show an anomalous mean stress sensitivity in the HCF and VHCF regime, which means that for positive mean stress values the fatigue strength is lower than predicted by equation 2.12.[55, 99, 128, 129] This is illustrated in Figure

2-22b, which shows that the data points for small positive R ratios are below the Goodman line, so the fitted constant-life curve has a concave shape. This anomalous behaviour can most probably explained by the fact that a mean tensile stress promotes dislocation pile-ups and localized strain accumulation, which leads to the formation of facets and thus internal crack initiation,[99, 128, 130] although some authors believe twinning could be involved.[55] There is some experimental evidence that Ti-6Al-4V is more prone to internal crack formation under a mean tensile stress.[44, 54, 55, 65, 68, 129] Liu et al. even found that the total facet area increases as the R ratio increases and that subsurface initiation at multiple sites only occurs at a high stress ratio of 0.5.[65, 68] On the other hand, internal crack initiation can still occur at negative R ratios.[129] It has even been observed by Nikitin et al.[98, 131] in fully reversed pure torsion fatigue tests, which is remarkable because in this case the stress is highest at the surface of the sample. Moreover, they did not observe any facets at the crack initiation site, which means that the mechanism of crack initiation might not be the same.

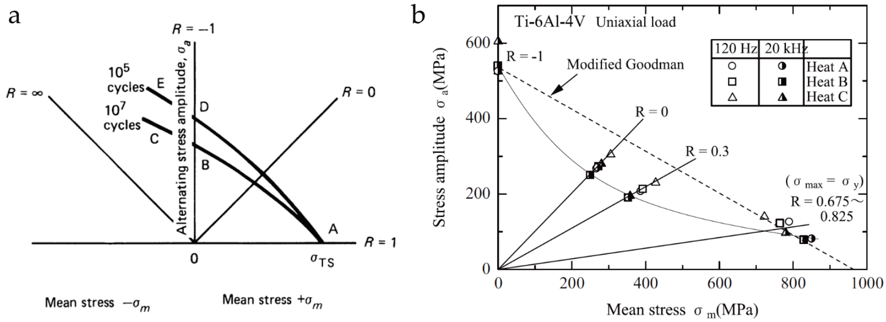

Figure 2-22: a) Typical constant-life diagram (10^5 and 10^7 cycles) for metallic materials;[132] b) Constant-life diagram (10^9 cycles) for Ti-6Al-4V showing the anomalous mean stress effect[55]

2.3.8 Dwell fatigue of Ti-6Al-4V

As discussed in the previous section, a mean tensile stress can have a negative influence on the fatigue life of Ti-6Al-4V. This phenomenon is pronounced even further in the case of dwell fatigue. In contrast with fatigue tests, which are generally performed using sinusoidal loading, dwell fatigue loading consists of a trapezoidal waveform with a certain dwell or hold time at maximum load, as illustrated in Figure 2-23a. This type of loading is highly relevant for aerospace applications, specifically for components such as fan discs in turbine engines.[6] Many titanium alloys, including Ti-6Al-4V, are dwell sensitive, which means that introducing a dwell time at maximum load leads to lower fatigue lives.[6, 91, 133, 134] The reduction in fatigue life because of dwell loading can be several orders of magnitude,[48] and becomes more drastic at longer dwell times[91, 134] and at higher stress levels.[91, 133] This phenomenon is sometimes also called cold dwell[6, 78, 133] or cold creep[91, 134] because it can be regarded as an interaction between fatigue and creep[48] and because it can occur at room temperature.[133] The fracture surfaces of samples after dwell fatigue testing show that cracks initiate internally, which is characteristic of creep,[48] and that the initiation region contains quasi-cleavage facets, as shown in Figure 2-23b.[6, 48, 78, 91, 133-136]

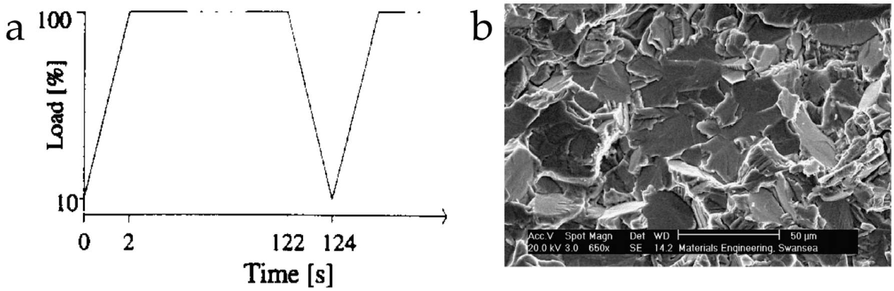

Figure 2-23: a) Dwell fatigue loading cycle;[136] b) Quasi-cleavage facets at subsurface crack initiation site after dwell fatigue[6]

The fact that Ti-6Al-4V displays creep at low temperatures can be attributed to its low strain hardening capability, which is caused by the limited amount of slip systems, the tendency for planar slip and consequently the limited level of dislocation interactions. The result is an accumulation of plastic strain.[91] An increase in grain size corresponds to a longer effective slip length, which explains why coarse grained microstructures are more susceptible to dwell effects.[6, 48, 91] It is important to note that this grain size effect occurs because cold creep in Ti-6Al-4V is governed by dislocation movement.[91] Other creep mechanisms sometimes show an opposite grain size dependence (i.e. a decrease in creep rate if the grain size is increased).[137] Several facet formation mechanisms during dwell fatigue have been suggested in literature. The model proposed by Evans and Bache[136] is the same as the one they propose for facet formation during fatigue without dwell periods, which involves the formation of a failure slip band on the basal plane in a strong grain due to the presence of a source slip band in a neighbouring weak grain (see also section 2.3.3 and Figure 2-18). However, this does not explain the time dependence, nor the fact that dwelling at a constant stress has been found to be more detrimental than dwelling at a constant strain.[63]

To understand these effects, the concept of load shedding has been put forward. Load shedding involves a time dependent redistribution of stress from weak grains, with their c-axis perpendicular to the loading direction, to strong grains, with their c-axis parallel to the loading direction. This occurs because weak grains will deform plastically during loading, which lowers the stress and can lead to a compressive stress after unloading. Strong grains do not deform plastically, but instead are subjected to an increasing stress over time because surrounding weak grains are deforming and are shedding their load onto the strong grain.[63, 138] This process continues until a critical stress for facet formation in the strong grain is reached, as is illustrated in Figure 2-24. Whether this involves slip band formation or cleavage is still unclear.[135, 136, 139]

Dwell sensitivity has also been explained as being the result of environmental effects, and in particular hydrogen diffusion, because an increasing hydrogen content has been found to increase dwell sensitivity[119] and because the crystallographic planes of fracture, i.e. facets, often coincide with known hydride habit planes.[135] Testing in vacuum, on the other hand, lowers the effect of dwell loads.[133] However, alloys with very low hydrogen content still exhibit dwell sensitivity, which shows that hydrogen is not the primary cause.[48] For that reason the time dependency is believed to include both creep and environmental effects.[48, 91] Finally, there has been some effort to model crack initiation during dwell fatigue, with crystal plasticity models[63, 139] and with a cellular automaton simulation method.[138] These models have been successful in showing that fatigue with load dwelling leads to increased accumulated slip[139] and that the orientation of neighbouring grains has an important influence on crack initiation.[63, 138, 139]

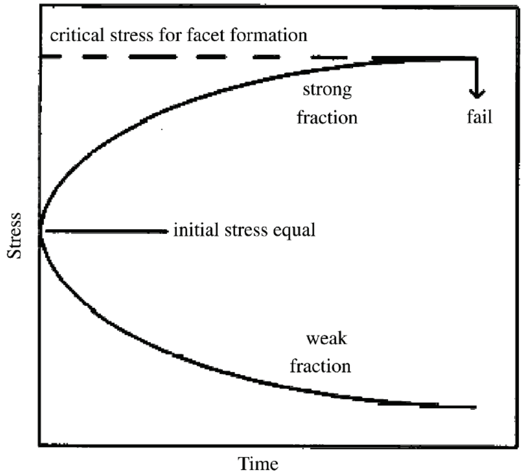

Figure 2-24: Schematic illustration of load shedding from weak to strong grains[48]

2.4 Conclusions

Titanium alloys, and Ti-6Al-4V in particular, are often used for components that undergo cyclic loading. In the high and very high cycle fatigue regime, fatigue cracks in this material can initiate internally, forming so-called fish-eye fracture patterns. The cracks do not nucleate from inclusions, as is the case in high strength steels, but instead the initiation regions contain α facets, which are α grains that have been broken in a planar manner. The highly anisotropic behaviour of the α phase is believed to be the root cause for the formation of facets, because it leads to a stress redistribution that depends on the local orientation of neighbouring grains. However, the mechanism by which these facets are formed is still ambiguous. The mechanisms suggested in literature can generally be categorized in two groups: those in which facets are formed by cleavage, and those in which facets are the result of slip band formation. Increasing the α grain size is believed to lower the fatigue life and increase the probability of internal crack initiation, although the amount of experimental data to confirm this is limited. The crystallographic texture has a significant influence on internal crack initiation and growth, because facets are found to grow on specific crystallographic planes. Therefore, it is remarkable that most research has been done on forged or rolled material with similar textures. At the moment the author is not aware of any publications on fatigue tests on drawn Ti-6Al-4V wires. Residual stress, due to surface preparation or treatments, the testing environment and testing temperature have an influence on the phenomenon of internal crack initiation. A positive mean stress causes lower fatigue lives than expected, and seems to be a necessary condition for the formation of facets. Furthermore, the industrially relevant case of dwell fatigue loading, which is a kind of interaction between creep and fatigue, also leads to facet formation and internal crack initiation. It is likely that these phenomena are closely related, although this is not yet clarified.

2.5 References

[1] G. Lütjering and J.C. Williams (2007). *Titanium*. 2nd ed, ed. B. Derby. Springer Berlin Heidelberg New York

[2] R.R. Boyer (1996). *An overview on the use of titanium in the aerospace industry.* Materials Science and Engineering A, 213(1-2), p. 103-114.

[3] G. Welsch, R. Boyer, and E.W. Collings (1993). *Materials Properties Handbook: Titanium Alloys*. ASM International

[4] M.J. Donachie (2000). *Titanium: A Technical Guide*. 2nd ed. ASM International

[5] A. Braem (2012). *Development of Biofunctional Porous Coatings for Bone Implants (Ontwikkeling van biofunctionele poreuze deklagen voor botimplantaten).* Ph.D. Thesis. Leuven, Katholieke Universiteit Leuven.

[6] M.R. Bache (2003). *A review of dwell sensitive fatigue in titanium alloys: the role of microstructure, texture and operating conditions.* International Journal of Fatigue, 25(9-11), p. 1079-1087.

[7] M.J. Donachie (1982). *Titanium and titanium alloys*. American Society for Metals

[8] S. Lampman (1990). *Wrought Titanium and Titanium Alloys, Properties and Selection: Nonferrous Alloys and Special-Purpose Materials.* ASM Handbook, ASM International, 2, p. 592-633.

[9] D. Eylon, J.R. Newman, and J.K. Thorne (1990). *Titanium and Titanium Alloy Castings, Properties and Selection: Nonferrous Alloys and Special-Purpose Materials.* ASM Handbook, ASM International, 2(634-646).

[10] J.I. Qazi and H.J. Rack (2006). *Titanium alloys for biomedical applications.* Materials Science & Engineering C, Biomimetic and Supramolecular Systems, 26(8), p. 1269-1277.

[11] A. Zarkades and F.R. Larson (1970). *Elasticity of titanium sheet alloys*, in *The Science, Technology and Application of Titanium*, N.E. Promisel, Editor. Pergamon. p. 933-941.

[12] F.H. Froes (2015). *Titanium: Physical Metallurgy, Processing, and Applications*. A S M International

[13] J.C. Williams, R.G. Baggerly, and N.E. Paton (2002). *Deformation behavior of HCP Ti-Al alloy single crystals.* Metallurgical and Materials Transactions A, 33(3), p. 837-850.

[14] E. Schmid and W. Boas (1935). *Kristallplastizität Mit Besonderer Berücksichtigung der Metalle*, in *Struktur und Eigenschaften der Materie*, 17. Springer Berlin Heidelberg.

[15] D.G.L. Prakash et al. (2010). *Deformation twinning in Ti-6Al-4V during low strain rate deformation to moderate strains at room temperature.* Materials Science and Engineering a-Structural Materials Properties Microstructure and Processing, 527(21-22), p. 5734-5744.

[16] F. Coghe, W. Tirry, L. Rabet, D. Schryvers, and P. Van Houtte (2012). *Importance of twinning in static and dynamic compression of a Ti-6Al-4V titanium alloy with an equiaxed microstructure.* Materials Science and Engineering a-Structural Materials Properties Microstructure and Processing, 537, p. 1-10.

[17] S. Di Iorio, L. Briottet, C. Cayron, E.F. Rauch, and D. Guichard (2004). *Damage mechanisms at a microscopic scale of PM Ti-6Al-4V at 20 K.* Journal of Materials Science & Technology, 20, p. 15-18.

[18] R.C. Picu and A. Majorell (2002). *Mechanical behavior of Ti–6Al–4V at high and moderate temperatures—Part II: constitutive modeling.* Materials Science and Engineering: A, 326(2), p. 306-316.

[19] K. Lambrighs (2010). *Fatigue properties of heavily drawn steel wires.* Ph.D. Thesis. Leuven, Katholieke Universiteit Leuven.

[20] M.J. Kirkham and P.K. Liaw (2002). *Advances in ultra-high cycle fatigue.* Mechanisms and Mechanics of Fracture: The John Knott Symposium, ed. W.O. Soboyejo, J.J. Lewandowski, and R.O. Ritchie. Warrendale. Minerals, Metals & Materials Soc

[21] M.E. Fine and Y. Chung (1996). *Fatigue Failure in Metals, Fatigue and Fracture.* ASM Handbook, ASM International, 19, p. 63–72.

[22] V. Kazymyrovych (2009). *Very high cycle fatigue of engineering materials: A literature review.* Karlstad University Studies, 22.

[23] R.K. Steele and A.J. McEvily (1976). *High-cycle fatigue behavior of Ti-6Al-4V alloy.* Engineering Fracture Mechanics, 8(1), p. 31-37.

[24] C. Bathias (1999). *There is no infinite fatigue life in metallic materials.* Fatigue & Fracture of Engineering Materials & Structures, 22(7), p. 559-565.

[25] C. Bathias, L. Drouillac, and P. Le Francois (2001). *How and why the fatigue S-N curve does not approach a horizontal asymptote.* International Journal of Fatigue, 23, p. S143-S151.

[26] T. Sakai (2009). *Review and Prospects for Current Studies on Very High Cycle Fatigue of Metallic Materials for Machine Structural Use.* Journal of Solid Mechanics and Materials Engineering, 3(3), p. 425-439.

[27] K. Shiozawa, L. Lu, and S. Ishihara (2001). *S-N curve characteristics and subsurface crack initiation behaviour in ultra-long life fatigue of a high carbon-chromium bearing steel.* Fatigue & Fracture of Engineering Materials & Structures, 24(12), p. 781-790.

[28] R.O. Ritchie (1977). *Influence of microstructure on near-threshold fatigue-crack propagation in ultra-high strength steel.* Metal Science, 11, p. 368-381.

[29] J. Schijve (1996). *Fatigue crack growth under variable-amplitude loading, Fatigue and Fracture.* ASM Handbook, ASM International, 19, p. 110-133.

[30] T.S. Gross and S. Lampman (1996). *Micromechanisms of Monotonic and Cyclic Crack Growth, Fatigue and Fracture.* ASM Handbook, ASM International, 19, p. 42-60.

[31] K.J. Miller (1982). *The short crack problem.* Fatigue of Engineering Materials and Structures, 5(3), p. 223-232.

[32] R.C. McClung, K.S. Chan, S.J. Hudak, and D.L. Davidson (1996). *Behavior of small fatigue cracks, Fatigue and Fracture.* ASM Handbook, ASM International, 19, p. 153-158.

[33] M.H. El Haddad, T.H. Topper, and K.N. Smith (1979). *Prediction of non propagating cracks.* Engineering Fracture Mechanics, 11(3), p. 573-584.

[34] M.J. Caton, R. John, W.J. Porter, and M.E. Burba (2012). *Stress ratio effects on small fatigue crack growth in Ti-6Al-4V.* International Journal of Fatigue, 38, p. 36-45.

[35] C. Sarrazin-Baudoux (2003). *Environmentally Influenced Fatigue Crack Path in Titanium Alloys*, in *Proceedings of Fatigue Crack Paths (FCP 2003)*: Parma, Italy.

[36] T. Zhai, A.J. Wilkinson, and J.W. Martin (2000). *A crystallographic mechanism for fatigue crack propagation through grain boundaries.* Acta Materialia, 48(20), p. 4917-4927.

[37] T. Zhai, X.P. Jiang, J.X. Li, M.D. Garratt, and G.H. Bray (2005). *The grain boundary geometry for optimum resistance to growth of short fatigue cracks in high strength Al-alloys.* International Journal of Fatigue, 27(10-12), p. 1202-1209.

[38] W. Schaef, M. Marx, H. Vehoff, A. Heckl, and P. Randelzhofer (2011). *A 3-D view on the mechanisms of short fatigue cracks interacting with grain boundaries.* Acta Materialia, 59(5), p. 1849-1861.

[39] M. Marx, W. Schaf, H. Vehoff, and C. Holzapfel (2006). *Interaction of microcracks with selected interfaces: Focused ion beam for a systematic crack initiation.* Materials Science and Engineering a-Structural Materials Properties Microstructure and Processing, 435, p. 595-601.

[40] A. Pineau (2015). *Crossing grain boundaries in metals by slip bands, cleavage and fatigue cracks.* Philosophical Transactions of the Royal

Society of London A: Mathematical, Physical and Engineering Sciences, 373(2038).

[41] A. King et al. (2011). *Three-dimensional in situ observations of short fatigue crack growth in magnesium.* Acta Materialia, 59(17), p. 6761-6771.

[42] G.Q. Wu, C.L. Shi, W. Sha, A.X. Sha, and H.R. Jiang (2013). *Effect of microstructure on the fatigue properties of Ti-6Al-4V titanium alloys.* Materials & Design, 46, p. 668-674.

[43] J.H. Zuo, Z.G. Wang, and E.H. Han (2008). *Effect of microstructure on ultra-high cycle fatigue behavior of Ti-6Al-4V.* Materials Science and Engineering A, 473(1-2), p. 147-152.

[44] R.K. Nalla, B.L. Boyce, J.P. Campbell, J.O. Peters, and R.O. Ritchie (2002). *Influence of microstructure on high-cycle fatigue of Ti-6Al-4V: Bimodal vs. lamellar structures.* Metallurgical and Materials Transactions a-Physical Metallurgy and Materials Science, 33(3), p. 899-918.

[45] N.E. Paton, J.C. Williams, J.C. Chesnutt, and A.W. Thompson (1975). *The effects of microstructure on the fatigue and fracture of commercial titanium alloys.* AGARD Conference Proceedings, 185, p. 4-1 - 4-14.

[46] N. Verdhan, D.D. Bhende, R. Kapoor, and J.K. Chakravartty (2015). *Effect of microstructure on the fatigue crack growth behaviour of a near-alpha Ti alloy.* International Journal of Fatigue, 74, p. 46-54.

[47] M. Janeček et al. (2015). *The very high cycle fatigue behaviour of Ti-6Al-4V.* Acta Physica Polonica A, 128, p. 497-502.

[48] S. Ankem, H. Margolin, C.A. Greene, B.W. Neuberger, and P.G. Oberson (2006). *Mechanical properties of alloys consisting of two ductile phases.* Progress in Materials Science, 51(5), p. 632-709.

[49] P.E. Irving and C.J. Beevers (1974). *Microstructural influences on fatigue crack growth in Ti-6Al-4V.* Materials Science and Engineering, 14(3), p. 229-238.

[50] J.J. Lucas (1973). *Titanium Science and Technology*. Vol. 3. Plenum Press, New York. p. 2081.

[51] M. Hamada and O. Umezawa (2009). *Evaluation of Subsurface Fatigue Crack Life in Forged Ti-6Al-4V Alloys at Cryogenic Temperatures.* Isij International, 49(1), p. 124-131.

[52] I. Marines-Garcia, P.C. Paris, H. Tada, C. Bathias, and D. Lados (2008). *Fatigue crack growth from small to large cracks on very high cycle fatigue with fish-eye failures.* Engineering Fracture Mechanics, 75(6), p. 1657-1665.

[53] D.F. Neal and P.A. Blenkinsop (1976). *Internal fatigue origins in alpha-beta titanium-alloys.* Acta Metallurgica, 24(1), p. 59-63.

[54] O. Umezawa and K. Nagai (1997). *Subsurface crack generation in high-cycle fatigue for high strength alloys.* ISIJ International, 37(12), p. 1170-1179.

[55] Y. Furuya and E. Takeuchi (2014). *Gigacycle fatigue properties of Ti-6Al-4V alloy under tensile mean stress.* Materials Science and Engineering A, 598, p. 135-140.

[56] S.K. Jha, C.J. Szczepanski, P.J. Golden, W.J. Porter, and R. John (2012). *Characterization of fatigue crack-initiation facets in relation to lifetime variability in Ti-6Al-4V.* International Journal of Fatigue, 42, p. 248-257.

[57] Y. Murakami, S. Kodama, and S. Konuma (1989). *Quantitative-evaluation of effects of non-metallic inclusions on fatigue-strength of high-strength steels. I:Basic fatigue mechanism and evaluation of correlation between the fatigue fracture-stress and the size and location of non-metallic inclusions.* International Journal of Fatigue, 11(5), p. 291-298.

[58] P. Grad, B. Reuscher, A. Brodyanski, M. Kopnarski, and E. Kerscher (2012). *Mechanism of fatigue crack initiation and propagation in the very high cycle fatigue regime of high-strength steels.* Scripta Materialia, 67(10), p. 838-841.

[59] Y. Murakami, T. Nomoto, and T. Ueda (1999). *Factors influencing the mechanism of superlong fatigue failure in steels.* Fatigue & Fracture of Engineering Materials & Structures, 22(7), p. 581-590.

[60] F. Bridier, P. Villechaise, and J. Mendez (2008). *Slip and fatigue crack formation processes in an alpha/beta titanium alloy in relation to crystallographic texture on different scales.* Acta Materialia, 56(15), p. 3951-3962.

[61] W.J. Evans, M.R. Bache, M. McElhone, and L. Grabowski (1997). *Environmental interactions with fatigue crack growth in alpha/beta titanium alloys.* International Journal of Fatigue, 19(1), p. S177-S182.

[62] C. Sarrazin-Baudoux (2005). *Abnormal near-threshold fatigue crack propagation of Ti alloys: role of the microstructure.* International Journal of Fatigue, 27(7), p. 773-782.

[63] F.P.E. Dunne and D. Rugg (2008). *On the mechanisms of fatigue facet nucleation in titanium alloys.* Fatigue & Fracture of Engineering Materials & Structures, 31(11), p. 949-958.

[64] A.L. Pilchak, A. Bhattacharjee, A.H. Rosenberger, and J.C. Williams (2009). *Low Delta K faceted crack growth in titanium alloys.* International Journal of Fatigue, 31(5), p. 989-994.

[65] X. Liu, C. Sun, and Y. Hong (2015). *Effects of stress ratio on high-cycle and very-high-cycle fatigue behavior of a Ti-6Al-4V alloy.* Materials Science and Engineering A, 622, p. 228-235.

[66] E. Takeuchi, Y. Furuya, N. Nagashima, and S. Matsuoka (2008). *The effect of frequency on the giga-cycle fatigue properties of a Ti-6Al-4V alloy.* Fatigue & Fracture of Engineering Materials & Structures, 31(7), p. 599-605.

[67] S. Heinz, F. Balle, G. Wagner, and D. Eifler (2013). *Analysis of fatigue properties and failure mechanisms of Ti6Al4V in the very high cycle fatigue regime using ultrasonic technology and 3D laser scanning vibrometry.* Ultrasonics, 53(8), p. 1433-1440.

[68] X. Liu, C. Sun, and Y. Hong (2016). *Faceted crack initiation characteristics for high-cycle and very-high-cycle fatigue of a titanium alloy under different stress ratios.* International Journal of Fatigue.

[69] H. Yokoyama, O. Umezawa, K. Nagai, and T. Suzuki (1997). *Distribution of internal crack initiation sites in high-cycle fatigue for titanium alloys.* Isij International, 37(12), p. 1237-1244.

[70] R.O. Ritchie, D.L. Davidson, B.L. Boyce, J.P. Campbell, and O. Roder (1999). *High-cycle fatigue of Ti-6Al-4V.* Fatigue & Fracture of Engineering Materials & Structures, 22(7), p. 621-631.

[71] H. Oguma and T. Nakamura (2013). *Fatigue crack propagation properties of Ti-6Al-4V in vacuum environments.* International Journal of Fatigue, 50, p. 89-93.

[72] I. Bantounas, D. Dye, and T.C. Lindley (2010). *The role of microtexture on the faceted fracture morphology in Ti-6Al-4V subjected to high-cycle fatigue.* Acta Materialia, 58(11), p. 3908-3918.

[73] M.R. Bache, W.J. Evans, V. Randle, and R.J. Wilson (1998). *Characterization of mechanical anisotropy in titanium alloys.* Materials Science and Engineering a-Structural Materials Properties Microstructure and Processing, 257(1), p. 139-144.

[74] K. Le Biavant, S. Pommier, and C. Prioul (2002). *Local texture and fatigue initiation in a Ti-6Al-4V titanium alloy.* Fatigue & Fracture of Engineering Materials & Structures, 25(6), p. 527-545.

[75] M.R. Bache, W.J. Evans, B. Suddell, and F.R.M. Herrouin (2001). *The effects of texture in titanium alloys for engineering components under fatigue.* International Journal of Fatigue, 23, p. S153-S159.

[76] W.J. Evans, J.P. Jones, and M.T. Whittaker (2005). *Texture effects under tension and torsion loading conditions in titanium alloys.* International Journal of Fatigue, 27(10-12), p. 1244-1250.

[77] I. Bantounas, D. Dye, and T.C. Lindley (2009). *The effect of grain orientation on fracture morphology during high-cycle fatigue of Ti-6Al-4V.* Acta Materialia, 57(12), p. 3584-3595.

[78] E.E. Sackett, L. Germain, and M.R. Bache (2007). *Crystal plasticity, fatigue crack initiation and fatigue performance of advanced titanium alloys.* International Journal of Fatigue, 29(9-11), p. 2015-2021.

[79] H. Knobbe, P. Koster, H.J. Christ, C.P. Fritzen, and M. Riedler (2010). *Initiation and Propagation of Short Fatigue Cracks in Forged Ti6Al4V.* Fatigue 2010, 2(1), p. 931-940.

[80] S.K. Jha and K.S.R. Chandran (2003). *An unusual fatigue phenomenon: duality of the S-N fatigue curve in the beta-titanium alloy Ti-10V-2Fe-3Al.* Scripta Materialia, 48(8), p. 1207-1212.

[81] A.J. McEvily, T. Nakamura, H. Oguma, K. Yamashita, H. Matsunaga, and M. Endo (2008). *On the mechanism of very high cycle fatigue in Ti-6Al-4V.* Scripta Materialia, 59(11), p. 1207-1209.

[82] H. Oguma and T. Nakamura (2010). *The effect of microstructure on very high cycle fatigue properties in Ti-6Al-4V.* Scripta Materialia, 63(1), p. 32-34.

[83] Y. Ono, T. Yuri, H. Sumiyoshi, S. Matsuoka, and T. Ogata (2003). *Subsurface fracture in high-cycle fatigue at cryogenic temperatures in Ti-5 % Al-2.5 % Sn extra low interstitial alloy.* Materials Transactions, 44(9), p. 1702-1705.

[84] S.G. Ivanova, R.R. Biederman, and R.D. Sisson (2002). *Investigation of fatigue crack initiation in Ti-6Al-4V during tensile-tensile fatigue.* Journal of Materials Engineering and Performance, 11(2), p. 226-231.

[85] K. Tokaji, K. Ohya, and H. Kariya (2000). *Subsurface fatigue crack initiation in beta titanium alloys.* Fatigue & Fracture of Engineering Materials & Structures, 23(9), p. 759-766.

[86] M.R. Bache (1999). *Processing titanium alloys for optimum fatigue performance.* International Journal of Fatigue, 21, p. S105-S111.

[87] R.J.H. Wanhill (1973). *Consideration of cleavage in alpha titanium.* Acta Metallurgica, 21(9), p. 1253-1258.

[88] A.N. Stroh (1957). *A theory of the fracture of metals.* Advances in Physics, 6(24), p. 418-465.

[89] K. Miyoshi and D.H. Buckley (1981). *Relationship between the ideal tensile strength and the friction properties of metals in contact with nonmetals and themselves.* NASA Technical Paper 1883.

[90] P.A.T. Olsson, M. Mrovec, and M. Kroon (2016). *First principles characterisation of brittle transgranular fracture of titanium hydrides.* Acta Materialia, 118, p. 362-373.

[91] W.J. Evans (2004). *Time dependent effects in fatigue of titanium and nickel alloys.* Fatigue & Fracture of Engineering Materials & Structures, 27(7), p. 543-557.

[92] A.L. Pilchak, R.E.A. Williams, and J.C. Williams (2010). *Crystallography of Fatigue Crack Initiation and Growth in Fully Lamellar Ti-6Al-4V.* Metallurgical and Materials Transactions a-Physical Metallurgy and Materials Science, 41A(1), p. 106-124.

[93] X. Demulsant and J. Mendez (1996). *Influence of environment on low cycle fatigue damage in Ti-6Al-4V and Ti 6246 titanium alloys.* Materials Science and Engineering a-Structural Materials Properties Microstructure and Processing, 219(1-2), p. 202-211.

[94] C.J. Szczepanski, S.K. Jha, J.M. Larsen, and J.W. Jones (2008). *Microstructural Influences on Very-High-Cycle Fatigue-Crack Initiation in Ti-6246.* Metallurgical and Materials Transactions a-Physical Metallurgy and Materials Science, 39A(12), p. 2841-2851.

[95] C.J. Szczepanski, S.K. Jha, P.A. Shade, R. Wheeler, and J.M. Larsen (2013). *Demonstration of an in situ microscale fatigue testing technique on a titanium alloy.* International Journal of Fatigue, 57, p. 131-139.

[96] O.M. Herasymchuk, O.V. Kononuchenko, P.E. Markovsky, and V.I. Bondarchuk (2016). *Calculating the fatigue life of smooth specimens of two-phase titanium alloys subject to symmetric uniaxial cyclic load of constant amplitude.* International Journal of Fatigue, 83, p. 313-322.

[97] K. Zhang, K.V. Yang, A. Huang, X. Wu, and C.H.J. Davies (2015). *Fatigue crack initiation in as forged Ti-6Al-4V bars with macrozones present.* International Journal of Fatigue, 80, p. 288-297.

[98] A. Nikitin, C. Bathias, and T. Palin-Luc (2015). *A new piezoelectric fatigue testing machine in pure torsion for ultrasonic gigacycle fatigue tests: application to forged and extruded titanium alloys.* Fatigue & Fracture of Engineering Materials & Structures, 38(11), p. 1294-1304.

[99] A. Atrens, W. Hoffelner, T.W. Duerig, and J.E. Allison (1983). *Subsurface crack initiation in high cycle fatigue in Ti6Al4V and in a typical martensitic stainless-steel.* Scripta Metallurgica, 17(5), p. 601-606.

[100] E. Maawad, Y. Sano, L. Wagner, H.G. Brokmeier, and C. Genzel (2012). *Investigation of laser shock peening effects on residual stress state and fatigue performance of titanium alloys.* Materials Science and Engineering a-Structural Materials Properties Microstructure and Processing, 536, p. 82-91.

[101] L.C. Xie, J. Zhang, C.B. Xiong, L.H. Wu, C.H. Jiang, and W.J. Lu (2012). *Investigation on experiments and numerical modelling of the residual stress distribution in deformed surface layer of Ti-6Al-4V after shot peening.* Materials & Design, 41, p. 314-318.

[102] R. Sonntag, J. Reinders, J. Gibmeier, and J.P. Kretzer (2015). *Fatigue Performance of Medical Ti6Al4V Alloy after Mechanical Surface Treatments.* Plos One, 10(3), p. 15.

[103] S. Amin-Yavari, A.A. Ziaei-Moayed, and H.R. Madaah-Hoseini (September 15-18, 2008). *Influence of shot peening treatment on the fatigue life of Ti6Al4V ELI biomedical alloy.* 10th international conference on shot peening (ICSP-10).

[104] T. Ludian, M. Kocan, H.J. Rack, and L. Wagner (2006). *Residual-stress-induced subsurface crack nucleation in titanium alloys.* International Journal of Materials Research, 97(10), p. 1425-1431.

[105] M. Multigner, E. Frutos, C.L. Mera, J. Chao, and J.L. Gonzalez-Carrasco (2009). *Interrogations on the sub-surface strain hardening of grit blasted Ti-6Al-4V alloy.* Surface & Coatings Technology, 203(14), p. 2036-2040.

[106] M. Thomas, T. Lindley, D. Rugg, and M. Jackson (2012). *The effect of shot peening on the microstructure and properties of a near-alpha titanium alloy following high temperature exposure.* Acta Materialia, 60(13-14), p. 5040-5048.

[107] E. Maawad, S. Yi, H.-G. Brokmeier, M. Wollmann, and L. Wagner (2008). *Residual stress-induced subsurface fatigue crack nucleation in shot peened titanium alloys.* 10th international conference on shot peening (ICSP-10).

[108] I. Apachitei, A. Leoni, A.C. Riemslag, L.E. Fratila-Apachitei, and J. Duszczyk (2011). *Enhanced fatigue performance of porous coated Ti6Al4V biomedical alloy.* Applied Surface Science, 257(15), p. 6941-6944.

[109] L. Wagner and G. Lütjering (1984). *Influence of a shot peening treatment on the fatigue limit of Ti-6Al-4V.* Shot Peening, American Shot Peening Society, p. 201-207.

[110] P.J. Golden, R. John, and W.J. Porter (2009). *Variability in room temperature fatigue life of alpha plus beta processed Ti-6Al-4V.* International Journal of Fatigue, 31(11-12), p. 1764-1770.

[111] M.Y.P. Costa, M.L.R. Venditti, M.O.H. Cioffi, H.J.C. Voorwald, V.A. Guimaraes, and R. Ruas (2011). *Fatigue behavior of PVD coated Ti-6Al-4V alloy.* International Journal of Fatigue, 33(6), p. 759-765.

[112] T. Renhui, O. Qiaolin, and W. Qingyuan (2011). *Effect of plasma nitriding on ultra-high cycle fatigue behaviors of Ti-6Al-4V.* Advanced Materials Research, 295-297, p. 2386-2389.

[113] I. Altenberger, Y. Sano, M.A. Cherif, I. Nikitin, and B. Scholtes (2006). *Residual stress state and fatigue behaviour of laser shock peened titanium alloys*, in *Residual Stresses Vii*, 524-525, W. Reimers and S. Quander, Editors. Trans Tech Publications Ltd: Zurich-Uetikon. p. 129-134.

[114] I. Altenberger, R. Nalla, U. Noster, B. Scholtes, and R. Ritchie (2002). *On the Fatigue Behavior and Associated Effect of Residual Stresses in Deep-Rolled and Laser Shock Peened Ti-6Al-4V Alloys at Ambient and Elevated Temperatures.* 7th National Turbine Engine High Cycle Fatigue Conference (HCF 2002).

[115] M.R. Bache, W.J. Evans, and M. McElhone (1997). *The effects of environment and internal oxygen on fatigue crack propagation in Ti-6Al-4V.* Materials Science and Engineering a-Structural Materials Properties Microstructure and Processing, 234, p. 918-922.

[116] T.P. Chapman et al. (2015). *Characterisation of short fatigue cracks in titanium alloy IMI 834 using X-ray microtomography.* Acta Materialia, 99, p. 49-62.

[117] V. Sinha and J.M. Larsen (2012). *Vacuum Levels Needed to Simulate Internal Fatigue Crack Growth in Titanium Alloys and Nickel-Base Superalloys: Thermodynamic Considerations.* Metallurgical and Materials Transactions a-Physical Metallurgy and Materials Science, 43A(10), p. 3433-3441.

[118] H. Oguma (2006). *Very High Cycle Fatigue Properties of Ti-6Al-4V Alloy.* PhD Thesis. Hokkaido University.

[119] W.J. Evans and M.R. Bache (1995). *Hydrogen and fatigue behavior in a near alpha-titanium alloy.* Scripta Metallurgica Et Materialia, 32(7), p. 1019-1024.

[120] M. Shimojo, Y. Higo, and Y. Oya-Seimiya (2000). *Effects of inert gases on fatigue crack growth and their transportation into subsurface regions in titanium.* Metallurgical and Materials Transactions a-Physical Metallurgy and Materials Science, 31(5), p. 1435-1441.

[121] K. Nagai et al. (1991). *Cryogenic mechanical properties of Ti-6Al-4V alloys with 3 levels of oxygen-content.* Isij International, 31(8), p. 882-889.

[122] S.L. Dong, G. Lu, L.Q. Zhang, D.Z. Yang, S.Y. He, and E.H. Han (2009). *Fatigue Properties of Ti-6Al-4V Alloy in Vacuum at Cryogenic Temperature*, in *Protection of Materials and Structures from Space Environment*, 1087, J.I. Kleiman, Editor. Amer Inst Physics: Melville. p. 534-543.

[123] K. Nagai, O. Umezawa, T. Yuri, and K. Ishikawa (1991). *Internal crack initiation in high cycle fatigue at cryogenic temperatures.* Engineering Fracture Mechanics, 40(4-5), p. 957-965.

[124] Z.Y. Huang, H.Q. Liu, C. Wang, and Q.Y. Wang (2015). *Fatigue life dispersion and thermal dissipation investigations for titanium alloy TC17 in very high cycle regime.* Fatigue & Fracture of Engineering Materials & Structures, 38(11), p. 1285-1293.

[125] R.J. Morrissey and T. Nicholas (2005). *Fatigue strength of Ti-6Al-4V at very long lives.* International Journal of Fatigue, 27(10-12), p. 1608-1612.

[126] R. Morrissey and T. Nicholas (2006). *Staircase testing of a titanium alloy in the gigacycle regime.* International Journal of Fatigue, 28(11), p. 1577-1582.

[127] D.W. Cameron and D.W. Hoeppner (1996). *Fatigue properties in engineering, Fatigue and fracture.* ASM Handbook, ASM International, 19, p. 15-26.

[128] J. Lindemann and L. Wagner (1997). *Mean stress sensitivity in fatigue of alpha, (alpha+beta) and beta titanium alloys.* Materials Science and Engineering a-Structural Materials Properties Microstructure and Processing, 234, p. 1118-1121.

[129] H. Oguma and T. Nakamura (2004). *The effect of stress ratios on very high cycle fatigue properties of Ti-6Al-4V*, in *Advances in Fracture and Failure Prevention, Pts 1 and 2*, 261-263, K. Kishimoto, et al., Editors. Trans Tech Publications Ltd: Zurich-Uetikon. p. 1227-1232.

[130] M. Whittaker (2011). *Titanium in the Gas Turbine Engine*. Advances in Gas Turbine Technology, ed. E. Benini. InTech

[131] A. Nikitin, C. Bathias, T. Palin-Luc, and A. Shanyavskiy (2016). *Crack path in aeronautical titanium alloy under ultrasonic torsion loading.* Frattura ed Integrità Strutturale, 35, p. 213-222.

[132] J.A. Charles and F.A.A. Crane (2013). *Selection and Use of Engineering Materials*. 2nd ed. Great Britain. Butterworth-Heinemann

[133] V. Doquet and V. De Greef (2012). *Dwell-fatigue of a titanium alloy at room temperature under uniaxial or biaxial tension.* International Journal of Fatigue, 38, p. 118-129.

[134] M.T. Whittaker, W.J. Evans, and W. Harrison (2009). *Time Dependent Fatigue Fractures of Titanium Alloys.* 12th International Conference on Fracture, Ottawa, 1, p. 2023-2031.

[135] A.L. Pilchak and J.C. Williams (2011). *Observations of Facet Formation in Near-alpha Titanium and Comments on the Role of Hydrogen.* Metallurgical and Materials Transactions a-Physical Metallurgy and Materials Science, 42A(4), p. 1000-1027.

[136] W.J. Evans and M.R. Bache (1994). *Dwell-sensitive fatigue under biaxial loads in the near-alpha titanium alloy IMI685.* International Journal of Fatigue, 16(7), p. 443-452.

[137] J.C. Gibeling (2000). *Creep deformation of metals, polymers, ceramics, and composites, Mechanical Testing and Evaluation.* ASM Handbook, ASM International, 8, p. 363-368.

[138] M.H. Pourian, F. Bridier, P. Pilvin, and P. Bocher (2016). *Prediction of crack initiation sites in alpha Ti-alloys microstructures under dwell-fatigue using Cellular Automaton simulation method.* International Journal of Fatigue, 85, p. 85-97.

[139] F.P.E. Dunne, D. Rugg, and A. Walker (2007). *Lengthscale-dependent, elastically anisotropic, physically-based hcp crystal plasticity: Application to cold-dwell fatigue in Ti alloys.* International Journal of Plasticity, 23(6), p. 1061-1083.

3 Materials and methods

3.1 Materials

This section describes the details of the materials used in this work. Firstly, the preparation of the Ti-6Al-4V wires and the resulting microstructures are described. Secondly, the crystallographic texture of the different microstructures is presented. Finally, the quasi-static tensile properties are discussed.

3.1.1 Materials preparation and microstructures

The Ti-6Al-4V (ASTM B863, grade 5) wire used in this study has a diameter of 1 mm, and was supplied in a coil by Stanford Advanced Materials. Table 3-1 shows the composition as determined by the manufacturer.

Table 3-1: Composition of the Ti-6Al-4V wire, as determined by the manufacturer (wt.%)

Al	V	Fe	C	N	H	O	Others	Ti
6.1	4.1	≤0.10	≤0.01	≤0.01	≤0.01	≤0.009	≤0.2	balance

Four different microstructures are obtained by the following thermomechanical steps:

- Microstructure A: wire straightening, stress relieving (1 h at 600 °C, furnace cooling)
- Microstructure B: 1 h at 920 °C followed by furnace cooling, wire straightening, stress relieving
- Microstructure C: 10 h at 920 °C followed by furnace cooling, wire straightening, stress relieving
- Microstructure D: 50 h at 920 °C followed by furnace cooling, wire straightening, stress relieving

The wires are straightened by applying approximately 1% plastic strain in tension. All of the heat treatments are done in vacuum (< 1 x 10^{-3} Pa). The stress relieving treatment consists of 1 h at 600 °C followed by furnace cooling. Backscattered electron images of polished cross-sections perpendicular to the wire axis of the four obtained microstructures are shown in Figure 3-1. It should be noted that microstructures B, C and D are equiaxed, whereas the grains in microstructure A are elongated along the wire axis, which typifies a mill-annealed microstructure. Therefore, a backscattered electron image of the polished longitudinal section of a wire with microstructure A is shown in Figure 3-2. The average primary α grain diameter, as determined by electron backscatter diffraction (EBSD) measurements on the cross-sections, is approximately 1, 2, 5 and 10 μm for microstructure A, B, C and D, respectively. The fraction of α phase, also determined from EBSD measurements, is approximately 0.93, 0.95, 0.95 and 0.96 for microstructure A, B, C and D, respectively. Prior to mechanical testing, the wires are electrochemically polished for 10 minutes in an electrolyte containing 55 vol.% CH_3COOH, 30 vol.% H_2SO_4 and 15 vol.% HF (48% pure) with a current density of 1.2 $mA \cdot mm^{-2}$. Further details of this electrochemical polishing treatment are reported by Pyka et al.[1] Because of polishing, the wire diameter is reduced to approximately 0.95 mm, although before mechanical testing this value is measured more accurately with a digital calliper for each sample.

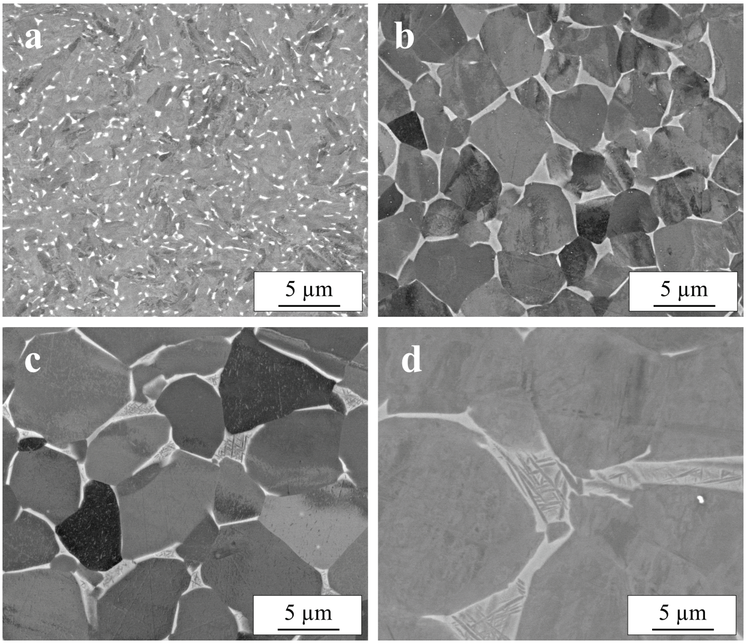

Figure 3-1: Backscattered electron images of polished cross-sections perpendicular to the wire axis of Ti-6Al-4V wires: (a) Microstructure A; (b) Microstructure B; (c) Microstructure C; (d) Microstructure D

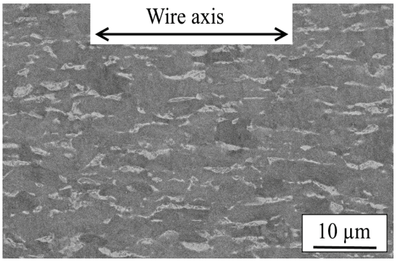

Figure 3-2: Backscattered electron image of a polished longitudinal section of the Ti-6Al-4V wire with microstructure A

3.1.2 Crystallographic texture

The crystallographic texture of the α phase of the four microstructures, measured by EBSD on polished cross-sections including a minimum of 300 primary α grains, is illustrated by $\{10\bar{1}0\}$ and $\{0001\}$ pole figures in Figure 3-3. It can be seen that there is a high tendency for grains to be oriented with the normal direction of the $\{10\bar{1}0\}$ planes parallel to the wire axis, as well as a tendency for grains to be oriented with the normal direction of the $\{10\bar{1}0\}$ planes rotated approximately 60° from the wire axis. The $\{0001\}$ pole figures show that there are nearly no grains oriented with their c-axis parallel to the wire axis. The α texture is very similar for all four microstructures. The texture of the β phase could only be accurately measured for microstructure D, because the size of the β regions in microstructures A, B and C is too small. Figure 3-4 shows that a <110> fibre texture is present in this phase.

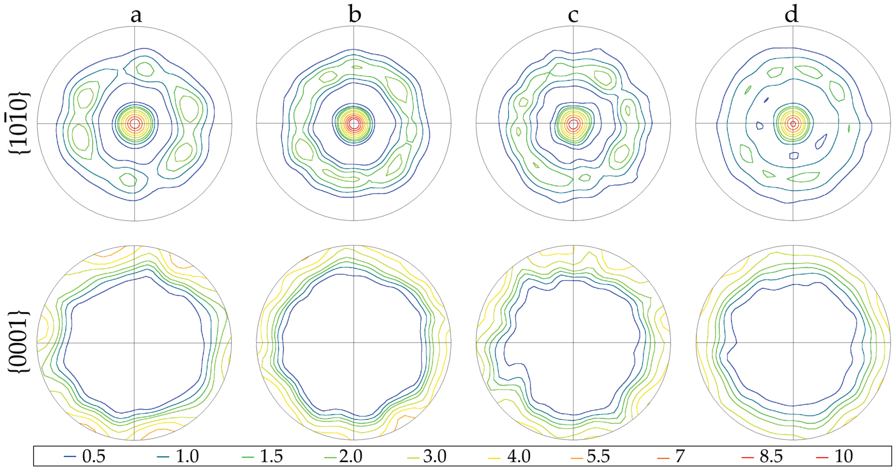

Figure 3-3: $\{10\bar{1}0\}$ and $\{0001\}$ pole figures of the α phase, obtained from EBSD measurements on sample cross-sections, wire axis is perpendicular to the paper; a) Microstructure A; b) Microstructure B; c) Microstructure C; d) Microstructure D

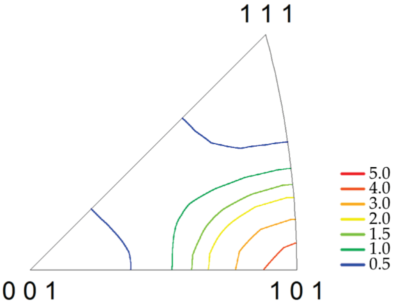

Figure 3-4: Inverse pole figure of the β phase for microstructure D, obtained from an EBSD measurement on a wire cross-section (reference direction is the wire axis)

The β phase contains secondary α, as can be seen in Figure 3-1d. An illustration of the texture of this secondary α is shown in Figure 3-5, which is a colour coded orientation map from an EBSD measurement on the cross-section of a sample with microstructure D. It can be seen that some secondary α rods are oriented with their c-axis parallel to the wire axis, which is perpendicular to the paper.

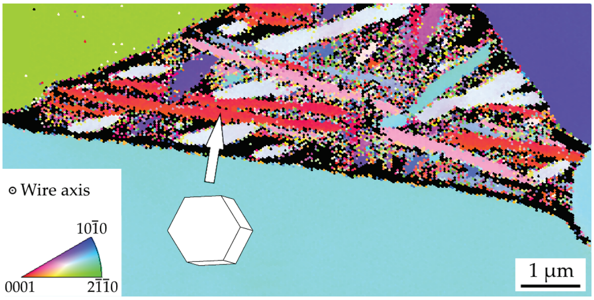

Figure 3-5: Colour coded orientation map (α phase) from EBSD measurement on cross-section of a wire with microstructure D (reference direction is the wire axis, which is perpendicular to the paper), showing a region containing secondary α, with a hexagonal unit cell as illustration

3.1.3 Quasi-static tensile properties

In order to measure the 0.2% yield stress $\sigma_{y,0.2\%}$, the ultimate tensile stress (UTS) and the fracture strain ε_f accurately, three tensile tests have been performed for each microstructure. The average values and standard deviations obtained from these tests are given in Table 3-2. A visual comparison of the engineering stress-strain curves from selected tensile tests on four wires with microstructures A, B, C and D is shown in Figure 3-6. The 0.2% yield stress and UTS of microstructures B, C and D are in a comparable range, but are higher for microstructure A. The fracture strain of microstructure A, on the other hand, seems to be slightly lower in comparison to the other three microstructures. It should be mentioned that these tensile tests are not standardised (see section 3.2.1).

Table 3-2: 0.2% yield stress ($\sigma_{y,0.2\%}$), ultimate tensile stress (UTS) and fracture strain (ε_f) of samples with microstructure A, B, C and D (± standard deviation)

Microstructure	A	B	C	D
$\sigma_{y,0.2\%}$ (MPa)	1056 ± 10	873 ± 16	836 ± 15	850 ± 20
UTS (MPa)	1162 ± 26	980 ± 5	960 ± 11	960 ± 24
ε_f (%)	8 ± 2.1	9 ± 2.8	10 ± 1.8	9 ± 1.6

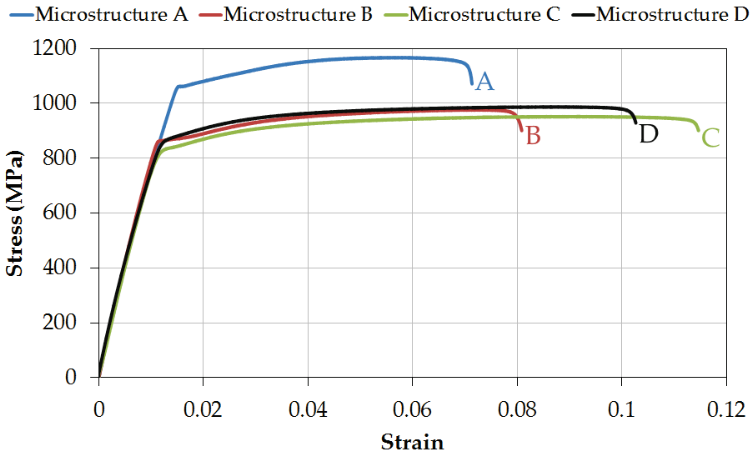

Figure 3-6: Engineering stress-strain curves of samples with microstructures A, B, C and D

3.2 Methods

This section provides details on the methods that were used in this work. This includes mechanical testing and several electron microscopy techniques.

3.2.1 Mechanical testing

For mechanical testing, the wires are cut to approximately 9 cm in length and glued in between two grooved Ti-6Al-4V clamping plates on each side, using Araldite Rapid epoxy adhesive. The grooved plates, schematically shown in Figure 3-7, have a length of 20 mm, width of 15 mm and a thickness of 1 mm. The groove has a width of 1 mm and a depth of 0.5 mm. Consequently, the samples have a free gauge length of approximately 50 mm, but prior to testing this is measured more accurately for each individual sample with a digital calliper. The wire is coated along the gauge length with Sicomet 85 cyanoacrylate glue, in order to protect the wire surface from the environment.

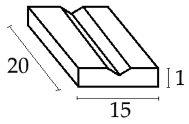

Figure 3-7: Clamping plate dimensions (mm)

Tensile tests, fatigue tests and dwell fatigue tests are all performed on an Instron ElectroPuls E3000. For tensile testing a strain rate of $2x10^{-4}$ s^{-1} is used. All fatigue tests are load controlled. Prior to each fatigue test, the machine is tuned in order to take into account the stiffness of the test sample. During this automatic tuning step, the load is increased from the minimum to the maximum load and back, and the corresponding displacement is registered. This tuning step is necessary to ensure a smooth start-up of the fatigue test. Next, the load is increased to the mean load value over a period of 5 s. This mean load is maintained for 5 s, after which the cyclic loading is started, using a sinusoidal waveform with frequency 60 Hz and load ratio $R=\sigma_{min}/\sigma_{max}=0.1$. The maximum applied stress for the different tests ranges between approximately 85 and 90% of the 0.2% yield stress of the material (see also Table 3-2). Samples that break inside the clamps are discarded. The dwell fatigue tests use a trapezoidal waveform with load ratio R=0.1, which consists of a linear increase to the maximum load during 2 s, a maximum load hold for either 30 or 120 s, a linear decrease to the minimum load during 2 s and a minimum load hold for 5 s, as is shown in Figure 3-8.

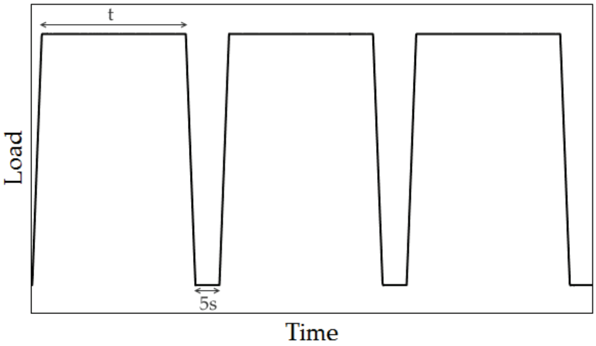

Figure 3-8: Applied load during dwell fatigue testing (t=30 s or 120 s)

3.2.2 Microscopy

Prior to electron microscopy, the fracture surfaces are first ultrasonically cleaned in acetone for one hour and then rinsed with ethanol. For microstructural and EBSD analysis, the samples are embedded, ground with SiC abrasive paper up to a grit of 1200 and polished with a mixture of colloidal silica (OP-S) and hydrogen peroxide (30%).

All scanning electron microscopy (SEM) images of fracture surfaces are made using a FEI Nova NanoSEM 450 with a secondary electron (SE) detector. SEM images of microstructures are taken with a backscattered electron (BSE) detector. Focused ion beam (FIB) milling is done with a FEI Nova 600 Nanolab, using a 30 kV voltage and a current of 20 nA for rough milling and 9 or 6.5 nA for fine milling. For combined FIB milling and EBSD measurements, the wire samples are placed on a tilted holder at 36° and further tilted by 16° in the microscope. This way, FIB milling is done at 52°, and a 180° rotation of the sample leads to the desired 70° angle of the milled surface for EBSD measurements. TSL OIM Analysis 7 software is used to clean

EBSD data, by applying a neighbour confidence index correlation of 0.1, and to calculate Schmid and Taylor factors of individual grains.

Roughness values and spatial facet angles are measured from a 3D topographical reconstruction. This reconstruction is produced by Alicona MeX software, with SEM images at -10°, 0° and 10° tilt as input. The accuracy of this technique for measuring facet angles is reported to be within ±3°.[2]

3.3 References

[1] G. Pyka et al. (2012). *Surface Modification of Ti6Al4V Open Porous Structures Produced by Additive Manufacturing.* Advanced Engineering Materials, 14(6), p. 363-370.

[2] C.J. Szczepanski, S.K. Jha, J.M. Larsen, and J.W. Jones (2008). *Microstructural Influences on Very-High-Cycle Fatigue-Crack Initiation in Ti-6246.* Metallurgical and Materials Transactions a-Physical Metallurgy and Materials Science, 39A(12), p. 2841-2851.

4 Influence of alpha grain size on fatigue behaviour

This chapter describes the influence of the α grain size on the fatigue behaviour of drawn Ti-6Al-4V wires by comparing the results of fatigue tests on wires with microstructures A, B, C and D. The microstructures of these samples have been shown in Figure 3-1. The average primary α grain diameter, as determined by electron backscatter diffraction (EBSD) measurements on the cross-sections, is approximately 1, 2, 5 and 10 μm for microstructures A, B, C and D, respectively. In the first section of this chapter, the fatigue life data are presented and discussed. Secondly, the different types of obtained fracture surfaces are shown. Finally, for samples with internal crack initiation, the different regions on the fracture surfaces are analysed.

4.1 Fatigue life

A complete overview of the fatigue life data is shown in Figure 4-1. This graph represents, in total, 14 samples with microstructure A, 9 samples with microstructure B, 13 samples with microstructure C and 14 samples with microstructure D. It should be mentioned that the purpose of these tests was not to obtain a complete and statistical representation of the fatigue response over a large stress range. Instead, the tests were performed at stress levels which could lead to internal crack initiation within a reasonable timeframe. The maximum applied stress therefore ranges between approximately 85 and 90% of the 0.2% yield stress of the material (see also Table 3-2). As discussed in section 2.3.7, Ti-6Al-4V shows an anomalous mean stress sensitivity in the HCF and VHCF regime, which means that the fatigue life is generally lower than expected at small positive R ratios. This has also been illustrated in the constant-life diagram in Figure 2-22b, in which the experimental fatigue data are below the Goodman line (equation 2.12). Coupled to this behaviour, there is some experimental evidence in literature that Ti-6Al-4V is more prone to internal crack formation under a mean tensile stress. For this reason, all fatigue tests are performed at a load ratio R of 0.1. It is observed that, in general, the fatigue life decreases if the grain size is increased. This can be seen, for example, by comparing the fatigue lives of samples with microstructure A at 900 MPa with the shorter fatigue lives of samples with microstructure D at 750 MPa and lower. Additionally, at a maximum stress of 750 MPa, all samples with microstructure D break after less than 10^7 cycles, while most samples with microstructure C do not. At this stress level, some samples with microstructure B do not even break after approximately 10^8 cycles. The observation of a decreasing fatigue life with increasing grain size is in agreement with literature, as discussed in section 2.2.4.[1, 2] There is however a rather large variability in fatigue life. This spread of almost two orders of magnitude is not uncommon for Ti-6Al-4V[3-6] and in this case can be explained by the fact that the applied stress level is close to the transition point from surface to interior initiation, the so-called “knee” in the S-N curve (see section 2.2.2).[7-9]

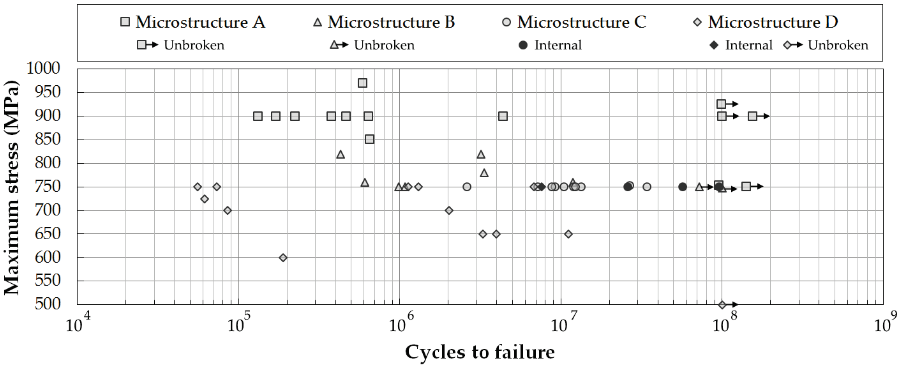

Figure 4-1: Complete overview of fatigue life data for all four microstructures, showing the maximum applied stress (MPa) and the resulting cycles to failure (R=0.1); Unbroken samples (7) are represented by symbols with arrows, samples broken due to internal crack initiation (4) are represented by darker symbols

Another observation regarding the fatigue life data is the occurrence of run-out samples, which are samples that did not break after approximately 10^8 cycles. In fact, for each microstructure the samples appear to form two groups, namely one group with short fatigue lives and one with longer fatigue lives. The latter group includes unbroken samples and samples with internal crack initiation. This is illustrated for microstructures A and D in Figure 4-2. A plausible explanation for this behaviour is the fact that, although the wire surface was relatively free of defects due to the electrochemical polishing treatment, a surface defect could still have been present in certain samples, which would lead to a shorter fatigue life. For example, Figure 4-3 shows the fracture surface of a sample with microstructure D that failed after 7.3 x 10^4 cycles, which is in the short fatigue life group. No facets are found at the initiation site, but instead there is a clear surface defect as indicated by the arrows. As mentioned in section 2.3.2, a similar observation regarding groups with short and long fatigue lives was made by Jha et al.[5], who distinguished between life-limiting, long-lifetime and subsurface failures in forged Ti-6Al-4V. The life-limiting failures showed very short fatigue lives and surface crack initiation with only one facet, whereas the long-lifetime failures showed longer fatigue lives and surface crack initiation with multiple facets. In the current case, the short fatigue life samples do not have a facet at the crack initiation site (see Figure 4-3). On the other hand, the long fatigue life samples do show multiple facets at the initiation site, as is illustrated in Figure 4-4 for a sample with microstructure D that failed after 1.1 x 10^7 cycles. Jha et al.[5] did not provide an explanation for the link between the appearance of the initiation site and the fatigue life in their results. However, in the current work it seems that for some samples the presence of a surface defect led to easy crack initiation due to stress concentration at the defect, which presumably resulted in very short fatigue lives. If the surface is free of large defects, crack initiation must take place by facet formation, either at the surface or in the bulk of the material, which takes more time.

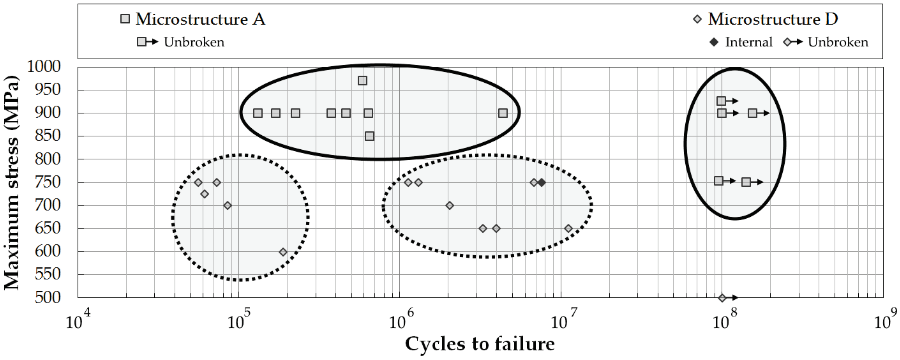

Figure 4-2: Fatigue life data of microstructures A and D, illustrating the separation of data in two groups for each microstructure

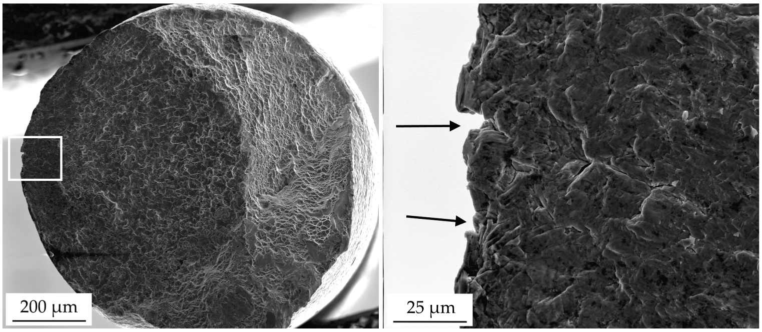

Figure 4-3: Fracture surface of a sample with microstructure D that failed after 7.3 x 10^4 cycles, because of crack initiation at a surface defect

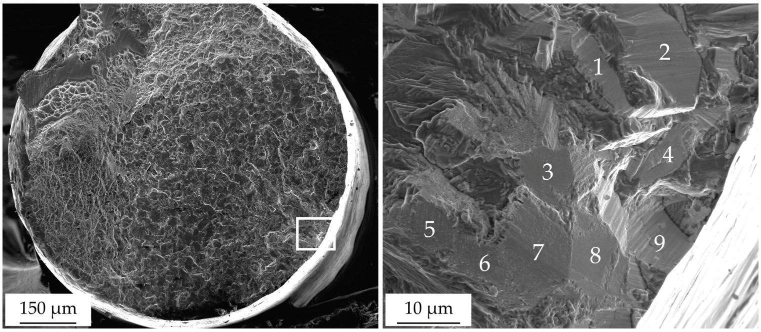

Figure 4-4: Fracture surface of a sample with microstructure D that failed after 1.1 x 10^7 cycles, with multiple facets (9) at the crack initiation site

4.2 Crack initiation location

Four samples failed due to internal crack initiation: three with microstructure C and one with microstructure D. As shown in Figure 4-5, the three samples with microstructure C are named C1, C2 and C3, and they failed after 2.6 x 10^7, 5.7 x 10^7 and 9.6 x 10^7 cycles, respectively. The sample with microstructure D, simply named D, failed after 7.6 x 10^6 cycles. The maximum applied stress for all four samples is 750 MPa. There were no samples with microstructure A or B that failed due to internal crack initiation. However, for these microstructures there were run-out samples (see Figure 4-1). There is a possibility that internal cracks could have been initiating in some of these samples, but did not yet reach a critical size. Additionally, the fatigue life of sample D is about an order of magnitude smaller than the fatigue lives of samples C1, C2 and C3. This would mean that for internal crack initiation, in the VHCF regime, an increase in grain size leads to a decrease in fatigue life, which is also the normal trend in the HCF regime.[1] This is in agreement with the results of Yokoyama et al.[6] As mentioned in section 2.3.4, a larger grain size leads to higher stress fields at dislocation pile-ups, because the increased slip length allows more dislocations to pile up before their back stresses extinguish the dislocation source in the bulk of the grain. This consequently leads to faster crack initiation. The facets would not only be formed faster, but would also be larger, which leads to a higher local stress concentration.

On the other hand, Furuya et al.[4] did not observe an influence of the grain size, which is why they suggested that the projected size of the cluster of facets, or equivalently the rough area, determines the fatigue strength, and not the size of single facets. However, this reasoning does not make sense if the crack initiation and short crack growth phase takes up most of the fatigue life. This can be understood by considering that the projected size of the rough area is not necessarily proportional to the time it takes to form this area. Firstly, it is not known how variable the time to crack initiation is, and secondly, the growth rate of short cracks is not constant, but depends on several factors, such as the grain size (see also section 2.2.3). In one sample, the rough area might be formed rapidly if there is easy crack initiation and short crack growth, while in another sample the formation of the rough area could take more time, even if the projected size of both areas is similar. Therefore it is unlikely that the grain size would not affect the fatigue life. Additionally, it will actually be shown in section 4.3.2 that the projected size of the rough area does not correlate with the fatigue life in the current work.

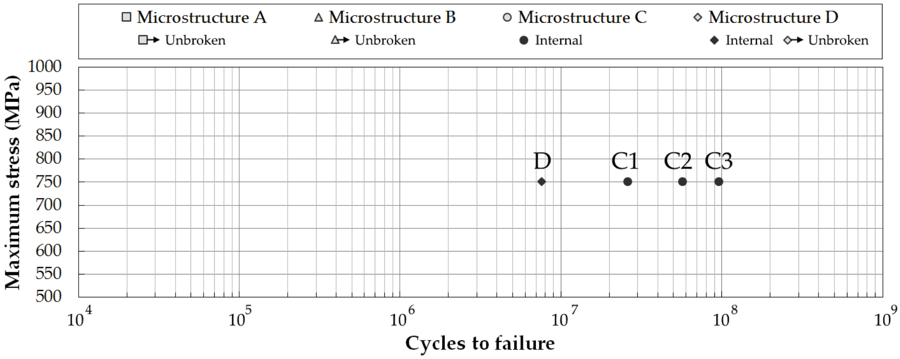

Figure 4-5: Fatigue life data of samples that fractured due to internal crack initiation

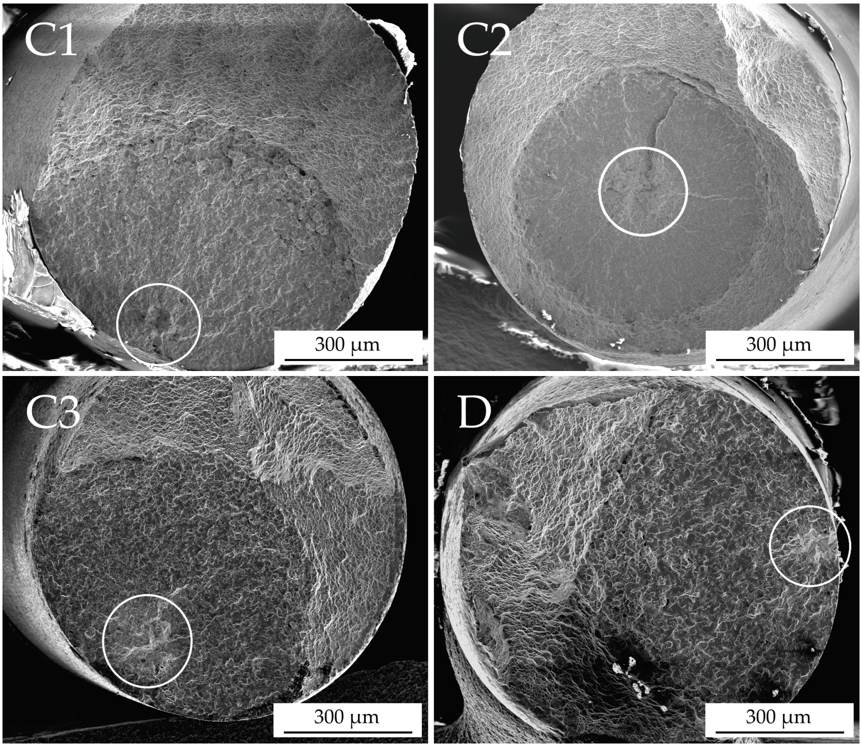

Figure 4-6: SEM images of the fracture surfaces of samples that broke after internal crack initiation, white circles indicate the initiation area; Samples C1, C2 and C3, with microstructure C, broke after 2.6 x 10^7, 5.7 x 10^7 and 9.6 x 10^7 cycles at σ_{max}=750 MPa, respectively; Sample D, with microstructure D, broke after 7.6 x 10^6 cycles at σ_{max}=750 MPa

Regarding the effect of the α grain size on the probability of internal crack initiation, as noticed by Oguma & Nakamura[6], there does not appear to be a clear trend in the results obtained in this study. Internal crack initiation was only found to occur for samples with microstructures C or D, which have the largest grain sizes, approximately 5 and 10 μm, respectively. This seems to confirm the increased probability of internal crack initiation with increasing grain size. However, there is only one sample with microstructure D that failed after internal crack initiation, whereas there are three with microstructure C. In any case, the amount of samples with internal crack initiation is too small to draw any statistically relevant conclusions regarding this correlation.

Finally, the possible relationship between the location of crack initiation and the fatigue life can be considered by comparing samples C1, C2 and C3. The fracture surface of sample C2 shows a fish-eye type failure, whereas the fracture surfaces of samples C1 and C3 show a subsurface-type crack (see Figure 4-6). For sample C2, crack initiation occurred at a depth of approximately 370 μm from the nearest point of the sample surface. By comparing the fatigue life of sample C2 with that of samples C1 and C3 (Figure 4-5), it can be seen that the distance of the initiation location to the edge does not seem to be correlated to the fatigue life, which is in agreement with the results of Yokoyama et al.[10] as discussed in section 2.3.2. This can be explained by the fact that in the VHCF regime crack initiation and short crack growth occupy most of the fatigue life, generally more than 90%.[11] This means that the formation of the rough area with facets dominates the fatigue life, and this process is not dependent on the formation depth as long as it remains subsurface. Once this area is formed, the long crack growth stage takes place, which will be affected by the depth and shape of the crack, as can be described by the geometric factor Y in formula 2.3, but its contribution to the total fatigue life is minimal.

4.3 Analysis of fractographic areas

This section provides the results of the quantification of certain properties of fracture surfaces with internal crack initiation. This includes the measurement of roughness values of different regions by reconstructing the surface topography from tilted SEM images, as described in section 3.2.2. The size of the rough faceted area for samples with internal crack initiation is measured and is used to estimate the threshold stress intensity factor range for long crack growth ΔK_{th}.

4.3.1 Roughness

The crack initiation and short crack growth area has a higher roughness compared to the long crack growth area. This is illustrated in the roughness profile of sample C2 in Figure 4-7. Because crack initiation and short crack growth are strongly influenced by the local microstructure and texture, the crack path is highly tortuous, which leads to a rough fracture surface. During long crack growth, in the Paris regime (see equation 2.4), crack growth is not controlled by the local microstructure, but by the global properties of the material, which leads to a fracture surface with striations and a relatively low roughness.[12] The difference in roughness can also be understood by considering the fact that crack initiation generally occurs in mode II (under the influence of a shear stress), while long crack growth in this case occurs in mode I (due to a normal stress perpendicular to the fracture surface).[4, 13-15]

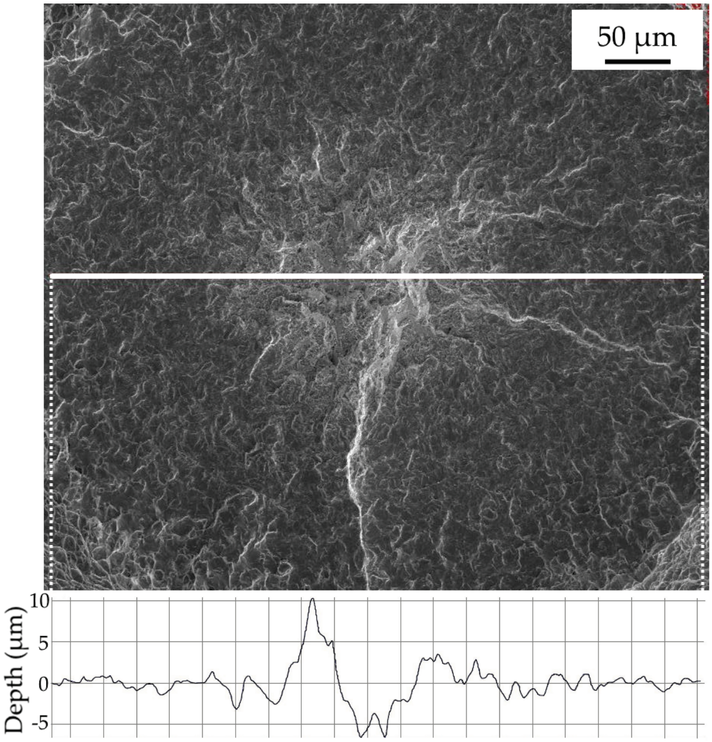

Figure 4-7: Roughness profile of a line through the fracture surface of sample C2, showing the difference in roughness between the central crack initiation and short crack growth area and the surrounding long crack growth area

The roughness of the crack initiation area of different samples can be quantified by area roughness parameters. S_a, which is the average height of the area, and S_q, which is the root mean square height of the area, are determined for the crack initiation area of samples with internal crack initiation (C1, C2, C3 and D). The results are shown in Figure 4-8 as a function of fatigue life. Even though the amount of data is limited, it can be seen that there appears to be a correlation between fatigue life and the roughness of the crack initiation area. This will be discussed further in the next section.

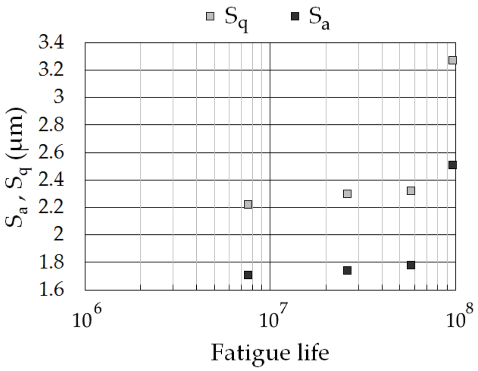

Figure 4-8: Area roughness parameters S_a (average height) and S_q (root mean square height) of the crack initiation area of samples D, C1, C2 and C3 as a function of fatigue life

4.3.2 Threshold for long crack growth

As mentioned in section 2.3.2, several authors have applied Murakami's[16] formula (equation 2.11) to calculate the threshold stress intensity factor range for long crack growth ΔK_{th} in the case of internal crack initiation in titanium alloys. In order to obtain a good estimate for ΔK_{th}, the size of the rough area of initiation and short crack growth has to be defined correctly. One possibility is to approximate this area by an ellipse, as was done by Liu et al.[17] Figure 4-9a illustrates this elliptical area for sample C2. This shape is logical in the case of a spherical short crack growth area around an inclusion in high-strength steel, which is the problem that Murakami et al.[16] investigated in order to derive equation 2.11. However, in the current case there is no reason to assume that the internal crack has an elliptical shape at the transition point from short to long crack growth. Therefore, it would be more logical to assume that this area should be enclosed by a freeform shape that includes all facets, as is illustrated in Figure 4-9b for sample C2.

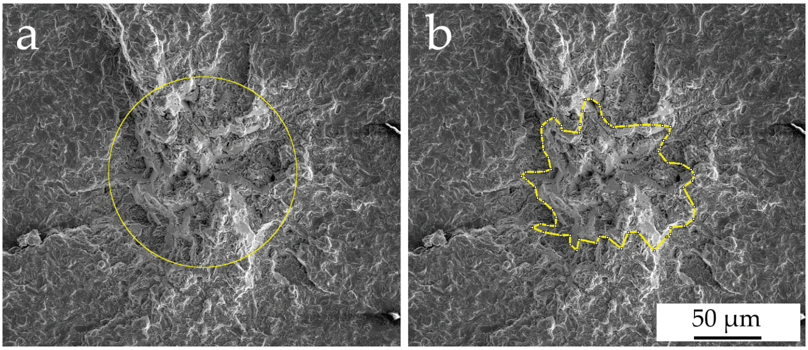

Figure 4-9: Measurement of crack initiation area on fracture surface of sample C2; a) Ellipse; b) Freeform

The ΔK_{th} values for samples C1, C2, C3 and D obtained by using either a freeform or an elliptical area approximation for the rough initiation are shown in Figure 4-10. The secondary axis on this graph also indicates the values for area$^{1/4}$ that were used to calculate ΔK_{th}. The applied stress range is the same for all four samples, which is why the data points can represent both ΔK_{th} and area$^{1/4}$ (see equation 2.11). If an elliptical area selection is used, the ΔK_{th} values are approximately between 6 and 8 MPa√m, which is in agreement with the results of Liu et al.[17] However, with a freeform selection the values are smaller, between 5 and 6 MPa√m, and the difference between the four samples is also slightly smaller. Because the applied stress range $\Delta\sigma$ (and thus also the R ratio) is the same for all samples, ΔK_{th} is approximately constant, so there is no correlation between ΔK_{th} and the fatigue life, which is also consistent with the results of Liu et al.[17] Additionally, there does not appear to be a large difference in ΔK_{th} between samples with microstructure C (C1, C2 and C3) and the sample with microstructure D. However, because only one sample with microstructure D failed due to an internally initiated crack, no definite conclusions can be drawn regarding the influence of the microstructure on ΔK_{th}.

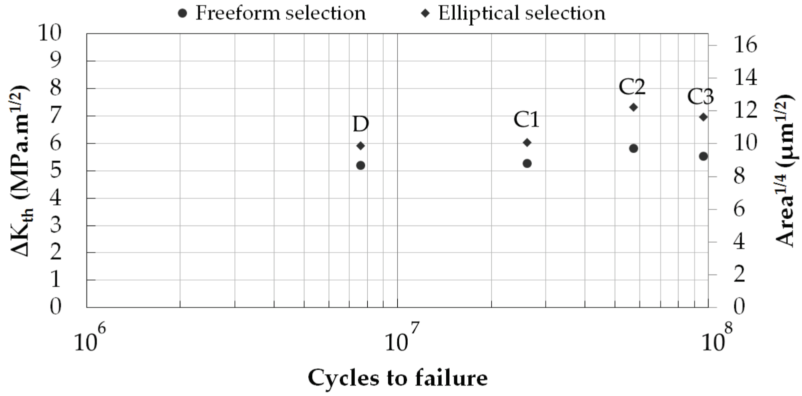

Figure 4-10: ΔK_{th} (or alternatively area$^{1/4}$) values for samples C1, C2, C3 and D, using either a freeform or an elliptical area selection, calculated with equation 2.11; σ_{max}=750 MPa and R=0.1 for all samples

Three important remarks should be made regarding these ΔK_{th} measurements. First of all, for non-spherical cracks the stress intensity factor range is not constant along the crack front. Murakami's formula[16] (equation 2.11), which is utilised to calculate ΔK_{th} values, uses a geometric factor (Y) of 0.5, regardless of the actual shape the of crack. Therefore, this equation is only an approximation for cracks with an arbitrary shape, although Murakami et al.[16] report that the error is less than 10%. Second of all, in the case of Ti-6Al-4V it is difficult to define the exact boundaries of the short crack growth area on the fracture surface. The estimation of the shape of this area introduces an additional error, and the difference between ΔK_{th} values for freeform and elliptical approximations in Figure 4-10 illustrates that this error might be severe. From this point of view, it seems more prudent to regard the ΔK_{th} value from a freeform approximation, which encloses all facets, as a lower limit value, whereas the elliptical approximation most probably leads to an overestimation. Finally, equation 2.11 uses the projected area on a plane perpendicular to the sample axis. As is illustrated in Figure 4-7, this area has a relatively high roughness, which means that the projected area is smaller than the actual surface area.

However, the actual surface area of the crack initiation and short crack growth region can be calculated by combining roughness measurements and measurements of the projected area size. Besides S_a and S_q, the roughness measurements also provide values for the developed interfacial area ratio S_{dr}, which is expressed as the percentage of additional surface area contributed by the topography as compared to an ideal flat plane the size of the measurement region. The actual surface area can then be calculated by using the following equation:

$$Surface\ area = Projected\ area \cdot (1 + S_{dr}) \tag{4.1}$$

The values for the actual surface area of samples C1, C2, C3 and D, with either a freeform or an elliptical selection, are plotted as a function of fatigue life in Figure 4-11. In contrast to the projected area (see Figure 4-10), the actual surface area does appear to be related to the fatigue life.

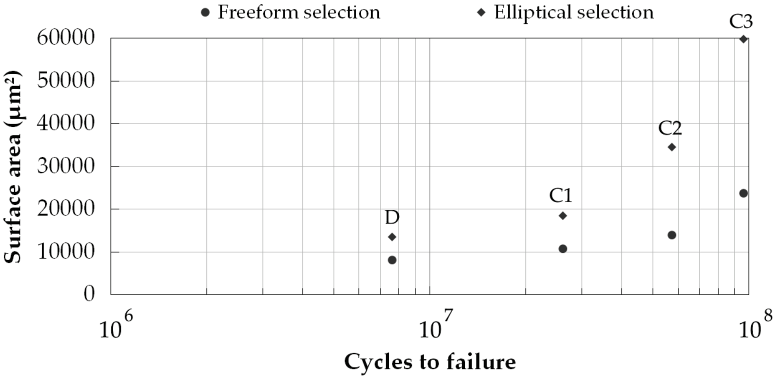

Figure 4-11: The actual surface area of the initiation region of samples C1, C2, C3 and D as a function of fatigue life

At this point, it is therefore necessary to consider the relevance of attempting to determine ΔK_{th} with equation 2.11 in the case of internal crack initiation in Ti-6Al-4V in the VHCF regime. For high strength steels, calculating ΔK_{th} with this equation is useful to understand the effect of the inclusion size on fatigue life. However, for Ti-6Al-4V there is no inclusion at the initiation site, and the projected size of the rough area, which is not clearly defined, does not seem to be correlated with the fatigue life. On the other hand, the actual surface area of the initiation and short crack growth region, which takes into account the roughness, does appear to be linked to the fatigue life (see Figure 4-8 and Figure 4-11). From these results, it is clear that the projected threshold size of the crack initiation and short crack growth area is not relevant with regard to the fatigue life. However, the roughness of this area, which is controlled by crack initiation and short crack growth mechanisms, is an important link to understanding the fatigue life. To the author's knowledge, the relation between the roughness of the initiation area (or equivalently the actual surface area) and the fatigue life has not yet been reported elsewhere. Easy crack initiation and short crack growth without much deflection in the crack path leads to a low roughness and correspondingly a short fatigue life. On the other hand, difficult crack initiation and short crack growth with a highly deflected crack path leads to an effectively larger fractured surface area, a higher roughness and a longer fatigue life. Therefore, the key to understanding the variability of the fatigue life of Ti-6Al-4V in the VHCF regime, is to understand these mechanisms.

4.4 Conclusions

In general, the fatigue life of drawn Ti-6Al-4V wires decreases as the alpha grain size increases. There is a large variability in fatigue life, partially because the applied stress range was chosen to be close to the transition point from surface to internal crack initiation, which forms a so-called knee in the S-N curve. The fatigue life data can be separated into two groups for each microstructure. The first group contains samples with short fatigue lives, most probably because they contained surface defects, which lead to easy crack initiation. The second group contains samples with longer fatigue lives, and also includes samples with internal crack initiation and run-out samples. In these samples, cracks initiated due to facet formation. Four samples broke due to an internal crack: three samples with microstructure C, which failed after 2.6×10^7, 5.7×10^7 and 9.6×10^7 cycles, and one sample with microstructure D, which failed after only 7.6×10^6 cycles. The general trend of a decreasing fatigue life with increasing alpha grain size also appears to be valid for internal crack initiation in the VHCF regime. The depth of crack initiation is not correlated to the fatigue life.

The crack initiation and short crack growth area has been characterized in terms of size and roughness. The projected area size, which can be used to estimate ΔK_{th}, is not linked to the fatigue life. The values for ΔK_{th} are found to be between 6 and 8 MPa√m if an elliptical shape is used to approximate the area, which is consistent with literature. Lower values are obtained if a freeform approximation, which includes all facets, is used. The method that is used to calculate ΔK_{th} from the area size is expected to lead to a significant error margin. The area roughness is found to be higher if the fatigue life is longer. Additionally, the actual surface area of the crack initiation and short crack growth region, which takes into account the roughness, is also related to the fatigue life. This correlation has not yet been reported elsewhere, to the author's knowledge, and proves that crack initiation and short crack growth mechanisms are controlling the fatigue life in the VHCF regime. This observation further stresses the importance of understanding the mechanisms of facet formation and short crack growth in Ti-6Al-4V.

4.5 References

[1] J.J. Lucas (1973). *Titanium Science and Technology*. Vol. 3. Plenum Press, New York. p. 2081.

[2] G.Q. Wu, C.L. Shi, W. Sha, A.X. Sha, and H.R. Jiang (2013). *Effect of microstructure on the fatigue properties of Ti-6Al-4V titanium alloys.* Materials & Design, 46, p. 668-674.

[3] T. Akahori and M. Niinomi (1998). *Fracture characteristics of fatigued Ti-6Al-4V ELI as an implant material.* Materials Science and Engineering a-Structural Materials Properties Microstructure and Processing, 243(1-2), p. 237-243.

[4] Y. Furuya and E. Takeuchi (2014). *Gigacycle fatigue properties of Ti-6Al-4V alloy under tensile mean stress.* Materials Science and Engineering A, 598, p. 135-140.

[5] S.K. Jha, C.J. Szczepanski, P.J. Golden, W.J. Porter, and R. John (2012). *Characterization of fatigue crack-initiation facets in relation to lifetime variability in Ti-6Al-4V.* International Journal of Fatigue, 42, p. 248-257.

[6] H. Oguma and T. Nakamura (2010). *The effect of microstructure on very high cycle fatigue properties in Ti-6Al-4V.* Scripta Materialia, 63(1), p. 32-34.

[7] S.K. Jha and K.S.R. Chandran (2003). *An unusual fatigue phenomenon: duality of the S-N fatigue curve in the beta-titanium alloy Ti-10V-2Fe-3Al.* Scripta Materialia, 48(8), p. 1207-1212.

[8] N.E. Paton, J.C. Williams, J.C. Chesnutt, and A.W. Thompson (1975). *The effects of microstructure on the fatigue and fracture of commercial titanium alloys.* AGARD Conference Proceedings, 185, p. 4-1 - 4-14.

[9] O. Umezawa and K. Nagai (1997). *Subsurface crack generation in high-cycle fatigue for high strength alloys.* ISIJ International, 37(12), p. 1170-1179.

[10] H. Yokoyama, O. Umezawa, K. Nagai, and T. Suzuki (1997). *Distribution of internal crack initiation sites in high-cycle fatigue for titanium alloys.* Isij International, 37(12), p. 1237-1244.

[11] V. Kazymyrovych (2009). *Very high cycle fatigue of engineering materials: A literature review.* Karlstad University Studies, 22.

[12] R.O. Ritchie (1977). *Influence of microstructure on near-threshold fatigue-crack propagation in ultra-high strength steel.* Metal Science, 11, p. 368-381.

[13] A. Nikitin, C. Bathias, and T. Palin-Luc (2015). *A new piezoelectric fatigue testing machine in pure torsion for ultrasonic gigacycle fatigue tests:*

application to forged and extruded titanium alloys. Fatigue & Fracture of Engineering Materials & Structures, 38(11), p. 1294-1304.

[14] S. Ankem, H. Margolin, C.A. Greene, B.W. Neuberger, and P.G. Oberson (2006). *Mechanical properties of alloys consisting of two ductile phases.* Progress in Materials Science, 51(5), p. 632-709.

[15] A. Nikitin, C. Bathias, T. Palin-Luc, and A. Shanyavskiy (2016). *Crack path in aeronautical titanium alloy under ultrasonic torsion loading.* Frattura ed Integrità Strutturale, 35, p. 213-222.

[16] Y. Murakami, S. Kodama, and S. Konuma (1989). *Quantitative-evaluation of effects of non-metallic inclusions on fatigue-strength of high-strength steels. I:Basic fatigue mechanism and evaluation of correlation between the fatigue fracture-stress and the size and location of non-metallic inclusions.* International Journal of Fatigue, 11(5), p. 291-298.

[17] X. Liu, C. Sun, and Y. Hong (2015). *Effects of stress ratio on high-cycle and very-high-cycle fatigue behavior of a Ti-6Al-4V alloy.* Materials Science and Engineering A, 622, p. 228-235.

5 Alpha facets

Internal crack initiation in Ti-6Al-4V occurs because of the formation of facets, which are planar cracks in single α grains. The previous chapter illustrates the importance of understanding the formation mechanism of these α facets, because this is a controlling factor regarding the fatigue life. Therefore, this chapter provides an in-depth characterisation of the facets that are observed at internal crack initiation sites. The facets are characterized in terms of their appearance, with surface markings, their spatial orientation and their crystallographic orientation, which is determined in a non-destructive and a destructive manner. These characteristics are then used to reflect on the possible facet formation mechanisms that have been suggested in literature.

5.1 Surface markings

As mentioned in section 4.2, there are three samples with microstructure C (C1, C2 and C3) and one sample with microstructure D that broke due to internal crack initiation. The crack initiation areas of these samples are shown in Figure 5-1. The initiation areas are very similar for all four samples, and they contain many facetted α grains. The facets on the fracture surface of sample D are larger, because the α grain size is larger for microstructure D in comparison to microstructure C, as has been shown in section 3.1.1.

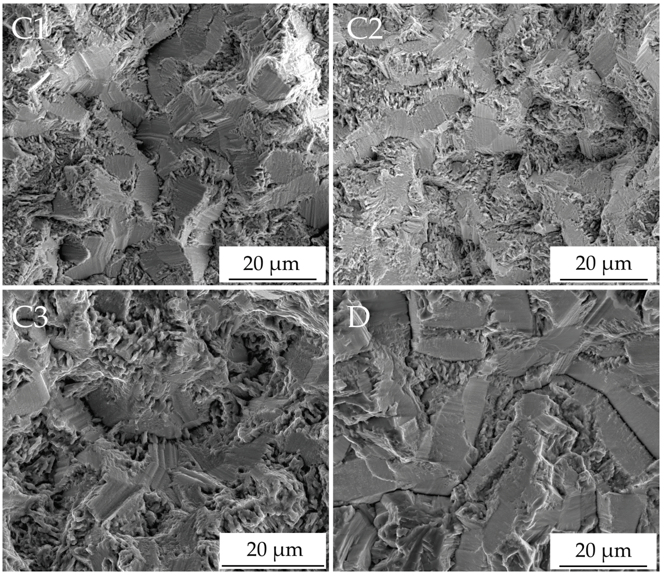

Figure 5-1: SEM images of the crack initiation area of samples that broke after internal crack initiation; Samples C1, C2 and C3, with microstructure C, broke after 2.6 x 10^7, 5.7 x 10^7 and 9.6 x 10^7 cycles at σ_{max}=750 MPa, respectively; Sample D, with microstructure D, broke after 7.6 x 10^6 cycles at σ_{max}=750 MPa

SEM images of the facets at a higher magnification reveal the presence of nano-roughness or markings. This observation is interesting, because most publications describe facets as being flat and smooth, as mentioned in section 2.3.3. There are only a few cases in which radial patterns with featherlike features have been noticed on facets,[1-4] and one case in which slip-like patterns were observed on a facet in a near-β Ti-22V-4Al alloy.[5] Figure 5-2 shows a selection of images of markings on facets at internal crack initiation sites.

Figure 5-2a illustrates the roughness of a facet on the fracture surface of sample C2. This roughness consists of very fine and linear markings, which could be the result of slip activity on parallel slip planes. Figure 5-2b and c are taken from both opposite fracture surfaces of sample C2, at the same location. The white ellipses indicate non-linear markings on the facets. Interestingly, on one fracture surface it appears that the pattern consists of material on top of the facet (Figure 5-2b), whilst on the opposing fracture surface the same pattern appears to be pressed into the facet (Figure 5-2c), which could suggest that some material was transferred between the two opposing crack surfaces. The appearance of these markings draws similarities with galling and cold welding patterns seen in adhesive wear. The presence of a wear mechanism during internal fatigue crack initiation and short crack growth in Ti-6Al-4V has already been suggested by McEvily et al.,[6] as was mentioned in section 2.3.6. Additionally, the rounded fractographic features, which were observed by both McEvily et al.[6] and Oguma et al.[7] as shown in Figure 2-21, are also present in between facets in this case.

Figure 5-2d shows a secondary crack, which partly consists of a facet, on the fracture surface of sample C1. These "secondary facets" are observed at the crack initiation sites of all four samples, and they form short crack paths that most likely got blocked by certain microstructural barriers. Figure 5-2e represents typical facets with linear markings at the crack initiation site of sample D. In contrast, this sample also contains one "anomalous" facet with a fan-shaped pattern, as shown in Figure 5-2f. This pattern could be the result of a cleavage-type fracture mechanism.[2] The relation between these different markings and possible facet formation mechanisms will be discussed in more detail in section 5.4.

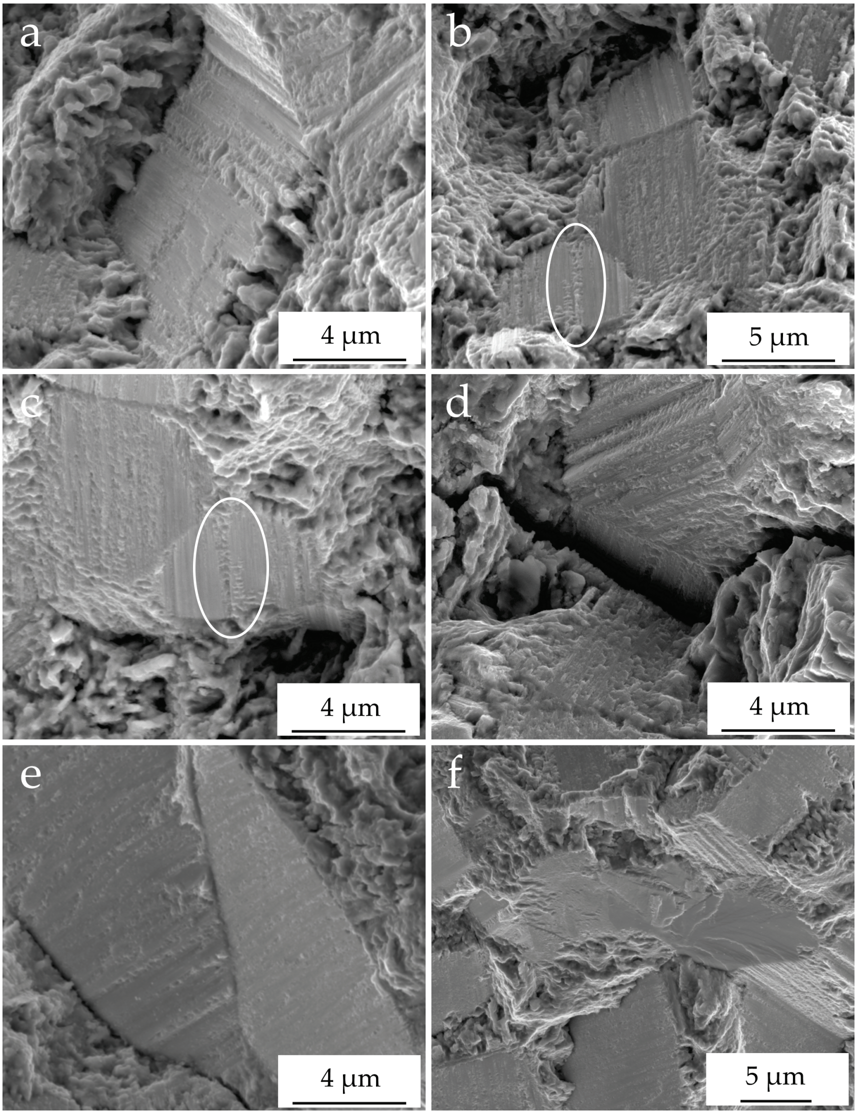

Figure 5-2: SEM images of facets at crack initiation sites; a) Nano-roughness on a facet of sample C2; b-c) Images taken at the same location on both opposite fracture surfaces of sample C2, showing facets with corresponding markings (indicated by white ellipses); d) Secondary faceted crack in sample C1; e) Typical linear patterns on facets of sample D; f) Facet with an anomalous, fan-shaped pattern in sample D

5.2 Spatial angle distribution

The topography of crack initiation areas can be reconstructed in 3D from tilted SEM images, as is described in section 3.2.2. This reconstruction can then be used to measure the angles of facet planes. For these measurements, the facet plane angle is defined as the angle between the facet plane normal and the wire axis, as is illustrated in Figure 5-3.

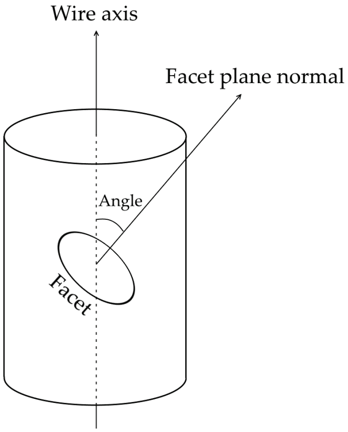

Figure 5-3: Definition of facet plane angle

The facet plane angles have been measured for samples C1, C2 and D. The fracture surfaces of samples C1, C2 and D contain 47, 46 and 40 facets, respectively. The facet plane angle distributions for these samples are presented in Figure 5-4. This graph shows the percentage of facets that lie in a specified angle range. A first observation is that the distribution of facet angles is very similar for all three samples. The highest percentage of facets lie at angles between 55 and 65 degrees for samples C1 and C2. For sample D, there is an equal amount of facets in the 45-55 degrees and 55-65 degrees range. A second interesting observation is the lack of facets at angles lower than 35 degrees. The spatial angles of facets in these samples deviate from the facet angles found in similar publications (see section 2.3.3). Jha et al.[8] reported that the majority of facet angles for a fish-eye sample were between 30 and 60 degrees, while Bantounas et al.[9] found that the angles of initiation facets for a subsurface-initiated sample were between 15 and 40 degrees. These angles are considerably smaller than those found in this work. Evans and Bache[10, 11] even found facets that were perpendicular to the loading axis, which means that they were at zero degrees according to the definition used here (Figure 5-3).

The difference in facet angles between the current results and those found in literature can most likely be explained by the difference in crystallographic texture. As was mentioned in section 2.3.3, facets form on certain crystallographic planes. Therefore, it is logical that the texture affects the facet plane angles. The mentioned authors used forged or rolled Ti-6Al-4V for fatigue testing, while drawn wires were used in the current work. One particular example of the textural differences between these material forms, is that the drawn wires contain nearly no grains with their c-axis parallel to the loading axis (see section 3.1.2), which is not the case for the forged or rolled material that was used by Bantounas et al.[9] The link between facet angles and the crystallographic texture will be discussed further in section 5.3.1.

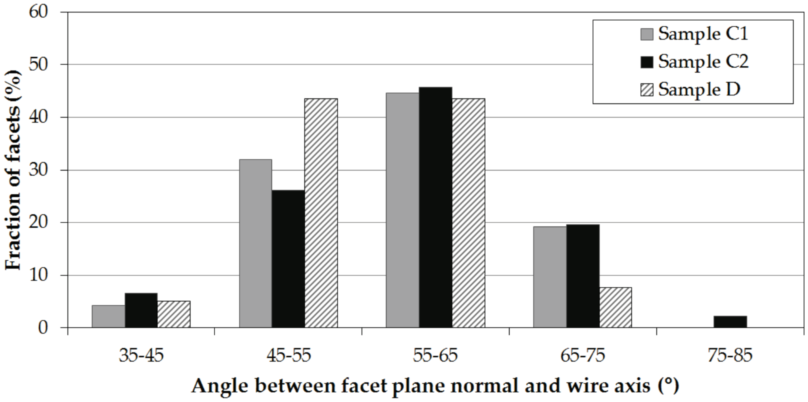

Figure 5-4: Distribution of facet plane angles for samples C1, C2 and D

The facet plane angles could provide an insight into the loading conditions that were present during facet formation, as was also mentioned in section 2.3.3. Jha et al.[8] found angles between 30 and 60 degrees, and they argue that the faceted grains are suitably oriented for shear because the shear stress should be maximum at 45 degrees. On the other hand, authors who found facets at lower angles logically assume that facet formation requires a combination of a moderate shear stress and a high tensile stress perpendicular to the plane on which the facet forms.[9, 12] In the case of Evans and Bache,[10, 11] the facet angles are around 0 degrees, which would mean that they were formed under high tensile stress and very low shear stress conditions. However, their model (see Figure 2-18) assumes that shear stress is induced by a slip band in a neighbouring grain.

Regardless of whether this model is correct or not, it raises an important question regarding the actual local stress conditions during facet formation. The observation of facet angles around 60 degrees, as shown in Figure 5-4, might lead to the assumption that a moderately high shear stress and a rather low tensile stress was present on the plane on which facet formation took place. However, this assumption is not necessarily correct, because it does not take into account the fact that the stress distribution is not uniform at the microscale, due to the orientation of neighbouring grains. For example, crystal plasticity modelling by Dunne et al.[13, 14] showed a variation in tensile stress of several hundred MPa for certain grain orientation combinations. Additionally, the stress also varies inside grains, or more specifically close to grain boundaries. Therefore, it is too simplistic to assume specific stress conditions based on the facet plane angles. The effect of the orientation of neighbouring grains on facet formation will be investigated in section 6.1.

Finally, the angles of facets can have an effect on crack closure during crack growth. In planar slip materials such as Ti-6Al-4V, roughness induced crack closure is in fact the dominant closure mechanism for crack growth in the near threshold regime.[15] The effect of the crack angle on the roughness induced crack closure level has been studied by Parry et al.[16] by finite element modelling. They simulated the growth of a through-thickness fatigue crack in the centre of a plate, using five different crack geometries: an undeflected crack, and cracks that undergo periodic deflections of 15°, 30°, 45° and 60°. By investigating the deformed finite element mesh, they could identify the crack opening and closure levels for each crack geometry. From these simulations, they found that the crack closure level strongly increased with the deflection angle, which has also been confirmed by Kibey et al.[15] Additionally, crack closure did not occur simultaneously at all points, due to residual plastic strain in the crack wake, as is illustrated in Figure 5-5, which shows the deformed finite element mesh for a crack that is periodically deflected at 45 degrees. This results in sliding contact and friction between the crack faces during loading and unloading. If the crack deflection angle is higher, there is more crack closure and more friction between the crack faces.

Although the model of Parry et al.[16] uses idealised crack geometries, it is likely that similar crack closure effects are occurring in the case of an internal faceted crack in the current work, and that higher facet angles would result in higher crack closure levels. Therefore, it is plausible that some of the markings that have been observed on facets (Figure 5-2b and c) are indeed wear markings due to crack face sliding. The occurrence of wear markings on facets in this work and the absence of these markings on facets in other publications, as mentioned in section 2.3.3, can be related to the steeper facet plane angles, which in turn are dependent on the crystallographic texture. It is important to mention that crack closure can indeed occur at a positive load ratio of 0.1,[17] which was applied for all fatigue tests in this work. Additionally, it should be noted that roughness induced crack closure is not expected to be significant when the crack is confined to a single grain.[18] This means that in this case, wear between the crack faces would only take place when the crack already comprises several facets.

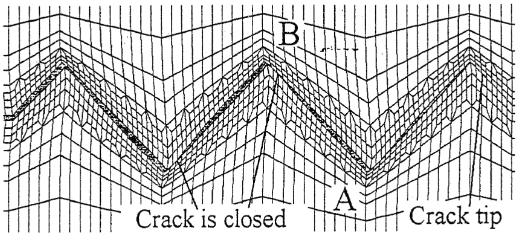

Figure 5-5: Deformed finite element mesh of a growing crack that is periodically deflected at 45° [16]

5.3 Crystallographic planes

Alpha facets are generally found to form on certain crystallographic planes. As mentioned in section 2.3.3, this can be either the basal plane, a near-basal plane, a prismatic plane or a pyramidal plane (see also Figure 2-5). In order to understand how facets are formed, it is important to find out which crystallographic planes coincide with the facet planes. One way to do this, non-destructively, is by comparing the crystallographic texture of the wires with the facet plane angle distribution. However, this will only provide global statistical information for all facets in general, without considering individual facets. A more rigorous approach, which is destructive and more time-consuming, is to make sections through the fracture surface with a focused ion beam (FIB) and perform EBSD measurements on these sections. This provides information about the orientation of specific facets, and can also expose secondary faceted cracks (see Figure 5-2d). Both methods will be explored in the following sections.

5.3.1 Non-destructive determination from texture

The crystallographic texture of the Ti-6Al-4V wires that have been used in this work can be represented by pole figures, which are shown in Figure 3-3 for all four microstructures. These pole figures show that the texture is quite well-defined and axisymmetric. As a result, it is possible to couple this information with the measurements of the facet plane angles, as shown in Figure 5-4, in order to obtain some qualitative insights into which crystallographic planes should coincide with the facet planes. The $\{10\bar{1}0\}$ pole figure that represents the texture for microstructure D, and which can also be found in Figure 3-3d, is presented again in Figure 5-6a. Figure 5-6b shows the orientation of the hexagonal lattice which represents the two most prominent texture features, being the normal direction of the $\{10\bar{1}0\}$ planes parallel to the wire axis, and the normal direction of the $\{10\bar{1}0\}$ planes rotated approximately 60 degrees from the wire axis. The position of the points that would represent the six prismatic planes on the pole figure are indicated in this figure by numbers one to six. It is clear that this orientation, together with the equivalent orientations that involve a rotation around the wire axis, does indeed represent the texture.

The facet plane angle distributions in Figure 5-4 show that most facets form an angle of approximately 60 degrees with respect to the normal direction. By comparing this information with the crystallographic texture, it is reasonable to state that most facets were formed on one of the prismatic planes oriented with the normal direction rotated 60 degrees from the wire axis (planes 2, 3, 5 and 6 in Figure 5-6b). It is interesting to note that in this case no facets seem to have formed on the prismatic planes numbered 1 and 4, since these would have had an angle of approximately 0 degrees with respect to the normal direction and such angles have not been measured. This observation will be discussed further in section 5.4.

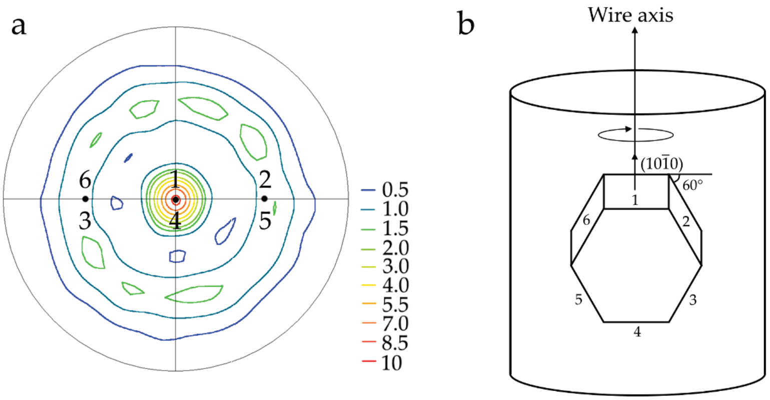

Figure 5-6: a) $\{10\bar{1}0\}$ pole figure for microstructure D, with positions of six prismatic planes for orientation shown in b; b) Representation of crystal orientation present in the texture, and the six prismatic planes in the hexagonal lattice

5.3.2 Destructive determination by FIB milling and EBSD

In order to obtain the crystallographic orientation of individual facets, sections of the fracture surfaces have been made by FIB milling, which were then analysed by EBSD. This FIB sectioning is illustrated in Figure 5-7, which also shows the definition of the sample coordinate system (x_s-y_s-z_s). The FIB-milling plane coincides with the x_s-y_s plane.

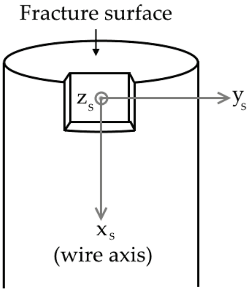

Figure 5-7: Illustration of FIB sectioning through a fracture surface, and definition of sample coordinate system x_s-y_s-z_s

In total, 10, 10 and 18 facets have been examined for samples C1, C3 and D, respectively. For samples C1 and C3, all of the inspected facets coincide with a prismatic lattice plane. This is illustrated in Figure 5-8 for one section through sample C3. The top view of the fracture surface (Figure 5-8a) shows that this section contains one facet. Figure 5-8b shows the FIB-milling plane that cuts through this facet. The position of the latter is indicated by two arrows. The facet forms an angle of approximately 60° with the plane perpendicular to the wire axis. The orientation map from an EBSD measurement on this FIB-section in Figure 5-8c indicates that the facet plane is parallel to a prismatic lattice plane.

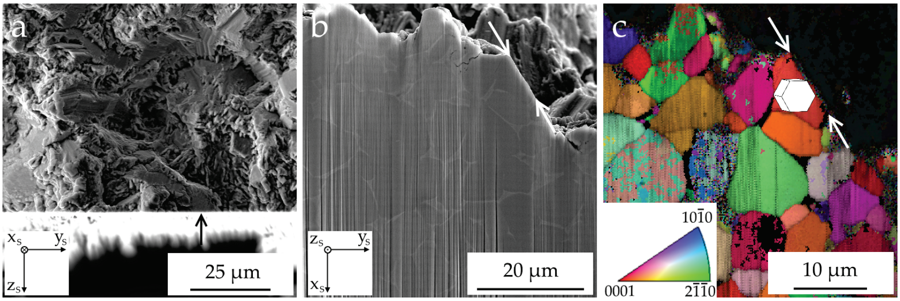

Figure 5-8: a) Top view SEM image of fracture surface of sample C3, showing where the FIB cross-section was made, and the location of the sectioned facet (indicated by the arrow); b) Front view SEM image of the cross-section; c) Colour coded orientation map for the α phase obtained by EBSD on the cross-section (reference direction z_s), with hexagonal unit cell to illustrate the orientation of the sectioned facet

For sample D, all examined facets coincide with a prismatic lattice plane, except for the facet that has an anomalous, fan-shaped pattern (see Figure 5-2f). Figure 5-9 shows the analysis of one section through two "regular" facets in sample D. Both facets are parallel to a prismatic lattice plane, as can be seen in the orientation map in Figure 5-9d. The roughness on these facets has a linear appearance, as was mentioned in section 5.1 and also shown in Figure 5-2e. A close-up view of the examined cross-section (Figure 5-9e) shows that this linearity coincides with the slip direction in the prismatic slip system, which is $\langle 11\bar{2}0\rangle\{10\bar{1}0\}$. This observation strongly suggests that prismatic slip is involved in the formation of these facets, as will be discussed further in section 5.4.

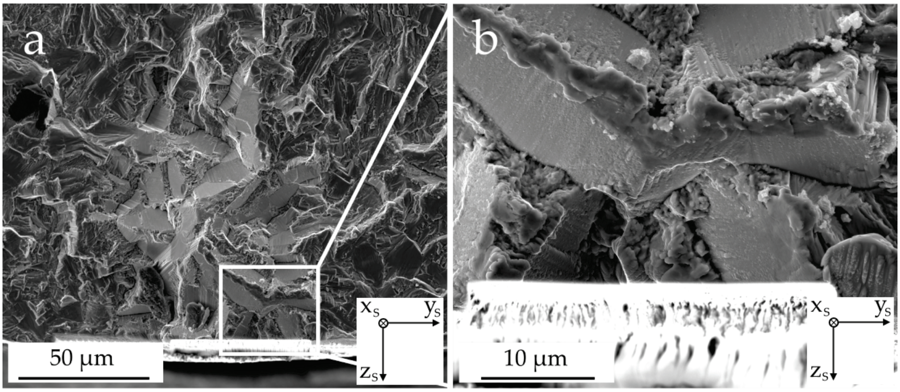

Figure 5-9: a) Top view SEM image of the fracture surface of sample D; b) Close-up top view SEM image, showing the position of the FIB cross-section

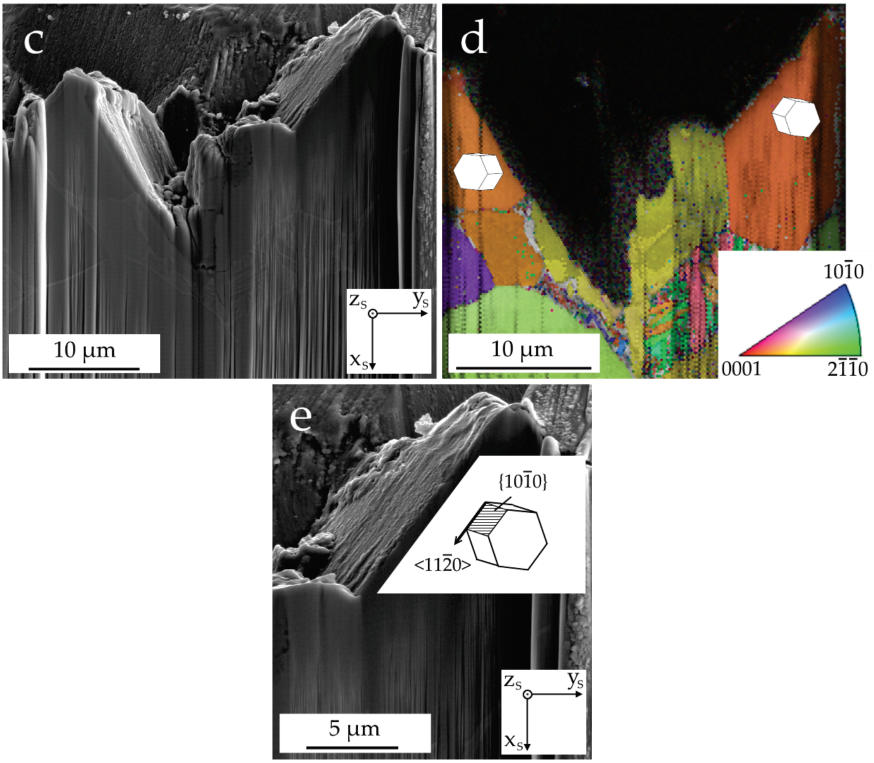

Figure 5-9 (continued): c) Front view SEM image of the cross-section; (d) Colour coded orientation map for the α phase obtained by EBSD on the cross-section (reference direction z_S), with hexagonal unit cells to illustrate the orientation of the two sectioned facets; (e) Close-up front view SEM image of one of the sectioned facets, illustrating the orientation of the prismatic slip system in this facetted grain

It is important to mention that these markings are not traces of active slip planes, which are sometimes observed at the surface of a metal after plastic deformation, because in the current case the facet is parallel to a slip plane. Instead, the markings are plausibly caused by cyclic deformation on a slip band along the slip direction.

The roughness on the anomalous facet of sample D, which is shown in Figure 5-2f, is not linear, but instead forms a fan-shaped pattern. This facet has also been sectioned in order to measure its crystallographic orientation. The results of this measurement are presented in Figure 5-10. The orientation map in Figure 5-10c shows that in this case, the facet plane has a near-basal orientation. This near-basal orientation, together with the fan-shaped markings, suggest that in this case a cleavage mechanism could have caused facet formation. This will also be discussed further in section 5.4. Please note that the grain with a yellow colour at the top of Figure 5-10c could be mistaken for being a facet, which extends from the anomalous facet. However, a comparison with Figure 5-10a shows that this is not the case, since there is no facet at this position.

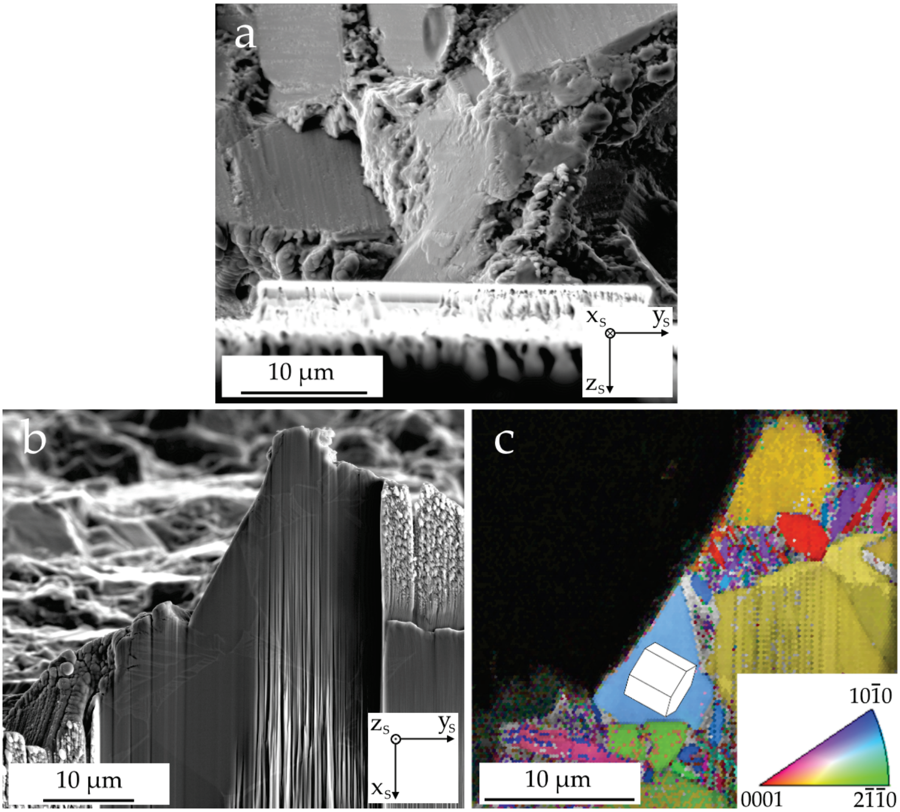

Figure 5-10: Top view SEM image of the fracture surface of sample D, showing the position of the FIB cross-section; b) Front view SEM image of the cross-section; c) Colour coded orientation map for the α phase obtained by EBSD on the cross-section (reference direction z_S), with hexagonal unit cell to illustrate the orientation of the sectioned anomalous facet

The fracture surfaces of all four samples also contain secondary cracks, as is illustrated in Figure 5-2d. Some of these secondary cracks are revealed in Figure 5-11, which shows a cross-section through the fracture surface of sample D and the corresponding orientation map. A first observation is that these secondary facets (formed by the secondary cracks) also coincide with prismatic lattice planes. Secondly, it can be seen that only one of the three inspected secondary facets is connected directly to the fracture surface. In other words, the other two secondary facets appear to be isolated from the main crack. Liu et al.[19] found a similar secondary isolated crack below the fracture surface. However, in their sample the crack was found to span several grains, while in the section shown in Figure 5-11 the isolated cracks seem to be contained within separate α grains. The orientation measurements of grains with secondary facets can be used to investigate the effect of grain boundaries or β phase regions on early stage crack growth. This will be explored further in section 6.2.

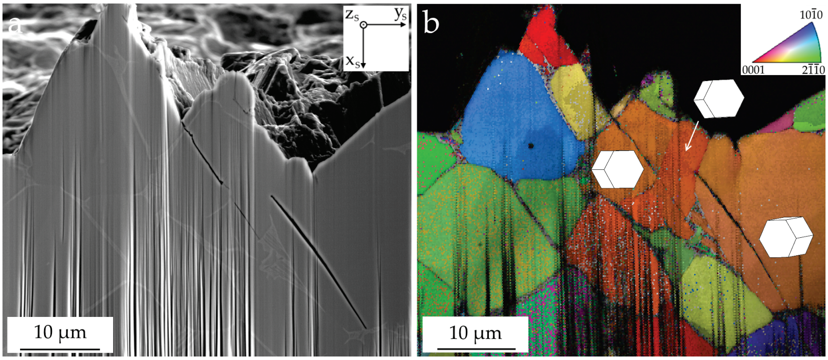

Figure 5-11: a) Front view SEM image of a FIB cross-section of sample D, showing secondary facets; b) Colour coded orientation map for the α phase obtained by EBSD on the cross-section (reference direction z_S), with hexagonal unit cells to illustrate the orientation of the grains that contain secondary facets

Besides secondary facets, some cross-sections reveal grains in which other interesting phenomena are occurring. Three cross-sections are presented in Figure 5-12, together with illustrative drawings that show the grain boundaries (dotted lines), α+β regions (grey areas) and grain orientations (hexagonal unit cells) of certain grains. Figure 5-12a shows a section through the fracture surface of sample C1. It can be observed that there is a facet in grain 1, parallel to a prismatic plane, and a facet that goes through both grains 3 and 4, also parallel to a prismatic plane in both grains. This second facet illustrates that facets can initiate in one grain, and grow through the grain boundary into a neighbouring grain (see also section 6.2). Both facets have encountered a β phase region containing secondary α, which is plausibly acting as an obstacle to crack growth. This could be caused by either the β phase, which plastically deforms more easily and thus leads to crack tip blunting, or by the secondary α grains, which have varying crystallographic orientations (see Figure 3-5) and therefore would deflect the crack path repeatedly. Grain 3 shows evidence of plastic deformation and damage in the region between both facets, with apparent void nucleation, which is most probably caused by the high stress fields around the crack tips. Therefore, this image probably shows the ongoing process of crack coalescence between two facets.

Figure 5-12b presents another section through sample C1. Again, it can be seen that there has been plastic deformation around the secondary crack in grain 1, which is connected to a facet on the fracture surface. Additionally, this section shows several fine lines in grain 1, parallel to a prismatic plane, which could point to the early stages of facet formation due to the development of prismatic slip bands. More interestingly, these fine lines extend through the grain boundary with only a slight deflection into grain 2, in which they are parallel to the basal plane. This means that first of all basal slip is possible, and second of all slip transfer between grains with basal and prismatic slip may occur. Figure 5-12c shows a section through the fracture surface of sample C3, which reveals early stage facet formation in grains 1 and 2 along prismatic planes, and apparent void nucleation in grain 3. An interesting observation on this section is the fact that slip band formation does not seem to be limited to one crystallographic plane per grain. The main facet is forming on prismatic planes in grains 1 and 2, but there appear to be side branches from this main facet on a different prismatic plane in grain 1 and on either the basal plane or a different prismatic plane in grain 2. Finally, it is important to consider that these sections only provide two-dimensional information, which means that any explanation that is based on this information should be regarded with prudence.

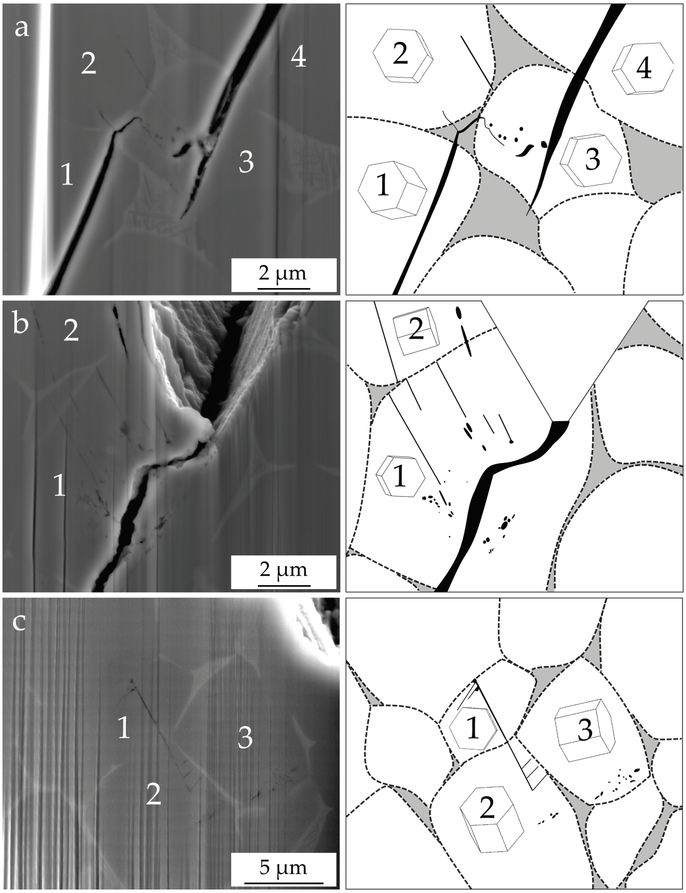

Figure 5-12: SEM images of FIB cross-sections, together with sketches, which outline the grain boundaries (dotted lines) and α+β regions (grey areas), and hexagonal unit cells to illustrate grain orientations; a) Cross-section through sample C1, showing crack coalescence between two facets occurring in grain 3; b) Cross-section through sample C1, showing early stages of crack initiation and possible slip transfer in grains 1 and 2; c) Cross-section of sample C3, showing early stages of crack initiation on multiple planes and possible slip transfer in grains 1 and 2

5.4 Facet formation mechanisms

The properties of facets at internal crack initiation sites, which have been investigated in the previous sections, can be used to reflect on the facet formation mechanisms that have been proposed in literature. As mentioned in section 2.3.3, the suggested facet formation mechanisms can generally be categorized in two groups: mechanisms in which facets are formed by cleavage of single α grains and mechanisms in which dislocation slip in certain grains leads to facets. In order to distinguish between these two different mechanisms, it is important to identify on which crystallographic planes the facets have formed. If facets are the result of dislocation slip and slip band formation, then they should concur with a certain slip system of the α phase. On the other hand, if they are formed by cleavage, then they should coincide with a cleavage plane. The basal, prismatic and pyramidal slip systems of the α phase are illustrated in Figure 2-5 and Table 2-2. Regarding cleavage, Wanhill[20] reported that the cleavage planes in the α phase are consistently found to be planes approximately 15° from the basal plane, i.e. near-basal.

The results in section 5.3 show that, in nearly all cases, the facet planes are parallel to a prismatic plane. Furthermore, Figure 5-9e illustrates that the linear markings, which are also present on nearly all facets, coincide with the slip direction in the prismatic slip system. Therefore, it is very likely that these facets are the result of prismatic slip and slip band formation. The observations of early stage facet formation in Figure 5-12 confirm this mechanism. On the other hand, there is one anomalous facet in sample D, which has a near-basal orientation (Figure 5-10) and a fan-shaped pattern instead of linear markings (Figure 5-2f). Similar radial patterns or featherlike features have been observed in literature, as mentioned in section 2.3.3. Combined with the fact that this facet coincides with a near-basal plane, it is plausible that in this case a cleavage mechanism could have caused facet formation. However, it should be pointed out that the near-basal orientation of this facet does not exclude the possibility of basal $\langle 11\bar{2}0\rangle(0002)$ slip, which is for example observed in sample C1 (Figure 5-12b), although in that case the presence of the fan-shaped markings, which are totally different from the linear markings on the prismatic facets, cannot be explained. Therefore, these observations indicate the possibility that there could be two different facet formation mechanisms, one based on slip band formation and one based on cleavage, which would explain the disagreement in literature. Because an anomalous facet was only observed in sample D, and not in samples C1, C2 and C3, it is plausible that the grain size is one of the parameters that controls which mechanism occurs.

It is also important to consider that cleavage can only be expected to take place if there is a high normal stress on the cleavage plane. The relatively steep angle of the anomalous facet plane, which is approximately 62 degrees to the normal direction, seems to contradict this condition. However, as has been discussed in section 5.2, the stress distribution is not uniform at the microscale, and the local stress field will be affected by the orientation of neighbouring grains. Additionally, according to the cleavage model proposed by Neal and Blenkinsop[21], a normal stress can be induced on the cleavage plane by a dislocation pile-up on a prismatic slip plane in the same grain (see also section 2.3.3 and Figure 2-17). In support of this model, an EBSD measurement on one section through the anomalous facet revealed a region with a colour gradient in the orientation map (see Figure 5-13). Although this observation is only qualitative and two dimensional, it does point to the presence of a local lattice misorientation, which means that strongly localised deformation took place in this region. As mentioned in section 2.3.4, if the α grain size is larger, the effective slip length is longer and higher stresses can develop,[22, 23] which could explain why a possible cleavage mechanism was only observed in sample D.

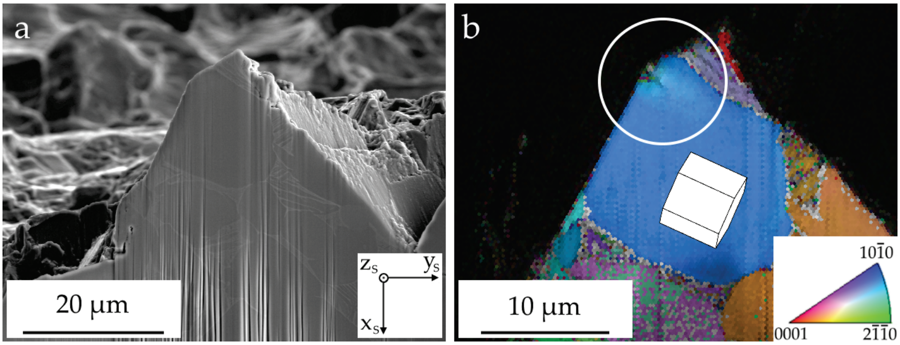

Figure 5-13: a) Front view SEM image of a cross-section through the anomalous facet of sample D; b) Colour coded orientation map for the α phase obtained by EBSD on the cross-section (reference direction z_s), showing a local lattice misorientation

As already mentioned above, the "regular" facets, which coincide with prismatic lattice planes, are most likely the result of prismatic slip band formation. Therefore, it is interesting to compare their characteristics with the slip-based facet formation mechanisms that have been suggested in literature. In the model proposed by Evans and Bache[10, 11] (see section 2.3.3), a "source" slip band in a weak grain induces a "failure" slip band on the basal plane of a strong grain, which then forms a facet that is at zero degrees to the normal direction. On the other hand, it has been mentioned in section 5.3.1 that in the current work there are no facets at zero degrees to the normal direction. An important difference to consider is the crystallographic texture of drawn wires, because there are virtually no "strong grains", which are oriented with their c-axis parallel to the wire axis (see section 3.1.2). In other words, there are no grains with their basal plane at zero degrees to the normal direction. However, there are many grains with a prismatic plane at approximately zero degrees to the normal direction (planes 1 and 4 in Figure 5-6b), and there does not appear to be facet formation on these planes either. Slip will occur most easily on slip systems for which the Schmid factor is high (see section 2.1.2 and equation 2.2), which in this case are planes 2, 3, 5 and 6 in Figure 5-6b. The Schmid factor for these planes would be approximately 0.43. On the other hand, the Schmid factor is zero for planes 1 and 4. It is logical to assume that if slip band formation precedes facet formation, facets will be formed on slip systems with a high Schmid factor. This explanation is in agreement with the results that are obtained in this work. The model proposed by Evans and Bache[10, 11] is clearly not applicable for the current work, seeing as no facets are formed on the prismatic planes that are also at zero degrees (planes 1 and 4 in Figure 5-6b). The conditions for facet formation as suggested by other authors,[9, 12] which are a moderate Schmid factor and a high tensile stress on the plane, are also not correct in this case.

Therefore, it seems that the different crystallographic texture of drawn wires has led to a different facet formation behaviour compared to the current description in literature. The difference lies in the presence of strong α grains in the forged or rolled materials investigated in literature, which are oriented with their c-axis parallel to the loading axis. The disagreement with the results of Evans and Bache[10, 11] is illustrated in Figure 5-14. In case of the presence of strong grains (Figure 5-14a), their model describes that a “source” slip band can develop in a weak grain (grain 1), which induces a high stress in a neighbouring strong grain (grain 2), because the latter is both elastically and plastically difficult to deform along the loading direction (see section 2.1.2). The induced shear stress leads to the formation of a basal slip band in the strong grain, which will develop further into a crack because it is also subjected to a high tensile stress.[10, 11]

In the current work, there is an absence of strong grains, and two simplified cases of neighbouring grain orientations can be considered (Figure 5-14b and c). In both cases, there is slip band formation in grain 1 in a prismatic slip system with a high Schmid factor, which leads to crack nucleation, as has been observed experimentally. If the orientation of grain 2 is very similar to the orientation of grain 1 (Figure 5-14b), it is possible that the crack can grow through the grain boundary. The case of a facet extending through two grains has for example been shown in Figure 5-12a (grains 3 and 4). The necessary conditions for short crack growth through grain boundaries will be discussed in more detail in section 6.2. In the second case (Figure 5-14c), the orientation of grain 2 is not similar to the orientation of grain 1, and crack transfer is unlikely. However, in contrast with the situation presented in Figure 5-14a, grain 2 is not a strong grain, which means that it can deform relatively easily. Therefore, it is unlikely that the stress, which is induced by the slip band in grain 1, would become high enough for slip to occur in grain 2 on a prismatic plane that is at zero degrees to the normal direction. In this case, it is therefore likely that the crack in grain 1 would be arrested at the grain boundary, although the induced plastic deformation in grain 2 could lead to other damage mechanisms such as void nucleation (as for example observed in Figure 5-12). Eventually, this damage might also lead to fracture of grain 2, but not in the form of a facet (i.e. not crystallographic).

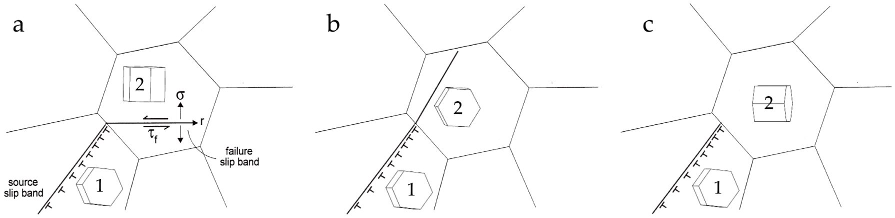

Figure 5-14: a) Evans and Bache model, in case of the presence of a strong grain;[10] b) Possible case in the absence of strong grains, with facet formation in grain 1 and crack growth through the grain boundary into grain 2; c) Possible case in the absence of strong grains, with facet formation in grain 1

It can then be questioned why, in the model proposed by Evans and Bache,[10, 11] the "source" slip bands do not lead to the formation of facets (see Figure 5-14a). Their explanation for this observation is that a high tensile stress is required for facet formation. However, the results obtained in this work show that this is not a necessary condition, since all of the facet planes are at relatively steep angles. A possible explanation for this disagreement is that facet formation simply occurs more rapidly on the failure slip band in the strong grain than it does on the source slip band in the weak grain. This could be due to the fact that the tensile stress is higher on the plane with the failure slip band. It is also possible that basal slip bands would for some reason be more prone to crack initiation than prismatic slip bands. This could for example explain why Bridier et al.[12] found that samples with basal facets had a lower fatigue life than samples with prismatic facets, although they only investigated samples with surface crack initiation (see section 2.3.3). In any case, in the current work there are no strong grains and therefore there is no distinction between source and failure slip bands, which means that slip bands will simply form in slip systems with a high Schmid factor and ultimately develop into facets.

Finally, it is not only important to understand how facets are formed, but also why they are formed in certain grains. In literature, the presence of strong grains or textural macrozones (see section 2.3.4) provides a relatively straightforward answer to this question. However, in the drawn wires that have been investigated in this work there are virtually no strong grains and no macrozones, and the observed facets do not seem to occur in grains with specific properties or orientations. To understand why facets are formed in certain grains in this case, the orientation of neighbouring grains should also be considered, which will be done in the next chapter (section 6.1).

5.5 Conclusions

In order to understand how the α facets, which are found at internal crack initiation sites, are formed, they have been analysed in detail in terms of their appearance, their spatial orientation and their crystallographic orientation. The facets are not smooth, but have some nano-roughness with linear markings for nearly all facets. One anomalous facet, on the fracture surface of the sample with the largest grain size (sample D), has a different appearance, with fan-shaped markings. Additionally, wear markings are observed in some cases, which are most probably the result of crack face sliding during crack closure. This friction wear due to crack closure can be attributed to the fact that the facets are at relatively steep angles, which in turn is caused by the crystallographic texture of the drawn wires. The facet plane angle distributions are very similar for the investigated samples, with most facet planes forming angles between 50 and 70 degrees with respect to the normal direction. From electron backscatter diffraction measurements on cross-sections of the fracture surfaces, it is found that nearly all of the examined facets are parallel to a prismatic plane of the hexagonal lattice. Additionally, the linear markings coincide with the slip direction of the prismatic slip system. Only the anomalous facet has a near-basal orientation. These observations suggest that it is possible that facets are formed by either a slip-based mechanism or a cleavage-based mechanism, and that the alpha grain size is one of the parameters that controls which mechanism occurs.

The cross-sections also expose secondary cracks, which have formed on prismatic planes as well, and in some cases early stage facet formation and short crack growth phenomena. The latter observations show that facets can extend through more than one grain, and that there is crack coalescence between facets. The crystallographic texture of drawn wires is different compared to forged or rolled material forms, because there are virtually no strong grains, which are oriented with their c-axis parallel to the loading axis. This difference leads to a different facet formation behaviour compared to what has been reported in literature, which is why the suggested facet formation mechanisms do not seem to be appropriate. With the exception of the anomalous facet, facet formation generally occurs on planes in slip systems that have a high Schmid factor. Additionally, the orientation of neighbouring grains has to be considered, because this will affect the local stress distribution, and could perhaps explain why facets form in specific grains. The effect of this local texture will be investigated in the next chapter.

5.6 References

[1] M. Hamada and O. Umezawa (2009). *Evaluation of Subsurface Fatigue Crack Life in Forged Ti-6Al-4V Alloys at Cryogenic Temperatures.* Isij International, 49(1), p. 124-131.

[2] S.G. Ivanova, R.R. Biederman, and R.D. Sisson (2002). *Investigation of fatigue crack initiation in Ti-6Al-4V during tensile-tensile fatigue.* Journal of Materials Engineering and Performance, 11(2), p. 226-231.

[3] M. Janeček et al. (2015). *The very high cycle fatigue behaviour of Ti-6Al-4V.* Acta Physica Polonica A, 128, p. 497-502.

[4] O. Umezawa and K. Nagai (1997). *Subsurface crack generation in high-cycle fatigue for high strength alloys.* ISIJ International, 37(12), p. 1170-1179.

[5] K. Tokaji, K. Ohya, and H. Kariya (2000). *Subsurface fatigue crack initiation in beta titanium alloys.* Fatigue & Fracture of Engineering Materials & Structures, 23(9), p. 759-766.

[6] A.J. McEvily, T. Nakamura, H. Oguma, K. Yamashita, H. Matsunaga, and M. Endo (2008). *On the mechanism of very high cycle fatigue in Ti-6Al-4V.* Scripta Materialia, 59(11), p. 1207-1209.

[7] H. Oguma and T. Nakamura (2013). *Fatigue crack propagation properties of Ti-6Al-4V in vacuum environments.* International Journal of Fatigue, 50, p. 89-93.

[8] S.K. Jha, C.J. Szczepanski, P.J. Golden, W.J. Porter, and R. John (2012). *Characterization of fatigue crack-initiation facets in relation to lifetime variability in Ti-6Al-4V.* International Journal of Fatigue, 42, p. 248-257.

[9] I. Bantounas, D. Dye, and T.C. Lindley (2009). *The effect of grain orientation on fracture morphology during high-cycle fatigue of Ti-6Al-4V.* Acta Materialia, 57(12), p. 3584-3595.

[10] M.R. Bache (1999). *Processing titanium alloys for optimum fatigue performance.* International Journal of Fatigue, 21, p. S105-S111.

[11] W.J. Evans (2004). *Time dependent effects in fatigue of titanium and nickel alloys.* Fatigue & Fracture of Engineering Materials & Structures, 27(7), p. 543-557.

[12] F. Bridier, P. Villechaise, and J. Mendez (2008). *Slip and fatigue crack formation processes in an alpha/beta titanium alloy in relation to crystallographic texture on different scales.* Acta Materialia, 56(15), p. 3951-3962.

[13] F.P.E. Dunne and D. Rugg (2008). *On the mechanisms of fatigue facet nucleation in titanium alloys.* Fatigue & Fracture of Engineering Materials & Structures, 31(11), p. 949-958.

[14] F.P.E. Dunne, A. Walker, and D. Rugg (2007). *A systematic study of hcp crystal orientation and morphology effects in polycrystal deformation and fatigue.* Proceedings of the Royal Society a-Mathematical Physical and Engineering Sciences, 463(2082), p. 1467-1489.

[15] S. Kibey, H. Sehitoglu, and D.A. Pecknold (2004). *Modeling of fatigue crack closure in inclined and deflected cracks.* International Journal of Fracture, 129(3), p. 279-308.

[16] M.R. Parry, S. Syngellakis, and I. Sinclair (2000). *Investigation of roughness induced crack closure effects in fatigue*, in *Damage and Fracture Mechanics VI*, A.P.S. Selvadurai and C.A. Brebbia, Editors. Witpress: Southampton, Boston.

[17] T.P. Chapman et al. (2015). *Characterisation of short fatigue cracks in titanium alloy IMI 834 using X-ray microtomography.* Acta Materialia, 99, p. 49-62.

[18] S. Suresh and R.O. Ritchie (1982). *A geometric model for fatigue crack closure induced by fracture surface roughness.* Metallurgical Transactions A, 13(9), p. 1627-1631.

[19] X. Liu, C. Sun, and Y. Hong (2016). *Faceted crack initiation characteristics for high-cycle and very-high-cycle fatigue of a titanium alloy under different stress ratios.* International Journal of Fatigue.

[20] R.J.H. Wanhill (1973). *Consideration of cleavage in alpha titanium.* Acta Metallurgica, 21(9), p. 1253-1258.

[21] D.F. Neal and P.A. Blenkinsop (1976). *Internal fatigue origins in alpha-beta titanium-alloys.* Acta Metallurgica, 24(1), p. 59-63.

[22] N.E. Paton, J.C. Williams, J.C. Chesnutt, and A.W. Thompson (1975). *The effects of microstructure on the fatigue and fracture of commercial titanium alloys.* AGARD Conference Proceedings, 185, p. 4-1 - 4-14.

[23] J.H. Zuo, Z.G. Wang, and E.H. Han (2008). *Effect of microstructure on ultra-high cycle fatigue behavior of Ti-6Al-4V.* Materials Science and Engineering A, 473(1-2), p. 147-152.

6 Influence of local texture on facet formation

The crystallographic texture has a large impact on the crack initiation behaviour of Ti-6Al-4V, because facet formation is known to occur on specific crystallographic planes. In the previous chapter, the facet formation mechanisms have been investigated and they have been shown to be affected by the texture. However, in the case of drawn wires, understanding how facets are formed does not seem to provide any insight into why facets form in specific grains. In other words, it is not yet clear which grains are susceptible to facet formation. Additionally, in some cases facets seem to have grown through the grain boundary into a neighbouring grain, which means that a distinction should be made between initiation and growth facets. Therefore, it is also important to understand under which conditions a facet is able to grow into a neighbouring grain.

In order to find an explanation for both problems, the orientation of neighbouring grains has to be investigated. In the case of crack initiation, this local texture will influence the local stress distribution, which could be an important factor in determining which grains form facets. In the case of short crack growth, the orientation of neighbouring grains determines whether there is an easy crack path, because facets are known to grow on certain crystallographic planes. This chapter first describes the approach to the crack initiation problem and the results of a Schmid and Taylor factor analysis of faceted and neighbouring grains. The next section discusses measurements of tilt and twist angles, which determine how easily a crack can grow into a neighbouring grain, and also presents an alternative approach by calculating alignment factors.

6.1 Crack initiation

In order to find out why facets are formed in specific grains, the orientation of faceted grains should be compared with the orientation of grains that did not develop facets, and with the orientation of grains that are direct neighbours to the faceted grains. The first comparison will indicate whether facets initiate in grains that in some way deviate from the average grain behaviour. The second comparison, on the other hand, only considers the local texture, which means that it could indicate whether a combination of local grain orientations can be related to the occurrence of facet formation. In order to quantitatively analyse and compare grain orientations, it is necessary to calculate specific properties that are dependent on these orientations. In the following sections, two of these properties are examined: the Schmid factor and the Taylor factor.

These two factors are calculated from EBSD measurements on cross-sections of fracture surfaces that have been made by FIB milling (see section 5.3.2). The Schmid and Taylor factors of every sectioned facet can be compared with the average values. Additionally, the Schmid and Taylor factors of neighbouring grains can be calculated and compared with those of the faceted grain. Figure 6-1 illustrates the identification of neighbouring grains around a faceted grain for a cross-section of the fracture surface of sample D (see sample nomenclature in section 4.2). It should be made clear that only primary α grains are considered in this case, because the resolution is generally not sufficient to confidently determine the orientation of secondary α rods. This figure also shows that not all of the neighbouring grains are measured, because the opposing fracture surface is not considered. However, even if the opposing fracture surface would be measured, by sectioning at the exact matching location, not all neighbouring grains would be visible because the cross-sections only provide two-dimensional information. This means that for every individual section, the direct neighbour analysis is not comprehensive, or, in other words, that some neighbouring grains will not be included. Therefore, instead of considering each cross-section separately, the information that is gathered from every cross-section will be combined in order to obtain an overview of the differences in Schmid or Taylor factor between facets and their analysed neighbouring grains.

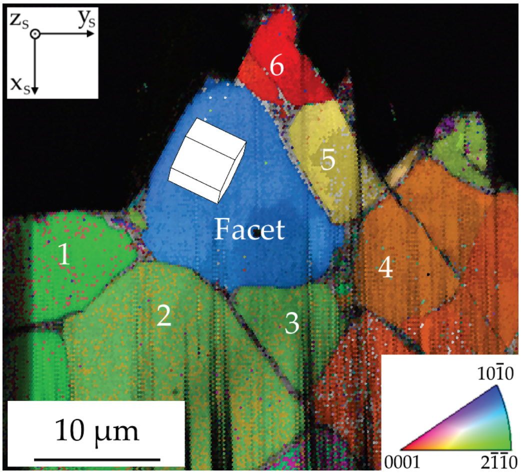

Figure 6-1: Colour coded orientation map obtained by EBSD on a cross-section through the fracture surface of sample D (reference direction z_S), illustrating the identification of six neighbouring grains around a faceted grain; Note that x_S is the wire axis (see definition of sample coordinate system in Figure 5-7)

6.1.1 Schmid factor analysis

It has been shown in the previous chapter that nearly all facet planes coincide with a prismatic lattice plane, and that the linear markings on facet surfaces are parallel to the prismatic slip direction. Because this is a strong indication that prismatic slip and slip band formation precedes facet formation, it is logical to first examine whether the faceted grains are oriented for easier prismatic slip compared to other grains. As has been discussed in section 2.1.1, the influence of the grain orientation on the resolved shear stress for specific slip systems can be expressed by Schmid's law.[1] The Schmid factor (equation 2.2) for prismatic slip provides information on how easily prismatic slip can occur for a certain grain orientation. A grain with a high prismatic Schmid factor experiences a high resolved shear stress in one of its prismatic slip systems during loading. There are three prismatic slip systems that have to be considered for each grain: $(10\bar{1}0)[\bar{1}2\bar{1}0], (1\bar{1}00)[\bar{1}\bar{1}20]$ and $(01\bar{1}0)[2\bar{1}\bar{1}0]$.[2] The Schmid factor for these three systems is determined in every measured grain, in the case of uniaxial loading along the wire axis, and only the highest value is retained.

An analysis of Schmid factors for prismatic slip is performed for samples C3 and D (see sample nomenclature in section 4.2). The average values are presented in Figure 6-2 and Figure 6-3. The total average includes faceted grains, neighbouring grains and other grains, which are neither a faceted nor a neighbouring grain. For sample C3, the total average, facet average and neighbour average are calculated using 150, 19 and 74 grains, respectively. For sample D, the total average, facet average and neighbour average are calculated using 129, 17 and 63 grains, respectively. Figure 6-2 shows that for sample C3 there do not seem to be any differences between the average Schmid factor of the faceted grains, the average Schmid factor of the neighbouring grains and the total average. As has been discussed in chapter 5, sample D contains one anomalous facet which does not coincide with a prismatic plane. Therefore, the prismatic Schmid factor for this facet is shown separately in Figure 6-3. This figure also shows that, for sample D, the average Schmid factor of regular faceted grains appears to be slightly higher compared to the total average and to the average of neighbouring grains, although it remains well within the standard deviation ranges of both data sets.

The grain that formed the anomalous facet has a lower Schmid factor for prismatic slip (0.39), which is consistent with the fact that it did not fracture on a prismatic plane. It has been mentioned in section 5.4 that there are indications that a cleavage mechanism could have led to the formation of this anomalous facet. However, it was also pointed out that the possibility of basal slip could not be excluded, because the anomalous facet has a near-basal orientation. Therefore, it makes sense to check the Schmid factor for basal instead of prismatic slip in this case. The total average of the Schmid factor for basal slip in sample D is 0.09 with a standard deviation of 0.12, whereas the anomalous facet has a basal Schmid factor of 0.39. This means that the grain in which the anomalous facet was formed, was oriented for easier basal slip compared to the average. This will be discussed further in section 6.1.3.

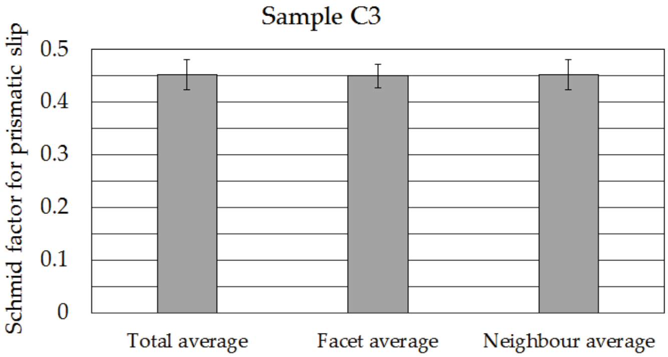

Figure 6-2: Average Schmid factors for prismatic slip for sample C3 (error bars represent standard deviation)

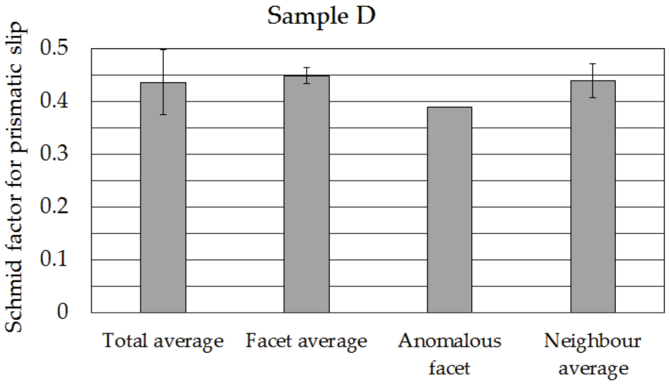

Figure 6-3: Average Schmid factors for prismatic slip for sample D (error bars represent standard deviation)

However, averaging the Schmid factors of all faceted grains and all neighbouring grains does not give any insights into the local differences, which means the Schmid factor of one faceted grain compared to the Schmid factors of its corresponding neighbouring grains. These local differences can be analysed for every sectioned facet. The results of this analysis are presented in Figure 6-4 and Figure 6-5 for samples C3 and D, respectively. Every point in these plots represents a neighbouring grain. The horizontal axis provides the value of the prismatic Schmid factor of the faceted grain that it is next to. The vertical axis provides the value of the prismatic Schmid factor of the neighbouring grain minus the value of the prismatic Schmid factor of the faceted grain. If the faceted grains would have Schmid factors that are generally higher than their respective neighbouring grains, there should be a tendency towards negative differences (on the vertical axis). This is not the case, for both sample C3 and sample D. In fact, the average difference in prismatic Schmid factor between neighbouring grains and their corresponding faceted grain is 0.002 for sample C3 and -0.008 for sample D, not taking into account the anomalous facet. In other words, the faceted grains do not appear to be different from their neighbouring grains, in terms of the Schmid factor for prismatic slip. Figure 6-5 shows that there is a difference for the anomalous facet and its neighbouring grains, which is logical because the prismatic Schmid factor of the anomalous facet is relatively low compared to the average (see Figure 6-3).

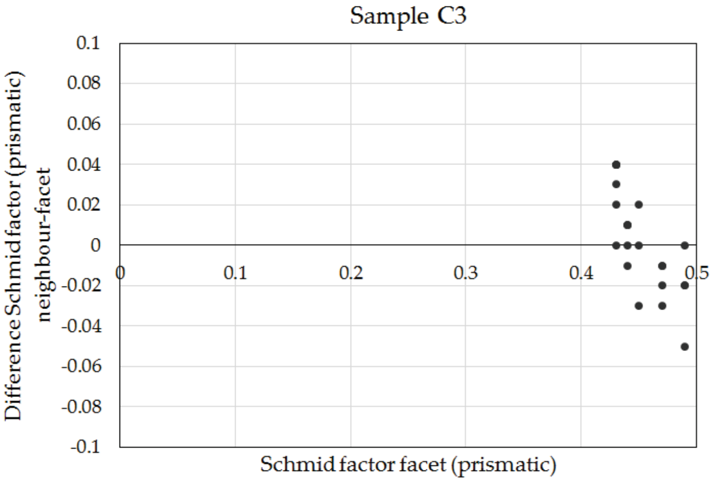

Figure 6-4: Plot of the difference in prismatic Schmid factor between neighbouring grains and the corresponding faceted grain, as a function of the prismatic Schmid factor of the faceted grain (sample C3)

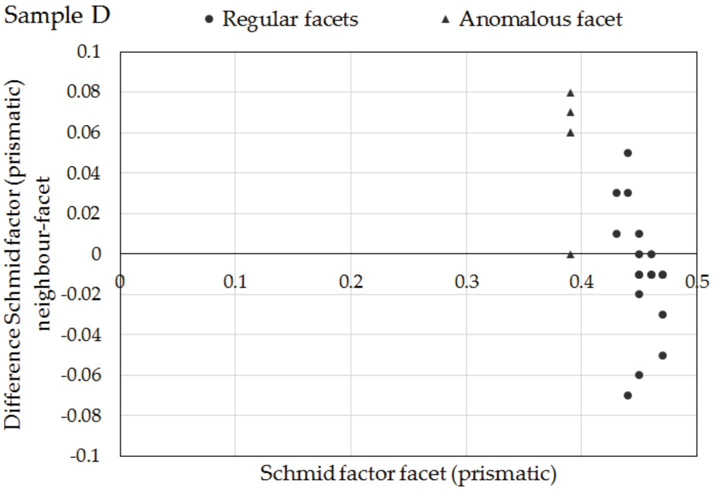

Figure 6-5: Plot of the difference in prismatic Schmid factor between neighbouring grains and the corresponding faceted grain, as a function of the prismatic Schmid factor of the faceted grain (sample D); Dots represent data of regular facets, triangles represent data of the anomalous facet

The analysis of Schmid factors for prismatic slip does not provide a satisfactory explanation for the occurrence of facet formation in specific grains. One possible reason for this shortcoming, is that Schmid's law approaches crystal plasticity from a stress point of view. In other words, in this analysis it is implicitly assumed that every grain experiences the same, externally applied stress (σ in equation 2.1). However, it has already been mentioned that, because of the high anisotropy of the hexagonal α phase, the local texture is expected to lead to significant differences in local stresses (see, for example, section 2.3.3). Because it is likely that this stress distribution plays a role in the occurrence of facet formation, it is not surprising that the Schmid factor is not an adequate parameter in this case.

6.1.2 Taylor factor analysis

A different method that could explain why certain grains are susceptible to facet formation, is to do a comparison of the Taylor factors instead of the Schmid factors. Taylor[3] noted that there should be strain compatibility requirements between grains during plastic deformation, which means that the problem can be approached from a strain point of view instead of a stress point of view. The key assumption in the Taylor model is that there is uniform strain within each grain, which is equal to the macroscopic strain. In every grain, a set of five slip systems has to be activated in order to accommodate this strain. This set of slip systems is dependent on the crystallographic orientation of the grain, and is determined by stating that the plastic work should be minimal. This way, the Taylor factor can be calculated for any given applied deformation gradient and crystal orientation. For each grain, the Taylor factor gives an indication of the amount of plastic work that is required to accommodate the applied deformation. In other words, a grain with a high Taylor factor will behave as a hard grain, which is difficult to deform plastically. For a grain with a low Taylor factor, a more efficient set of slip systems is available and plastic deformation requires less work.[3, 4]

In order to calculate Taylor factors from the EBSD measurements on cross-sections of fracture surfaces, some input is required regarding the imposed plastic strain increment **dε** and the available slip systems, with their respective critical resolved shear stresses (CRSS). During plastic deformation the volume must stay constant,[4] so the plastic strain increment for uniaxial tension along x_S, which is the wire axis, is:

$$\boldsymbol{d\varepsilon} = \begin{bmatrix} d\varepsilon_{x_S x_S} & d\varepsilon_{x_S y_S} & d\varepsilon_{x_S z_S} \\ d\varepsilon_{y_S x_S} & d\varepsilon_{y_S y_S} & d\varepsilon_{y_S z_S} \\ d\varepsilon_{z_S x_S} & d\varepsilon_{z_S y_S} & d\varepsilon_{z_S z_S} \end{bmatrix} = \begin{bmatrix} 1 & 0 & 0 \\ 0 & -0.5 & 0 \\ 0 & 0 & -0.5 \end{bmatrix} d\varepsilon$$

All basal, prismatic and pyramidal slip systems are considered, and the CRSS values that are used for calculating the Taylor factors are shown in Table 2-2. Generally, the calculation of Taylor factors involves the assumption that the CRSS values are the same for each slip system. However, because in this case the CRSS values are not the same for each family of slip systems, it is necessary to define what is considered as the Taylor factor in this work. If τ_i represents the CRSS value and $d\gamma_i$ the slip rate in the i-th slip system, the internal plastic work rate dw can be expressed as:[5]

$$dw = \sum_i \tau_i |d\gamma_i| \qquad (i = 1,2,\dots,5)$$

In Taylor's theory,[3] the selection of five slip systems, which have to satisfy the applied strain increment, is based on the minimisation of dw. The definition of the Taylor factor that is used in this work (for uniaxial tension along x_S), is:

$$\frac{\sum_i \tau_i |d\gamma_i|}{\tau_{prism} d\varepsilon_{x_S x_S}} \qquad (i = 1,2,\dots,5)$$

Note that τ_{prism}, which is the CRSS value for prismatic slip systems, can be interpreted as a normalising factor. This means that in this equation the CRSS value τ_i of each system i is expressed relative to τ_{prism}. This definition of the Taylor factor represents a relative plastic work rate, which gives an indication of the relative amount of plastic work that is required in a specific grain to accommodate the applied deformation. It should be noted that the Taylor factors are calculated with TSL OIM Analysis 7 software, which uses an algorithm based on the Bishop-Hill theory.[6] In this algorithm, the plastic strain increment is first transformed into crystal coordinates for each grain. Then, the possible values of the external plastic work rate are calculated by multiplying with each possible stress state that satisfies the yield locus of the crystal, which is dependent on the available slip systems and the CRSS values. The operative stress state is the one that results in the maximum external plastic work rate, which is then used to calculate the Taylor factor. The method of Bishop and Hill[6] (principle of maximum external plastic work) is strictly equivalent to the method of Taylor[3] (principle of minimum internal plastic work).[7]

Following the same methodology as in the previous section, a first comparison is made between the average values of the Taylor factor for faceted grains, for neighbouring grains, and for all measured grains. These average values are shown in Figure 6-6 and Figure 6-7 for samples C3 and D, respectively. For both samples, the average Taylor factor of faceted grains appears to be slightly higher compared to the average Taylor factor of neighbouring grains, and compared to the total average. However, the differences remain well within the standard deviation ranges. Figure 6-7 shows that the anomalous facet in sample D has a lower Taylor factor, which would mean that this grain was oriented for relatively easy deformation. This will be discussed further in section 6.1.3.

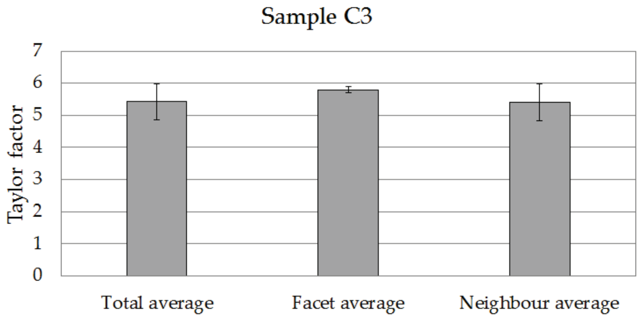

Figure 6-6: Average Taylor factors for sample C3 (error bars represent standard deviation)

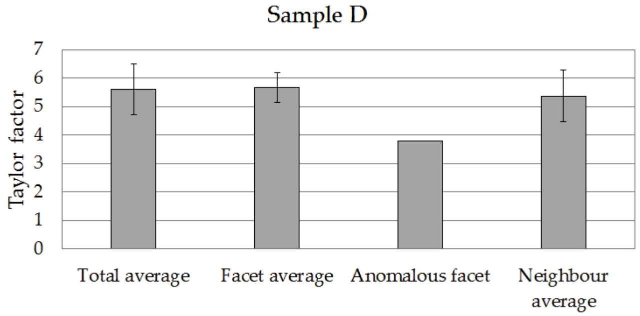

Figure 6-7: Average Taylor factors for sample D (error bars represent standard deviation)

As mentioned in the previous section regarding Schmid factors, comparing the average Taylor factor of all faceted grains with the average Taylor factor of all neighbouring grains does not provide any insights into the local differences between each faceted grain and its corresponding neighbouring grains. Therefore, these differences are plotted in Figure 6-8 and Figure 6-9 for samples C3 and D, respectively. Again, similar to the analysis in the previous section, every point in these plots represents a neighbouring grain. The horizontal axis provides the value of the Taylor factor of the faceted grain that it is next to. The vertical axis provides the value of the Taylor factor of the neighbouring grain minus the value of the Taylor factor of the faceted grain. For both samples there is a tendency towards negative differences (on the vertical axis), which means that the faceted grains generally seem to have a higher Taylor factor compared to their corresponding neighbouring grains. The average difference in Taylor factor between neighbouring grains and their corresponding faceted grain is -0.3 for sample C3 and -0.41 for sample D, not taking into account the anomalous facet. This means that the faceted grains can be considered as hard grains, which do not deform easily, in comparison with their neighbouring grains. The implications of this observation regarding crack initiation will be discussed in the following section (6.1.3). Finally, Figure 6-9 shows that for the anomalous facet, the differences are generally positive values, which means that it has a lower Taylor factor compared to its neighbouring grains, and it behaves as a relatively soft and easily deformable grain. The consequence of this observation on the possibility of a cleavage mechanism will also be discussed in section 6.1.3.

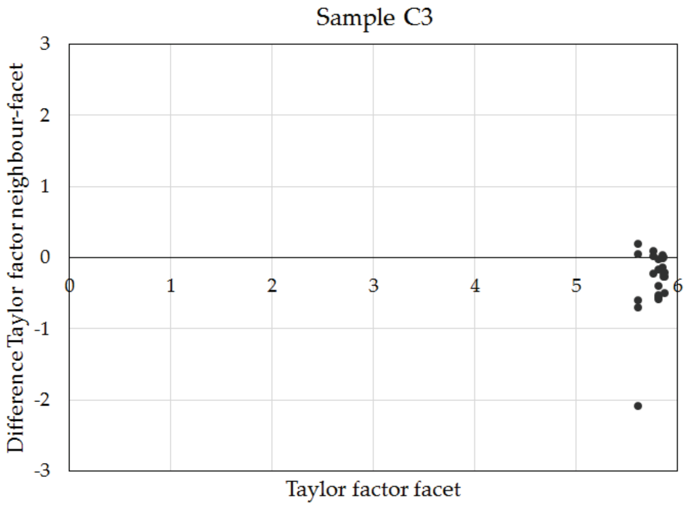

Figure 6-8: Plot of the difference in Taylor factor between neighbouring grains and the corresponding faceted grain, as a function of the Taylor factor of the faceted grain (sample C3)

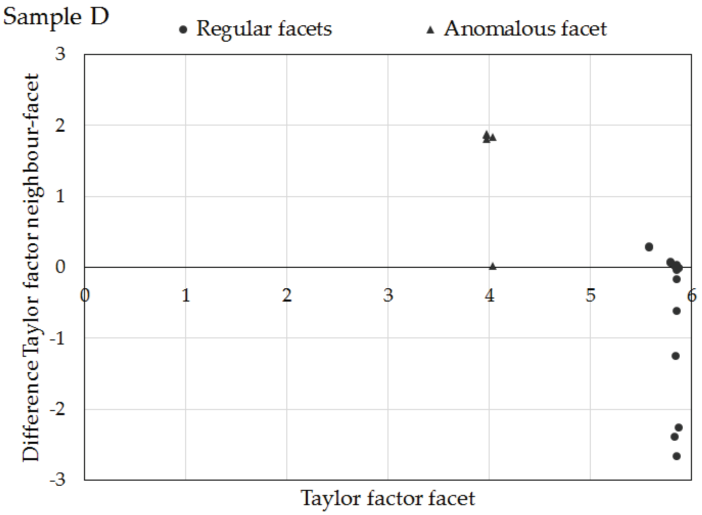

Figure 6-9: Plot of the difference in Taylor factor between neighbouring grains and the corresponding faceted grain, as a function of the Taylor factor of the faceted grain (sample D); Dots represent data of regular facets, triangles represent data of the anomalous facet

6.1.3 Discussion on susceptibility to facet formation

The results above show that the Schmid factor for prismatic slip does not seem to be a suitable parameter to explain which grains are susceptible to facet formation. However, the Taylor factor of faceted grains is generally higher compared to their respective neighbouring grains. On the other hand, it has been shown in chapter 5 that, apart from the anomalous facet, all facets are most likely formed by a prismatic slip-related process. Therefore it is logical to question how the Taylor factor could be an appropriate parameter to predict crack initiation. The first step towards a possible explanation has already been discussed at the end of section 6.1.1. It is clear that the anisotropy of the α phase gives rise to a stress redistribution at the microscale, which is dependent on the local texture. The Schmid factor cannot represent this, because its calculation implies the assumption that the stress is the same for each grain. On the other hand, the Taylor factor does appear to represent this behaviour, because it describes how difficult it is for grains to deform plastically, assuming that the strain is the same for each grain. In other words, it quantifies the meaning of "hard" (or strong) and "soft" (or weak) grains, which play an important role in the occurrence of facet formation,[8, 9] as has already been discussed in section 2.3.3. In this case, faceted grains could be considered as being somewhat "harder" compared to their direct neighbouring grains, because the higher Taylor factor implies that they are more difficult to deform plastically. However, facets form in these grains as a result of planar prismatic slip, which cannot be explained with the Taylor model. Therefore, it is necessary to make a clear distinction regarding the interpretation of this analysis. The Taylor factors, in this case, are only interpreted as a way to understand possible stress redistribution between neighbouring grains, and should not be used to explain the plasticity behaviour itself. This is rather logical because the current problem involves cyclic loading instead of monotonic loading. In other words, the Taylor factor might be useful to explain why facets are formed in certain grains, but not how they are formed.

Although, to the author's knowledge, this Taylor factor approach has not yet been proposed in literature, it seems to be a convenient way to describe what several authors have already attempted to explain in a more elaborate way, which is that a certain combination of grain orientations may lead to facet formation. If a "hard" grain is surrounded by "soft" grains, it will experience a higher stress, which can cause facet formation. This stress redistribution can be easily understood by comparing it to the simple case of two springs being loaded in parallel. The strain is the same for both springs, but if one of the springs provides more resistance to deformation, it experiences a higher stress. Dunne et al.[8, 10] simulated the effect of various combinations of crystallographic orientations on grain-level stresses by using a crystal plasticity model, and they found a rogue grain combination, for which the normal stress on the basal plane of the hard grain is the highest. This worst case scenario occurs if the hard grain is oriented with its c-axis approximately parallel to the loading direction, and the neighbouring soft grain has its c-axis normal to the loading direction and a prismatic plane at approximately 70° to the loading direction. Evans and Bache[11, 12] used a similar case in their model for facet formation (see also Figure 5-14a). The Taylor factors for this combination, calculated by using the same input as described in section 6.1.2, would be 8.87 for the hard grain and 5.77 for the soft grain. This means that the difference in Taylor factor between the neighbouring grain and the facet-forming grain would be -3.1. This difference is indeed greater than the values obtained in this work (see Figure 6-8 and Figure 6-9). It has been discussed in chapter 5 that the crystallographic texture of drawn wires is different, because there are virtually no grains which are oriented with their c-axis parallel to the loading axis. As a result of this texture, the differences in Taylor factor between faceted and neighbouring grains are relatively small (on average -0.3 for sample C3 and -0.41 for sample D). However, the observations in these drawn wires show that even small orientation differences, and correspondingly small differences in Taylor factor, can lead to facet formation, even though it might take more time (see also section 5.4). Therefore, this work provides new information that should be included in the search for an optimal texture for fatigue performance, as has been discussed for example by Bache.[11] With this in mind, it appears that, for tension-tension loading, the texture of drawn wires already results in a better very high cycle fatigue performance compared to forged or rolled products, because of the absence of large orientation differences between grains.

The anomalous facet in sample D, which was categorised as anomalous because of its different surface markings and near-basal orientation (see chapter 5), also behaves irregularly in the Schmid and Taylor factor analysis. The orientation of this grain is represented in inverse pole figures in Figure 6-10a and b, which also show iso-curves of constant prismatic (a) and basal (b) Schmid factor. It can be seen that the regular faceted grains in this sample have an orientation for which the prismatic Schmid factor is high, and the basal Schmid factor is very low. However, for the anomalous facet, the prismatic and Basal Schmid factor are both approximately equal to 0.39. This also provides an explanation for the fact that the Taylor factor of this grain is relatively low (see Figure 6-7), since both prismatic and basal slip systems may be activated relatively easily, which means that the grain is “soft” in terms of plastic deformability. Although this observation suggests that this facet was indeed formed by a different mechanism, it is to some extent in contradiction with the possibility of a cleavage mechanism, because as mentioned in section 5.4, cleavage can only be expected to take place if there is a high normal stress on the cleavage plane. This seems unlikely if the stress in this grain can be easily relaxed by dislocation slip.

There are two possible explanations for the formation of this anomalous facet. The first possibility is that, indeed, this facet was not formed by a cleavage mechanism, but instead by basal slip band formation. The main problem with this explanation is the presence of the fan-shaped pattern on the facet surface (see Figure 5-2f), which deviates from the linear markings that are present for other facets. A second possible explanation is that this facet was formed by a cleavage mechanism, according to the model that has been suggested by Neal and Blenkinsop[9] (see also section 2.3.3 and Figure 2-17). Their model does not consider neighbouring grains and describes that the formation of dislocation pile-ups on slip planes can induce a high normal stress on the cleavage plane. In this case, the low Taylor factor and the availability of slip systems could mean that dislocation pile-ups were formed in this grain. At this point, it is not clear which explanation is correct. Additionally, only one anomalous facet has been found and analysed, and more data would have to be collected in order to provide a satisfactory explanation.

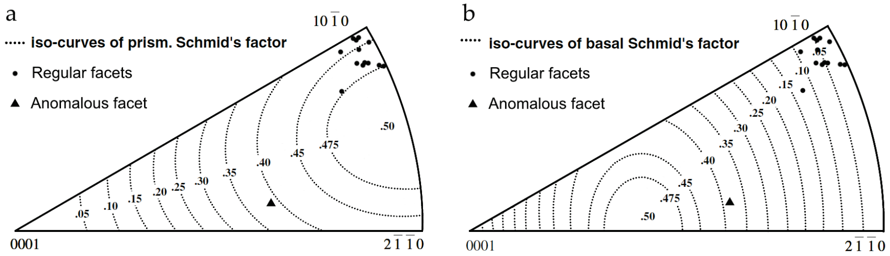

Figure 6-10: Inverse pole figures with iso-curves of the prismatic (a) and basal (b) Schmid factor,[13] with dots to represent the orientation of regular facets and a triangle to represent the orientation of the anomalous facet (for sample D); The reference direction in this case is the wire axis x_S (see sample coordinate system definition in Figure 5-7)

It has been mentioned in section 6.1 that the Schmid and Taylor factor analyses in this work do not take into account all neighbouring grains. Furthermore, the rogue grain combination that has been suggested by Dunne et al.[8, 10] only consists of two grains. Therefore, in both cases the question still remains whether it might be necessary to consider all neighbouring grains. Regarding the work of Dunne et al.,[8, 10] there could possibly be an even worse case scenario than this rogue grain combination if several neighbouring grains had been accounted for in the model. In the current work, the Taylor analysis shows that the average difference in Taylor factor between a neighbouring and a faceted grain is negative (-0.3 for sample C3 and -0.41 for sample D), but this does not mean that every neighbouring grain has a lower Taylor factor than the faceted grain. This is also illustrated by the plots in Figure 6-8 and Figure 6-9, which show that there are positive differences as well. Consequently, the exact conditions for determining potential facet formation locations in drawn wires are not yet entirely clear. This also remains an open question because not all neighbouring grains are accounted for. To answer this question experimentally, it would be necessary to do a rigorous texture analysis in 3D on a large number of fracture surfaces, which would be enormously time-consuming. Additionally, the role of secondary α, which is present in the dual-phase regions in between primary α grains, has not been investigated. As has been discussed in section 3.1.2, some of these secondary α grains have "hard" orientations, with the c-axis close to the wire axis. This is illustrated once more in the orientation map in Figure 6-11. Therefore, secondary α grains could also influence the stress distribution.

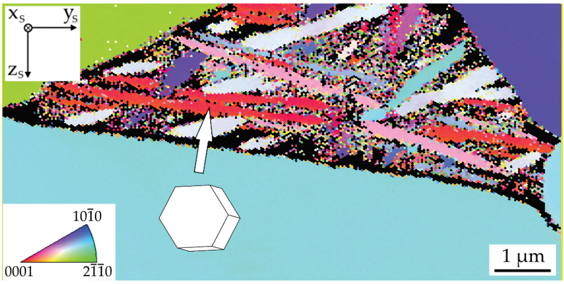

Figure 6-11: Colour coded orientation map obtained by EBSD on a cross-section of a wire with microstructure D, to illustrate the presence of secondary α with a "hard" orientation (the wire axis x_s is the reference direction)

Finally, it is important to mention that the Taylor factor approach in section 6.1.2 only considers plastic behaviour and does not include any elasticity effects. Because differences in elastic stiffness between grains can also affect the stress distribution, neglecting elasticity could be perceived as an oversimplification. However, the simplified approach in this work can be justified because of two reasons. Firstly, it is clear that, even though the macroscopic stress is within the elastic region, localised plasticity is occurring at the microscale. Therefore, it is more appropriate to consider the plastic behaviour, with a plasticity model (i.e. Taylor model), rather than considering the elastic behaviour. Evidently, a more complicated finite element model, which could take into account both elasticity and plasticity, would provide a more accurate representation of the actual stress distribution. For example, this type of modelling (in 2D) has already been performed by Dunne & Rugg,[8] although they did not use an experimentally obtained microstructure or texture as input for their model. Secondly, because of the crystallographic texture of the drawn wires that are investigated in this work, the differences in stiffness (in the direction of the wire axis) between grains are relatively small. This is illustrated in Figure 6-12, which shows the variation of the E modulus and Taylor factor of a single crystal as a function of the loading direction. Please note that for this plot the Taylor factor is calculated as described in section 6.1.2, and the E modulus is calculated with the elastic stiffness tensor components shown in Table 6-1. As mentioned in section 3.1.2, texture measurements on the wires have shown that there is a high tendency for grains to be oriented with the normal direction of the prismatic $\{10\bar{1}0\}$ planes parallel to the wire axis (see also Figure 3-3). In Figure 6-12, the angle that describes this orientation is 0 degrees, because the wire axis is the loading axis. It can be observed that at these low angles, the E modulus is nearly constant. In fact, the difference in E modulus between loading angles of 10° and 0° is approximately 0.5 GPa. For this reason, the small orientation differences between grains will only lead to very small differences in E modulus. On the other hand, the Taylor factor is more sensitive to small orientation differences in this region. Therefore, even though it is clear that the Taylor factor by itself cannot fully describe the stress distribution between grains, it is plausible that it could indeed provide an indication of this stress distribution.

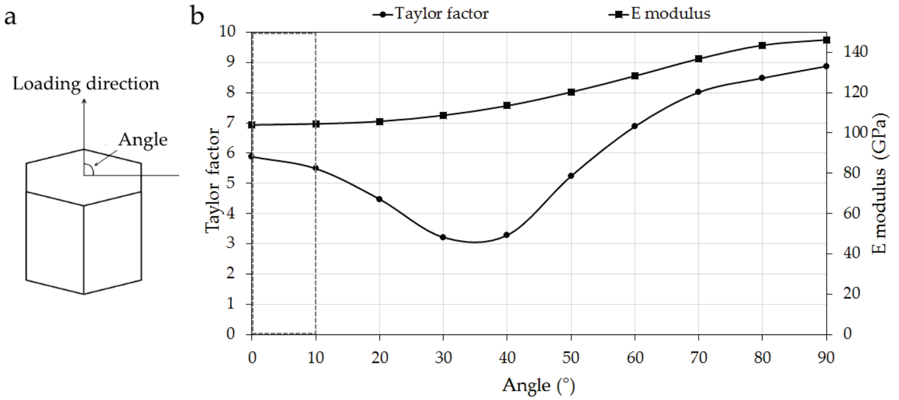

Figure 6-12: Taylor factor and E modulus variation as a function of the loading direction: a) Definition of (uniaxial) loading direction and varied angle; b) Taylor factor and E modulus as a function of the defined angle

Table 6-1: Single crystal elastic stiffness tensor components (GPa) for α-Ti, used for the calculation of E moduli[14]

C11	C33	C44	C12	C13
160	181	46.5	90	66

6.2 Short crack growth

In the previous chapter, it has been shown that in some cases facets seem to have grown through the grain boundary into a neighbouring grain. In order to explain the possible occurrence of short crack transfer through grain boundaries, the crystallographic orientations of the faceted grain and the neighbouring grain should be analysed. The compatibility of the crack planes in both grains can then be expressed by the tilt and twist angles, which have been defined in section 2.2.3 and illustrated in Figure 2-10. The following section first describes how these angles are determined from EBSD measurements on fracture surface cross-sections. In the next section, a few observed cases of apparent short crack growth are analysed. Finally, an alternative approach based on slip transfer criteria is described, in which the alignment factor A is used to understand short crack transfer by checking the compatibility of slip systems.

6.2.1 Determination of tilt and twist angles from Euler angles

As has been mentioned in section 2.2.3, the interaction of short cracks with grain boundaries in Ti-6Al-4V is dependent on the crack plane compatibility between the neighbouring grains. The model that has been proposed by Zhai et al.[15] expresses this compatibility with two angles: the tilt (ϑ) and the twist (ω) angle. The crack (or slip) planes can be described by unit vectors of the plane normal [N_1] and [N_2], which can be calculated from EBSD measurements. These two planes intersect the sample surface, described by normal unit vector [Z], which results in crack traces that are visible on the surface, or in this case on the FIB milled cross-section. The angle between those traces is defined as the tilt angle ϑ. The grain boundary can be described by a unit vector [E] that is normal to the grain boundary plane. The two crack (slip) planes intersect the grain boundary plane and the angle between those intersects is called the twist angle ω. The twist angle has been reported as being the most important controlling parameter for short crack growth through a grain boundary, followed by the tilt angle and also to lesser extent the Schmid factor of the slip system in the second grain. If the tilt and twist angles are small, crack transfer can occur easily.[15-18]

If vectors [N_1], [N_2], [E] and [Z] are known, both angles can be calculated from equations 2.8 and 2.9. The first two vectors, which describe a slip plane in grain 1 and a slip plane in grain 2, can be calculated from the EBSD measurements on FIB milled cross-sections of the fracture surface. For each grain, the EBSD measurement provides the Euler angles (ϕ_1, Φ, ϕ_2), according to Bunge's description.[19] These angles fully describe the crystallographic orientation of the grain, and are defined as the rotations that are needed to bring the sample coordinate system into coincidence with the crystal coordinate system. In the next step, a rotation matrix is constructed for each grain, based on its Euler angles, which can be used to rotate vectors from the crystal coordinate system to the sample coordinate system. This rotation matrix is defined as:[19]

$$\begin{bmatrix} \cos\varphi_1\cos\varphi_2-\sin\varphi_1\cos\Phi\sin\varphi_2 & -\cos\varphi_1\sin\varphi_2-\sin\varphi_1\cos\Phi\cos\varphi_2 & \sin\varphi_1\sin\Phi \\ \sin\varphi_1\cos\varphi_2+\cos\varphi_1\cos\Phi\sin\varphi_2 & -\sin\varphi_1\sin\varphi_2+\cos\varphi_1\cos\Phi\cos\varphi_2 & -\cos\varphi_1\sin\Phi \\ \sin\Phi\sin\varphi_2 & \sin\Phi\cos\varphi_2 & \cos\Phi \end{bmatrix}.$$

Only prismatic planes will be considered, since all the short crack transfer cases that are discussed in the following section concern possible crack transfer on prismatic planes. In order to avoid additional complexity because of the hexagonal lattice structure, a Cartesian (cubic) crystal coordinate system (x_C, y_C, z_C) is used, as shown in Figure 6-13a. For the three prismatic planes in the lattice, a unit vector normal to the plane is determined in this coordinate system. For each grain, these are then transformed to the sample coordinate system (x_S, y_S, z_S), which is defined in Figure 6-13b, by using the corresponding rotation matrix. This leads to three possible vectors for [N_1] (grain A) and three possible vectors for [N_2] (grain B). In other words, these vectors define the three prismatic planes of each grain in the sample coordinate system. The unit vector normal to the surface plane, [Z], is taken as the EBSD measurement plane (x_S-y_S plane), which means its coordinates are (0,0,1) in the sample coordinate system. In order to determine the grain boundary plane normal [E], the intersection of the grain boundary plane with the x_S-y_S plane is first obtained from the orientation (EBSD) map. The grain boundary plane normal [E] is then assumed to be perpendicular to z_S. The tilt and twist angles are calculated from equations 2.8 and 2.9 for all possible combinations of prismatic planes. There are three possibilities for [N_1] (grain 1) and three possibilities for [N_2] (grain 2), which means that there are nine possible combinations of prismatic planes and correspondingly nine possible tilt and twist angles values. If there has been crack transfer, the crack traces on the x_S-y_S plane can be used to approximately determine the value of the tilt angle. By comparing this value to the nine calculated values, the correct combination of slip planes can be selected.

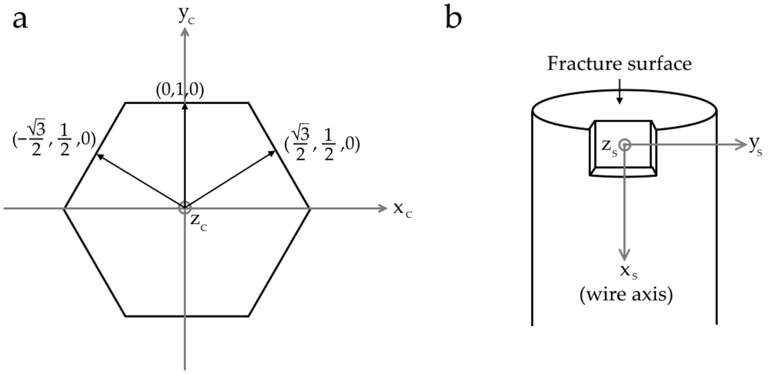

Figure 6-13: a) Definition of Cartesian crystal coordinate system, and unit vectors to describe the three prismatic planes; b) Definition of sample coordinate system for a sectioned fracture surface

6.2.2 Tilt and twist angle analysis

The SEM image and orientation map of the first examined cross-section with possible short crack transfer are shown in Figure 6-14. It can be seen that there appears to have been short crack transfer between grains 1 and 2. The tilt and twist angles in this case are approximately 2.4 and 16.7 degrees, respectively. On the other hand, the facet in grain 3 does not extend into grain 2. For these grains, the lowest tilt and twist angles are approximately 4.7 and 33.8 degrees, respectively. The tilt and twist angles could therefore explain why short crack transfer took place between grains 1 and 2, and did not take place between grains 2 and 3. In comparison, Zhai et al.[18] observed crack transfer in a high strength aluminium alloy for tilt and twist values of 24 degrees and 0.7 degrees, and crack arrest for tilt and twist values of 62° and 7.2 degrees. However, it should be noted that there is a difference between the experiments in this work and those performed by other authors who measured tilt and twist angles.[15-18, 20] In the latter case, the experiments involve one main crack, which follows a certain path through the microstructure. The deflections of this path at grain boundaries are dependent on the tilt and twist values, because these express the easiest crack path. In the current work, several short cracks are present in the bulk of the sample. This situation is more complicated, because it is not clear when each of these short cracks initiated. For example, in the case of Figure 6-14, it is possible that the crack in grain 1 nucleated first and propagated into grain 2, before the crack in grain 3 nucleated. This could also play a role in determining whether the crack in grain 3 would propagate into grain 2. This remark is a first indication that the tilt and twist model might not be entirely capable of explaining short crack transfer in the current work.

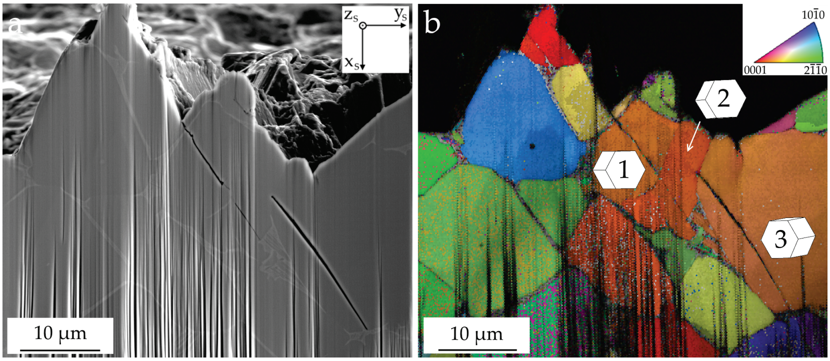

Figure 6-14: a) SEM image of a cross-section of sample D; b) Colour coded orientation map for the α phase obtained by EBSD on the cross-section (reference direction z_s), with hexagonal unit cells to illustrate the orientation of the grains 1, 2 and 3

Two other cross-sections with possible short crack transfer cases are presented in Figure 6-15. Figure 6-15a shows a cross-section of sample D and Figure 6-15b shows a cross-section of sample C1. The corresponding tilt and twist angles are presented in Table 6-2. It can be observed that, for all these cases, the tilt angle is relatively small. However, the twist angle is not always small. This is unusual, because it has been reported that the twist angle is the most important controlling parameter for short crack transfer through a grain boundary.[15-18] If the twist angle is large, crack transfer should be difficult, as has been explained in section 2.2.3. The observation of large twist angles in this case can be ascribed to the fact that the grain boundary is not well-defined. First of all, in an equiaxed microstructure the grain boundary cannot simply be described by a plane, because this does not take into account the grain boundary curvature. Second of all, the sections are two-dimensional, so it has to be assumed that the grain boundary plane normal [E] is perpendicular to z_S (see section 6.2.1). This assumption most likely causes large errors in the estimation of the twist angle. Therefore, another problem with applying the tilt and twist model in the current work, is that the correct orientation of the grain boundary plane cannot be determined, because this essentially requires 3D information. This issue has also been pointed out by King et al.[20] and Pineau.[21] Please note that in the cross-section shown in Figure 6-15a, the crack in grain 4 is also extending into the grain above, which has a green colour in the orientation map. In this grain, crack coalescence is occurring between the crack in grain 4 and the main crack, which formed the fracture surface. This type of crack coalescence, which has also been observed in Figure 5-12a, is not occurring on a specific crystallographic plane. Instead, it seems to be the result of plastic damage and void nucleation, which leads to a tortuous and non-planar crack path.

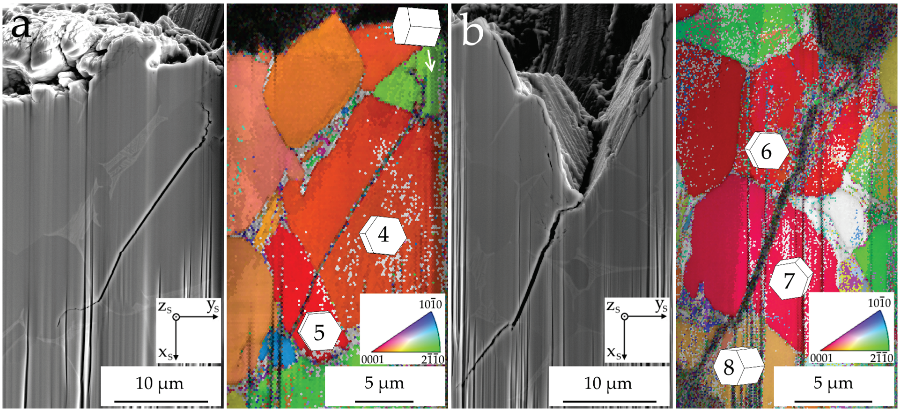

Figure 6-15: a) SEM image and colour coded orientation map of a cross-section of sample D (reference direction z_S), with hexagonal unit cells to illustrate the orientation of grains 4 and 5; b) SEM image and colour coded orientation map of a cross-section of sample C1 (reference direction z_S), with hexagonal unit cells to illustrate the orientation of grains 6, 7 and 8

Table 6-2: Tilt and twist angles for the short crack transfer cases presented in Figure 6-14 and Figure 6-15

	Tilt angle	**Twist angle**
Grain 1 and 2	2.4°	16.7°
Grain 4 and 5	15.1°	45.7°
Grain 6 and 7	18.3°	18.7°
Grain 7 and 8	13.6°	55.2°

Even though the obtained values of the twist angle are most probably not correct, the values for the tilt angle are still valid, because these do not depend on [E] (see equation 2.9). Therefore, it would be expected that the calculated tilt angles should still be relatively small if short crack transfer occurred. However, even this might not be the case here. Figure 6-16 shows another cross-section of sample D. This section cuts through two neighbouring facets, which are indicated by a circle in Figure 6-16a. The front view SEM image in Figure 6-16b shows that in this case there is no continuity between both facets. In other words, one facet does not directly extend into the other facet. However, the tilt angle for this case, obtained from the orientation data shown in Figure 6-16c, is only 8.1 degrees. Therefore, short crack transfer would be expected to have happened easily. Interestingly, this does not seem to have been the case. One possible explanation for this observation is that perhaps both facets first initiated independently, and then coalesced afterwards. Another possibility, however, is that the β phase region in between both grains affects the crack transfer behaviour. In fact, it has already been mentioned in section 5.3.2 and shown in Figure 5-12a that these regions, which often also contain secondary α, can act as an obstacle to crack growth. The tilt and twist model does not take this into account.

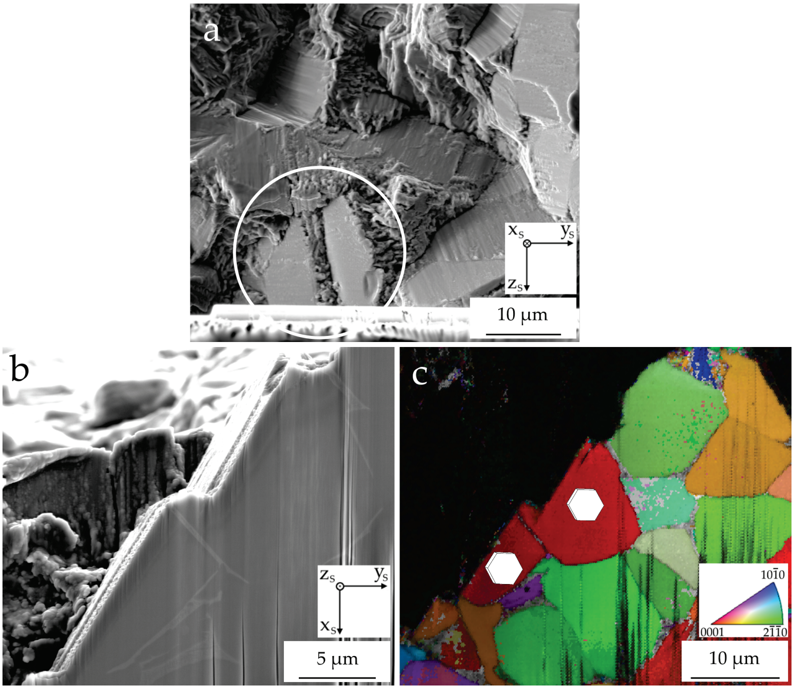

Figure 6-16: a) Top view SEM image of a cross-section of sample D, with a circle to indicate two sectioned facets; b) Front view SEM image of the two sectioned facets; c) Colour coded orientation map of the cross-section (reference direction z_s), with hexagonal unit cells to illustrate the orientation of the sectioned facets

6.2.3 Compatibility of slip systems – alignment factor analysis

An alternative approach to understanding why short crack transfer takes place in certain cases, is to draw a parallel to the problem of slip transfer between grains. Lee, Robertson and Birnbaum[22] suggested slip transfer criteria which determine whether there can be slip transfer from a specific slip system in one grain into a specific slip system in the neighbouring grain, known as the LRB criteria. Both slip planes intersect the grain boundary plane, and the first criterion is that the angle between these intersection lines should be small. Interestingly, this is completely similar to stating that the twist angle, in the tilt and twist model of Zhai et al.,[15] should be small. The second criterion for slip transfer is that the resolved shear stress on the outgoing slip system should be high. Finally, the third criterion states that the magnitude of the residual Burgers vector should be small. The LRB criteria have already been used to study slip transfer in titanium alloys.[23] However, it is clear that a complete analysis with these criteria would also require information on the grain boundary orientation. Therefore, a simplified equation has been derived by Guo et al.,[24] which can be used to calculate an alignment factor A:

$$\mathrm{A} = \frac{([\mathrm{N_i}]\cdot[\mathrm{N_j}])\cdot([\mathrm{b_i}]\cdot[\mathrm{b_j}])}{\|\mathrm{b_i}\|\cdot\|\mathrm{b_j}\|} \tag{6.1}$$

In this equation, possible slip transfer is considered between slip system i and slip system j. The slip plane normal vector is represented by [N] and the Burgers vector is represented by [b]. Essentially, the A factor simply expresses the compatibility between two slip systems, without taking into account the grain boundary shape and orientation. If both slip systems are well aligned, the A factor is high. For example, if both the slip plane and the slip direction (Burgers vector) would be perfectly aligned, the A factor would be equal to one. The methodology to calculate A factors from the EBSD data in this work is similar to the methodology that is used to calculate tilt and twist factors, as explained in section 6.2.1. For every prismatic slip system in a grain, the slip plane normal and the Burgers vector (see Figure 2-5 and Table 2-2) are defined in the crystal coordinate system (Figure 6-13a). These are then transformed to the sample coordinate system (Figure 6-13b) by using a rotation matrix, which depends on the Euler angles of the grain. The A factor can then be calculated from equation 6.1 for every combination of prismatic slip systems of the two considered grains. The highest A factor is retained, and describes the compatibility of the two most well-aligned slip systems.

For the short crack transfer case presented in Figure 6-14, the highest A factor between grains 1 and 2, for which crack transfer occurred, is found to be 0.99. The highest A factor between grains 2 and 3, for which no crack transfer is observed, is only 0.69. The highest A factors for the cases that are presented in Figure 6-15 are shown in Table 6-3. For all these cases, the slip systems in question are quite well-aligned, and consequently the A factor is relatively high. As a comparison, Guo et al.[24] found that slip transfer between grains could occur in CP titanium if A was larger than 0.7. The current results show that it seems that the A factor should indeed be high for crack transfer to occur. It is important to remark that this is in complete agreement with the statement that the tilt and twist angles should be small, because this is only possible if the two slip systems are well-aligned. However, it has been shown in the previous section that the tilt and twist model is not easily applicable in the current work. Although the A factor does not take into account the grain boundary orientation, it seems to be a more suitable approach in this case. On the other hand, the effect of β phase regions still remains unaccounted for. For example, the highest A factor for the case presented in Figure 6-16 is 0.99, while there doesn't appear to have been crack transfer. As mentioned earlier, it is also possible that in this case both facets first initiated independently, and then coalesced afterwards. This example shows that it is often not possible to distinguish between initiation facets and growth facets. Furthermore, this distinction might be even more difficult, because it cannot be excluded that in some cases one crack could have initiated throughout two grains, if these grains are oriented for easy slip transfer (expressed by a high A factor). In other words, two neighbouring grains with a similar orientation (high A factor) could behave as one large grain, which is somewhat similar to the situation when macrozones are present in the texture (see section 2.3.4).

Table 6-3: Alignment factors for the short crack transfer cases presented in Figure 6-14 and Figure 6-15

	A factor
Grain 1 and 2	0.99
Grain 4 and 5	0.96
Grain 6 and 7	0.87
Grain 7 and 8	0.85

The calculation of A factors may also be useful to explain the observation of slip transfer between grains with prismatic and basal slip, as has been discussed in chapter 5 (Figure 5-12b). This image, which is presented again in Figure 6-17, shows a cross-section through sample C1. Grain 1 contains several fine slip lines, parallel to a prismatic plane, which seem to extend into grain 2, in which they are parallel to the basal plane. If only prismatic slip systems would be considered for both grains, the highest A factor would be 0.35, which means that slip transfer is unlikely. However, if the basal slip systems are considered for grain 2, the highest A factor is 0.86, which explains why there was slip transfer from a prismatic slip system in grain 1 to a basal slip system in grain 2.

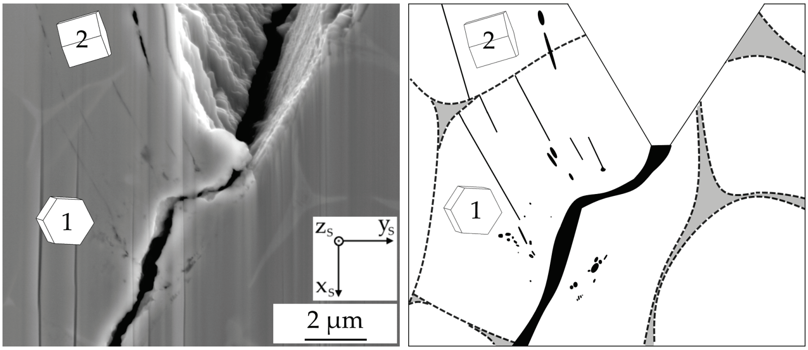

Figure 6-17: Cross-section through sample C1, together with a sketch, which outlines the grain boundaries (dotted lines) and α+β regions (grey areas), showing early stages of crack initiation and possible slip transfer between grains 1 and 2

6.3 Conclusions

In this chapter, the influence of the local texture on crack initiation and short crack growth has been investigated. Regarding crack initiation, this local texture provides some insights into which grains are susceptible to facet formation. The local orientation also affects faceted crack growth through grain boundaries, because these short cracks generally grow on prismatic planes. The orientations of faceted and neighbouring grains have been determined from EBSD measurements on cross-sections of fracture surfaces.

To answer the question of why facets form in certain grains, a Schmid factor and a Taylor factor analysis have been performed. Although it has been shown in the previous chapter that facets most likely form by a prismatic slip band mechanism, there is no clear difference between the prismatic Schmid factor of faceted grains and the average prismatic Schmid factor. Additionally, there is no clear trend regarding the local differences in prismatic Schmid factor between each faceted grain and its corresponding neighbouring grains. This can be explained by the fact that the Schmid factor analysis implicitly assumes that the stress is the same in every grain, which means that it cannot account for possible stress redistribution between grains. Therefore, a comparison of Taylor factors is more appropriate, because it assumes equal strain in every grain instead of equal stress. This way, a distinction can be made between "hard" grains, which are difficult to deform plastically and have a high Taylor factor, and "soft" grains, which are more easily deformed plastically and have a lower Taylor factor. It is found that the average Taylor factor of faceted grains is only slightly higher than the average Taylor factor. However, a local comparison has shown that the Taylor of each faceted grain has a tendency towards being higher than the Taylor factors of its corresponding neighbouring grains. This is logical from a stress redistribution point of view. If a "hard" grain is surrounded by "soft" grains, it will experience a higher stress, which can lead to facet formation. Although this analysis does not consider the differences in elastic stiffness between grains, it is argued that the Taylor factor can provide an indication of the stress distribution, due to the fact that the differences in stiffness in this case are relatively small. The use of Taylor factors is a novel approach to explain why certain grains are susceptible to facet formation. On the other hand, the anomalous facet in sample D, which was categorised as anomalous because of its different surface markings and near-basal orientation (see chapter 5), also behaves irregularly in the Schmid and Taylor factor analysis. Because of its orientation, both its basal and prismatic Schmid factor are relatively high, and as a result its Taylor factor is quite low. This observation casts doubt on the possibility of a cleavage formation mechanism for this facet. An alternative possibility is that this facet was formed by a basal slip band mechanism, although it remains unclear which explanation is correct. Finally, it is important to mention that not all neighbouring grains are considered, because the cross-sections are two-dimensional. Additionally, the β and secondary α phase regions have not been taken into account. It would be necessary to do a rigorous texture analysis in 3D on a large number of fracture surfaces in order to perform a more comprehensive study.

Short faceted crack growth through grain boundaries has been investigated for a selection of cross-sections. First, the tilt and twist angles have been derived for each case. These angles express the compatibility of the crack planes in both grains. It has been shown that the tilt angle is usually small in case of crack transfer. However, a correct calculation of twist angles would require more detailed information on the shape and spatial orientation of the grain boundaries. Again, this would require a thorough and time-consuming 3D analysis. Therefore, an alternative approach is used, in which the alignment factor A is calculated instead of tilt and twist angles. This A factor has been derived to investigate the possibility of slip transfer, and it expresses the compatibility of slip systems between two grains. If both slip systems are well-aligned, the A factor is high. The results of the analysis of selected cross-sections show that it seems that the A factor should indeed be high for crack transfer to occur. Although the A factor does not take into account the grain boundary shape or orientation, it therefore seems to be a more suitable approach in this case. On the other hand, the effect of β and secondary α phase regions still remains unaccounted for, while these can act as barriers to short crack growth.

6.4 References

[1] E. Schmid and W. Boas (1935). *Kristallplastizität Mit Besonderer Berücksichtigung der Metalle*, in *Struktur und Eigenschaften der Materie*, 17. Springer Berlin Heidelberg.

[2] S.L. Semiatin, M.G. Glavicic, S.V. Shevchenko, O.M. Ivasishin, Y.B. Chun, and S.K. Hwang (2009). *Modeling and Simulation of Texture*

Evolution during the Thermomechanical Processing of Titanium Alloys, Fundamentals of Modeling for Metals Processing. ASM Handbook, ASM International, 22A, p. 536-552.

[3] G.I. Taylor (1938). *Plastic strain in metals.* J. Inst. Metals, 62, p. 307.

[4] H.R. Piehler (2009). *Crystal-plasticity fundamentals, Fundamentals of modeling for metals processing.* ASM Handbook, ASM International, 22A, p. 232-238.

[5] M. Morita and O. Umezawa (2011). *Slip deformation analysis based on full constraints model for α-titanium alloy at low temperature.* Materials Transactions, 52(8), p. 1595-1602.

[6] J.F.W. Bishop and R. Hill (1951). *A theory of the plastic distortion of a polycrystalline aggregate under combined stress.* Philosophical Magazine 42, p. 414-427.

[7] P. Van Houtte (1988). *A comprehensive mathematical formulation of an extended Taylor-Bishop-Hill model featuring relaxed constraints, the Renouard-Wintenberger theory and a strain rate Sensitivity model.* Textures and Microstructures, 8, p. 313-350.

[8] F.P.E. Dunne and D. Rugg (2008). *On the mechanisms of fatigue facet nucleation in titanium alloys.* Fatigue & Fracture of Engineering Materials & Structures, 31(11), p. 949-958.

[9] D.F. Neal and P.A. Blenkinsop (1976). *Internal fatigue origins in alpha-beta titanium-alloys.* Acta Metallurgica, 24(1), p. 59-63.

[10] F.P.E. Dunne, A. Walker, and D. Rugg (2007). *A systematic study of hcp crystal orientation and morphology effects in polycrystal deformation and fatigue.* Proceedings of the Royal Society a-Mathematical Physical and Engineering Sciences, 463(2082), p. 1467-1489.

[11] M.R. Bache (1999). *Processing titanium alloys for optimum fatigue performance.* International Journal of Fatigue, 21, p. S105-S111.

[12] W.J. Evans (2004). *Time dependent effects in fatigue of titanium and nickel alloys.* Fatigue & Fracture of Engineering Materials & Structures, 27(7), p. 543-557.

[13] F. Bridier, P. Villechaise, and J. Mendez (2008). *Slip and fatigue crack formation processes in an alpha/beta titanium alloy in relation to crystallographic texture on different scales.* Acta Materialia, 56(15), p. 3951-3962.

[14] D. Tromans (2011). *Elastic anisotropy of hcp metal crystals and polycrystals.* International Journal of Research and Reviews in Applied Sciences, 6(4), p. 462-483.

[15] T. Zhai, A.J. Wilkinson, and J.W. Martin (2000). *A crystallographic mechanism for fatigue crack propagation through grain boundaries.* Acta Materialia, 48(20), p. 4917-4927.

[16] M. Marx, W. Schaf, H. Vehoff, and C. Holzapfel (2006). *Interaction of microcracks with selected interfaces: Focused ion beam for a systematic crack initiation.* Materials Science and Engineering a-Structural Materials Properties Microstructure and Processing, 435, p. 595-601.

[17] W. Schaef, M. Marx, H. Vehoff, A. Heckl, and P. Randelzhofer (2011). *A 3-D view on the mechanisms of short fatigue cracks interacting with grain boundaries.* Acta Materialia, 59(5), p. 1849-1861.

[18] T. Zhai, X.P. Jiang, J.X. Li, M.D. Garratt, and G.H. Bray (2005). *The grain boundary geometry for optimum resistance to growth of short fatigue cracks in high strength Al-alloys.* International Journal of Fatigue, 27(10-12), p. 1202-1209.

[19] D.P. Field (2004). *Textured Structures, Metallography and Microstructures.* ASM Handbook, ASM International, 9, p. 215-226.

[20] A. King et al. (2011). *Three-dimensional in situ observations of short fatigue crack growth in magnesium.* Acta Materialia, 59(17), p. 6761-6771.

[21] A. Pineau (2015). *Crossing grain boundaries in metals by slip bands, cleavage and fatigue cracks.* Philosophical Transactions of the Royal Society of London A: Mathematical, Physical and Engineering Sciences, 373(2038).

[22] T.C. Lee, I.M. Robertson, and H.K. Birnbaum (1990). *TEM in situ deformation study of the interaction of lattice dislocations with grain boundaries in metals.* Philosophical Magazine A, 62(1), p. 131-153.

[23] J. Shirokoff, I.M. Robertson, and H.K. Birnbaum (1993). *The Slip Transfer Process Through Grain Boundaries in HCP Ti.* MRS Proceedings, 319.

[24] Y. Guo, T.B. Britton, and A.J. Wilkinson (2014). *Slip band–grain boundary interactions in commercial-purity titanium.* Acta Materialia, 76, p. 1-12.

7 Influence of load holds on fatigue behaviour

Several titanium alloys, including Ti-6Al-4V, show dwell sensitivity, which means that the fatigue life reduces if load holds are introduced.[1-4] As has been explained in section 2.3.8, dwell fatigue loading consists of a trapezoidal waveform with a certain dwell or hold time at maximum load. This phenomenon, sometimes also called cold dwell or cold creep, is particularly important for aerospace applications.[1, 5] Interestingly, in case of failure due to dwell fatigue, the fracture surfaces also reveal the presence of quasi-cleavage facets (see Figure 2-23b), and crack initiation generally occurs internally.[1-4, 6-9] Because these observations are rather similar to what is seen in very high cycle fatigue experiments, it seems appropriate to also investigate dwell fatigue in drawn wires in order to achieve a better understanding of how crack initiation takes place. Of course, it is obvious that drawn wires are generally not suitable for airplane components. However, the previous chapters have shown that, in the case of drawn wires, the crystallographic texture, with the absence of "strong" grains that are oriented with their c-axis parallel to the loading direction, causes a different fatigue crack initiation behaviour compared to rolled or forged products. Therefore, performing dwell fatigue tests on these drawn wires might also lead to new insights regarding dwell fatigue phenomena.

This chapter contains the results of a limited number of dwell fatigue tests. First, the influence of introducing load holds on the fatigue life is investigated, by making a comparison with the fatigue life in case of regular (sinusoidal) fatigue tests, which have been discussed in chapter 4. The next section presents a fractographic analysis of a selection of fracture surfaces, in order to illustrate the crack initiation behaviour in case of dwell fatigue loading. Additionally, the strain accumulation during dwell fatigue testing is investigated. Finally, the results are discussed and compared with literature.

7.1 Fatigue life

Dwell fatigue tests are very time-consuming, because the duration of every load cycle is increased in comparison with regular fatigue tests. Consequently, only a limited number of tests have been done on samples with microstructure C (see Figure 3-1c):

- Two dwell fatigue tests with a hold time of 30 s at maximum load (labelled as samples DF30-1 and DF30-2)
- Two dwell fatigue tests with a hold time of 120 s at maximum load (labelled as samples DF120-1 and DF120-2)

- Four tests with first 1000 dwell fatigue cycles (hold time 120 s), followed by regular (sinusoidal) fatigue loading until fracture (labelled as samples DFF-1, DFF-2, DFF-3 and DFF-4)

Further details on the loading conditions have been provided in section 3.2.1. The maximum and minimum applied stress are respectively 750 MPa and 75 MPa for all samples. The fatigue life data for these tests are shown in Figure 7-1, together with the fatigue life data for regular fatigue tests on samples with the same microstructure (C). In Figure 7-1a, the fatigue life is expressed as cycles to failure, while Figure 7-1b shows the fatigue life as time (s) to failure. Please note that, although all tests are performed at the same stress levels, they are depicted at a different position on the vertical axis in order to improve the readability of these plots.

From Figure 7-1a, it can be observed that the amount of cycles to failure is reduced drastically if a hold time is introduced. For both the samples with 30 s load holds and the samples with 120 s load holds, there is a reduction of two to three orders of magnitude. Furthermore, even when only 1000 dwell fatigue cycles are added prior to regular fatigue testing, the amount of cycles to failure is significantly reduced. Evans[3] noted that dwell fatigue loading involves both cyclic and time dependent effects, while Ankem et al.[6] describe it as a combination of fatigue and creep testing. For this reason, it makes sense to also consider the fatigue life as time to failure instead of cycles to failure.

Figure 7-1b illustrates that in this case the data are more consistent. It can be seen that the dwell fatigue samples (DF30 and DF120) generally even fail after longer testing times compared to the regular fatigue samples. The sample with the longest lifetime, DF120-2, failed after approximately 47 days. The samples that were subjected to 1000 dwell fatigue cycles followed by regular fatigue testing (DFF-1 to 4) have lifetimes that are comparable to those of regular fatigue tests. However, more interestingly, the time to failure for these four samples is nearly identical. For these samples, the biggest difference in time to failure (between samples DFF-4 and DFF-1) is in fact only 11 minutes. These observations will be further discussed in section 7.4.

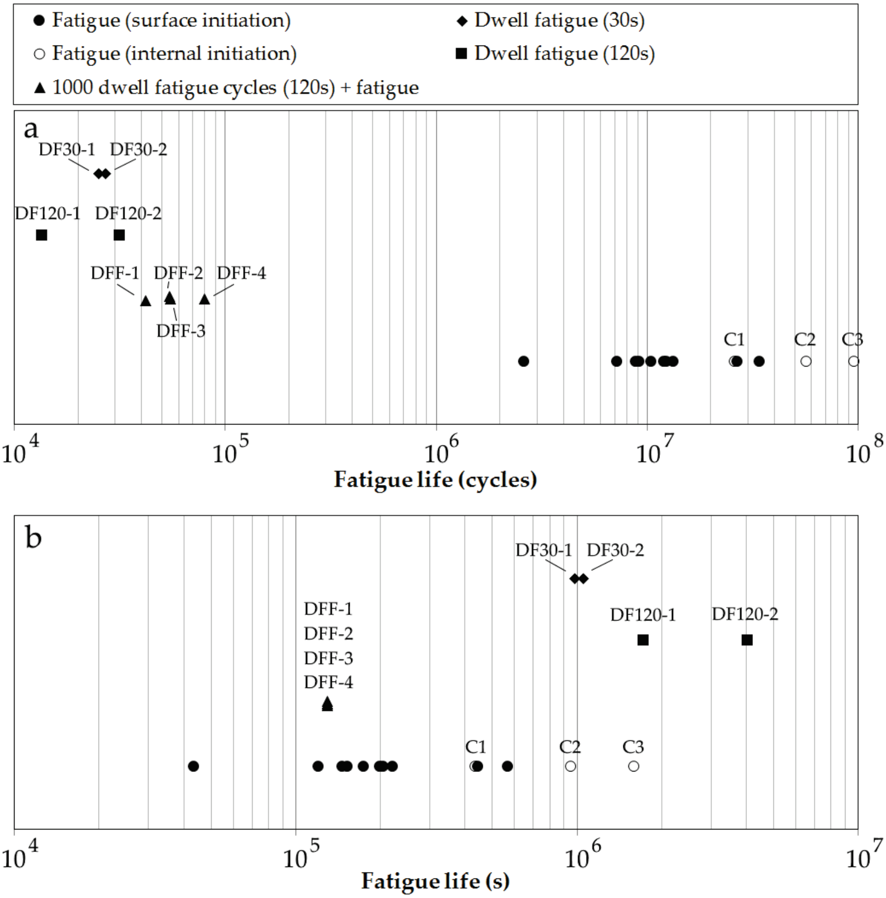

Figure 7-1: Fatigue life data of dwell fatigue tests with 30 s or 120 s hold time at maximum load, tests with 1000 dwell fatigue cycles (120 s hold time) followed by regular fatigue, and regular fatigue tests; σ_{max}=750 MPa, R=0.1 and microstructure C for all tests; Labels indicate sample nomenclature

7.2 Fractography

The fracture surfaces of dwell fatigue samples have been observed by SEM imaging in order to examine the crack initiation sites. For all samples, crack initiation occurred at the surface. This is illustrated in Figure 7-2a and b for samples DF30-2 and DFF-1, respectively. A close-up of the initiation area reveals that in both cases a facet is present at the surface of the sample, as indicated by the white circles. This facet is plausibly the crack initiation point. The angles of these facets have been measured, as described in section 3.2.2, and are found to be approximately 52 and 40 degrees for sample DF30-2 and DFF-1, respectively. It can be observed that other facets are present, a short distance away from the sample surface, which were presumably formed during short crack growth.

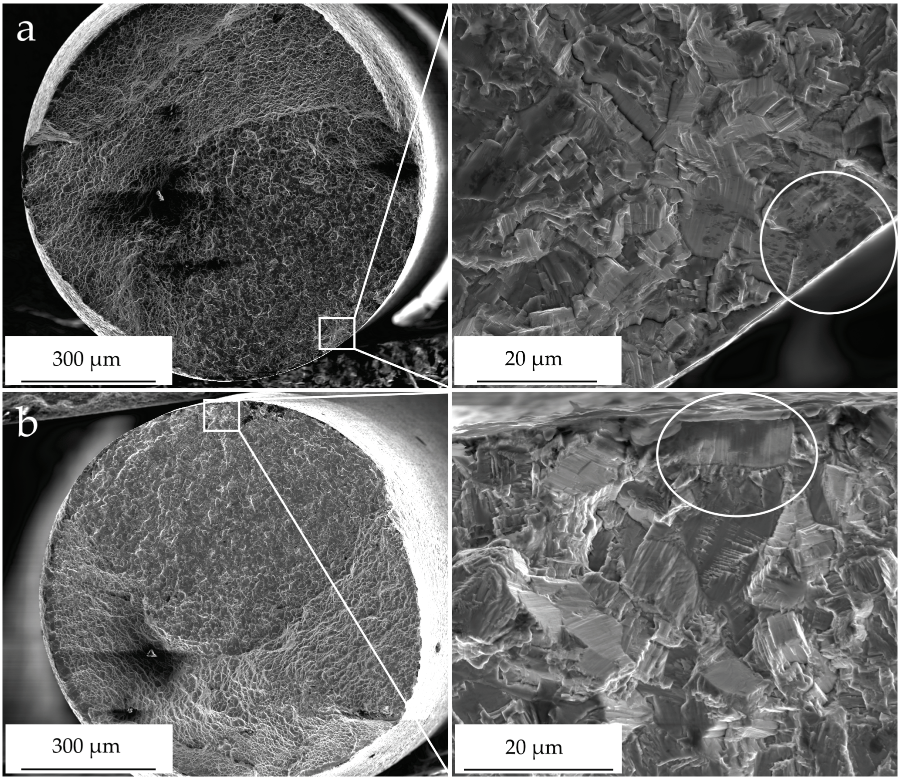

Figure 7-2: SEM images of fracture surfaces at low and high magnification, indicating the crack initiation location; a) Sample DF30-2; b) Sample DFF-1

In several samples, multiple crack initiation sites have been observed. Figure 7-3a and b illustrate this observation for sample DF30-2. In this case, a second crack initiation site is present at a certain distance from the fracture surface. This crack initiation site consists of two facets at the sample surface, which is comparable to the crack initiation sites shown in Figure 7-2.

Additionally, Figure 7-3c and d show SEM images of sample DF120-2. For this sample there are two crack initiation sites, similar to sample DF30-2. However, in this case a longer crack developed from both initiation sites. Therefore, it appears that this sample failed due to two simultaneously developing cracks on different planes, which ultimately connected. These observations suggest that, in the case of drawn wires, the introduction of load holds promotes surface crack initiation. This will be discussed further in section 7.4.

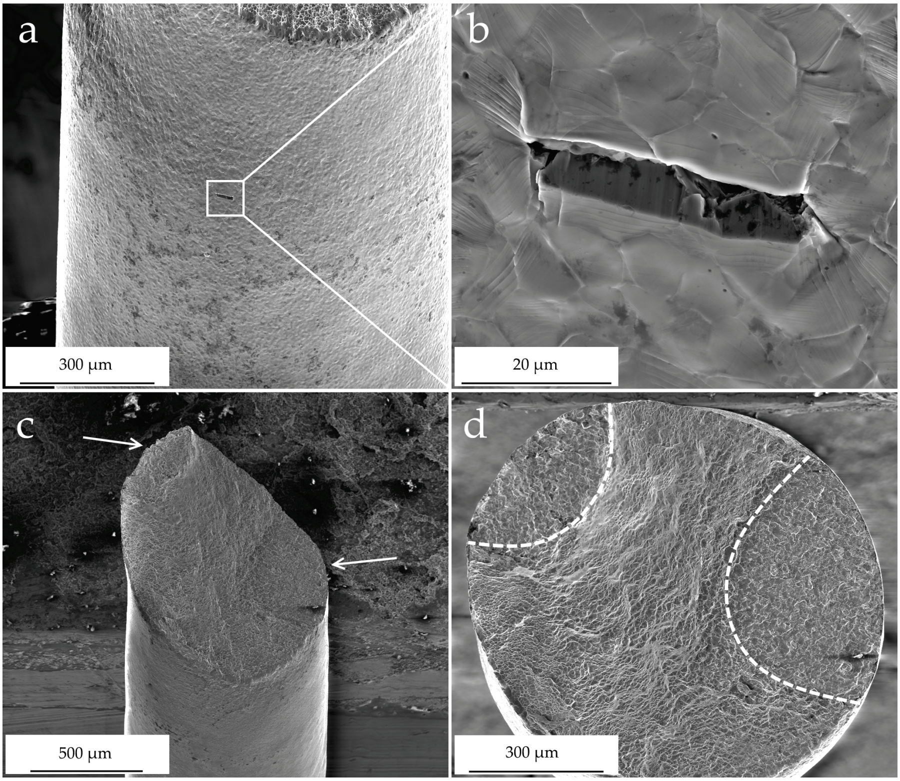

Figure 7-3: a) Side view SEM image of sample DF30-2 at a tilt angle of 45°; b) Close-up of (a), revealing another faceted surface crack initiation site in this sample; c) Side view SEM image of sample DF120-2 at a tilt angle of 45°, with arrows to indicate the two crack initiation locations; d) SEM image of fracture surface of sample DF120-2, with dotted lines enclosing the two dwell fatigue crack growth areas

7.3 Strain accumulation

It has been reported that strain accumulation plays a central role in the phenomenon of dwell sensitivity in titanium alloys.[3] Therefore, it is useful in the current case to see whether introducing load holds affects this accumulation, and also whether it is dependent on the hold time. Figure 7-4 shows the evolution of the maximum strain level as a function of time for samples DF30-1, DF30-2, DF120-1, DF120-2, C1, C2 and C3. A first observation is that the increase in maximum strain is larger for the dwell fatigue samples compared to the pure fatigue samples, which is in agreement with the results of Dunne et al.,[10] who modelled dwell fatigue by using a crystal plasticity model. Additionally, the maximum strain increases more rapidly for samples DF30-1 and DF30-2 than it does for samples DF120-1 and DF120-2. This observation seems surprising, given the fact that the latter samples are subjected to the maximum load for longer periods.

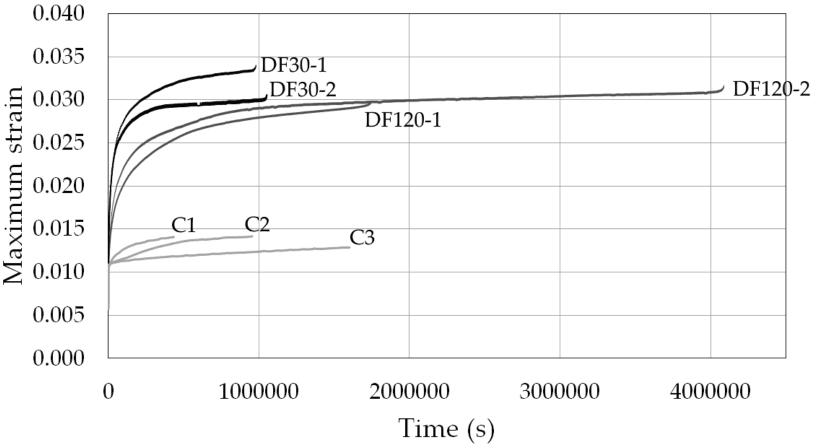

Figure 7-4: Maximum strain as a function of time (s) for samples DF30-1 and DF30-2 (dwell fatigue with 30 s load holds), samples DF120-1 and DF120-2 (dwell fatigue with 120 s load holds) and samples C1, C2 and C3 (regular fatigue)

In order to understand this behaviour, it is necessary to investigate the strain evolution during a loading cycle. Figure 7-5 shows the strain as a function of time during the first loading cycles of sample DF30-1 and sample DF120-2. It can be seen that during each load hold the strain gradually keeps on increasing. However, the rate of this strain increase becomes smaller during the load hold. In other words, the strain increases faster at the beginning of each load hold than it does near the end. The initial strain rate during each maximum load hold is also higher than the strain rate at the end of the previous maximum load hold. Consequently, the maximum strain increases more rapidly in the tests with a 30 s hold time, because there are more frequent unloading periods. This effect, which is shown in Figure 7-4, can already be observed after a few cycles (Figure 7-5).

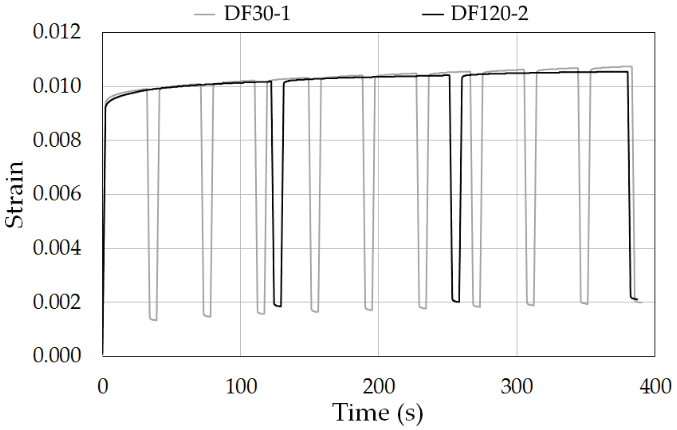

Figure 7-5: Strain in sample DF30-1 and sample DF120-2 as a function of time during the first cycles

Furthermore, the total strain increase during each load cycle decreases for each progressive cycle. This is illustrated more clearly in Figure 7-6, which shows the strain evolution for sample DF30-1 during the 1st, 100th, 1000th and 10000th cycle as a function of the time in each cycle. For cycle 1, the strain visibly increases during the maximum load hold (between lines E and F), while the strain increase during the maximum load hold of cycle 10000 is barely noticeable in this graph. In fact, the strain increase during the maximum load hold in cycles 1, 100, 1000 and 10000 for sample DF30-1 is respectively 5.3 x 10^{-4}, 1.3 x 10^{-4}, 9.5 x 10^{-5} and 7.6 x 10^{-5}, approximately. Finally, as mentioned in section 3.2.1, the time in between the maximum load holds is 5 s. During these periods, the load is kept constant at a level that corresponds to an original stress level of 75 MPa. It can be seen in Figure 7-6 that during these minimum load holds (between lines G and H), the strain actually decreases. This strain decrease is nearly constant for each cycle. Specifically, for cycles 1, 100, 1000 and 10000 the strain decrease in sample DF30-1 is respectively 9.5 x 10^{-5}, 1.1 x 10^{-4}, 9.6 x 10^{-5} and 9.5 x 10^{-5}, approximately. Similar values have been found for sample DF120-2. These observations will be discussed in section 7.4.

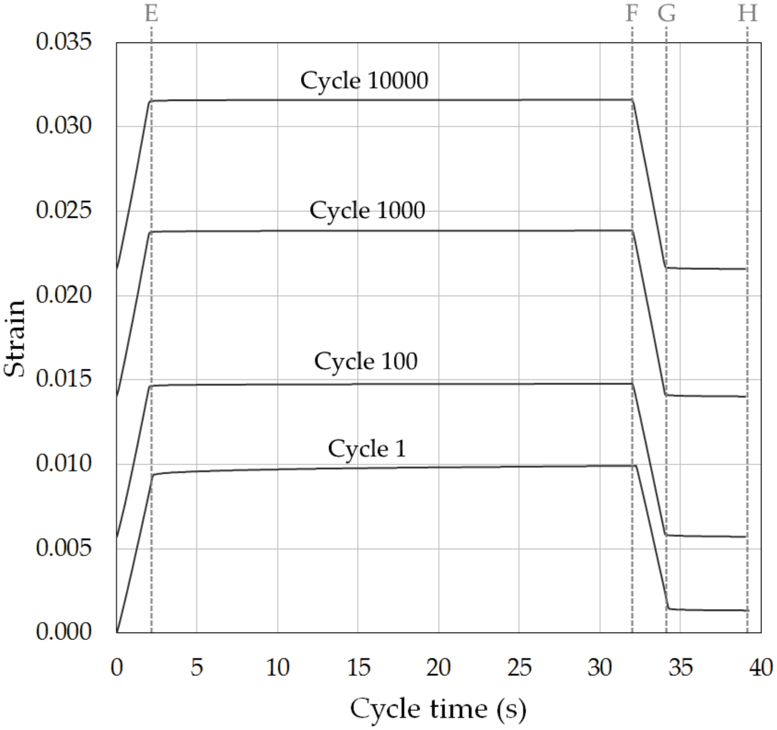

Figure 7-6: Strain evolution during the 1st, 100th, 1000th and 10000th cycle for sample DF30-1; Maximum load hold occurs between lines E and F, minimum load hold occurs between lines G and H

7.4 Discussion

It has been shown that the fatigue life, expressed as cycles to failure, decreases dramatically if load holds are introduced. As discussed in section 2.3.8, this behaviour has already been reported by several authors,[1-4] and is generally attributed to the phenomenon of load shedding,[6, 11] which leads to damage in the form of facets.[3] Load shedding involves a time-dependent stress redistribution among grains, which depends on the grain orientations. During a load hold, there will be plastic deformation of soft grains, because they are oriented for easy dislocation slip. Hard grains, which are oriented with their c-axis close to the loading axis, will not deform plastically (see also section 2.1.2). After unloading, the soft grains are consequently under a compressive stress, so that during the next loading cycle the stress in these grains is lower. The result of this behaviour is that, as time progresses, the stress in the strong grains increases. After a certain time this stress can reach a critical level, leading to the formation of quasi-cleavage facets in the strong grains (see Figure 2-24).[6, 12] This would also explain why crack initiation is generally reported to occur internally in Ti-6Al-4V during dwell fatigue, because grains near the surface of the sample can deform more freely. The quasi-cleavage facets, in case of dwell fatigue loading, are consistently reported to form on a basal plane of a hard grain, which is nearly perpendicular to the loading direction.[1, 3, 4, 7, 11, 13, 14] The model proposed by Evans and Bache[7] is usually described to explain the formation mechanism of these facets (see Figure 2-18).

However, the current results show that the introduction of load holds apparently promotes crack initiation at the surface. This statement is supported by the observation of multiple surface crack initiation sites, even though the number of tests is limited. The reason for this different behaviour most probably lies in the different texture of drawn wires. It has already been mentioned in chapter 5 that the different facet formation behaviour, in case of regular fatigue loading, is a result of the fact that there are virtually no hard grains in these wires (see also the texture measurements in section 3.1.2). As a result of the absence of hard grains, the build-up of internal stresses during dwell fatigue loading, due to load shedding, is limited. Instead, it is observed that crack initiation occurs by facet formation at the surface. Surface crack initiation normally also takes place because of a stress concentration. In this case, it is likely that this stress concentration is caused by the gradual formation of intrusions and extrusions, due to an accumulation of slip steps (see also section 2.2.1). These slip traces have actually been observed, for example on the surface of sample DF30-2 (Figure 7-3b). It would be expected that this mechanism happens more easily in a surface grain that is oriented for very easy dislocation slip. This is in agreement with the measured facet angles (52 and 40 degrees), because planes around 45 degrees are subjected to the highest shear stress.

Additionally, it has been mentioned in section 7.1 that four samples were subjected to an initial 1000 dwell fatigue cycles (with a hold time of 120 s), followed by regular fatigue testing until failure. Interestingly, the time to failure for these four samples (DFF-1 to 4) was found to be nearly identical. This may not be a coincidence, if it is assumed that strain localization already takes place in a few surface grains during the first 1000 dwell fatigue cycles. This assumption is not unrealistic, because the rate of strain accumulation is the highest during the first cycles (see Figure 7-4 and Figure 7-6). Furthermore, Sackett et al.[9] performed dwell fatigue tests on a large grained titanium alloy, and found that, by strain mapping, the crack initiation location could already be identified during the first load hold. Therefore, it is plausible that for samples DFF-1 to 4 the initial 1000 dwell cycles caused localized damage in a few surface grains. When these samples were then subjected to regular fatigue testing, the remaining fatigue life was controlled by crack growth, rather than crack initiation. This could be the reason why the differences in time to failure between these samples are very small.

It has also been observed that the maximum strain increases more rapidly in tests with 30 s load holds than it does in tests with 120 s load holds (see Figure 7-4). This can be taken one step further by comparing the strain increase during dwell fatigue tests with the strain increase during an actual creep test. This comparison is presented in Figure 7-7. This graph shows the strain evolution during the first 8000 s for samples DF30-1 and DF120-2, together with the strain evolution during a creep test, for which the load is kept constant at a level that corresponds to an initial stress level of 750 MPa. It can be observed that the strain quickly becomes nearly constant during the creep test. This is rather logical, because the applied stress level is below the macroscopic yield stress and the test is done at room temperature. The same behaviour has been observed by Evans,[3] who performed creep tests on bimodal Ti-6Al-4V at different stress levels. Pilchak and Williams[8] did a creep test under similar conditions on a Ti-8Al-1Mo-1V alloy, and found that their specimen did not fail, even after a very long time (426 hours). All of these results show that the unloading steps, in between maximum load holds, play a very important role during dwell fatigue. In the current work, the samples with 30 s load holds (DF30) have shorter fatigue lives (in time) compared to the samples with 120 s load holds (DF120), as has been shown in Figure 7-1b. This is probably caused by faster crack initiation due to the faster strain accumulation in the samples with 30 s load holds. This in turn is a result of the fact that there are more unloading periods, because the initial strain rate after each unloading period is higher than it was at the end of the previous maximum load hold (see Figure 7-5).

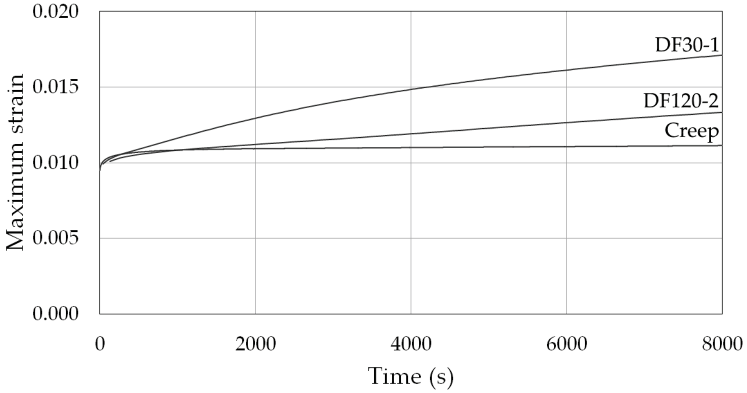

Figure 7-7: a) Strain evolution during the first 8000 s for sample DF30-1 (30 s hold time), sample DF120-2 (120 s hold time) and for a sample subjected to a static load corresponding to an initial stress level of 750 MPa (creep test)

Additionally, from the strain evolution curves in Figure 7-7 the creep rates can be estimated. Figure 7-8 shows the creep rates of samples DF30-1, DF120-2, the sample subjected to a creep test and sample C2. Each creep rate value was determined as the slope of a linear least squares fit of the maximum strain data between 6000 and 8000 s. From this plot it can be observed that the creep rate is higher for the sample with 30 s load holds (DF30-1) compared to the sample with 120 s load holds (DF120-2), while the sample with continuous loading (creep) shows an even lower creep rate. However, more interestingly, the regular fatigue sample (C2) also shows a lower creep rate than the sample with 30 s load holds. In other words, decreasing the hold time from 120 s to 30 s leads to a higher creep rate, while decreasing it from 30 s to approximately 0 s (in a fatigue test with a load frequency of 60 Hz) leads to a lower creep rate. This means that plausibly there is a hold time, in the grey region indicated in Figure 7-8, for which the creep rate would be maximum and, consequently, the amount of cycles to failure would be the lowest.

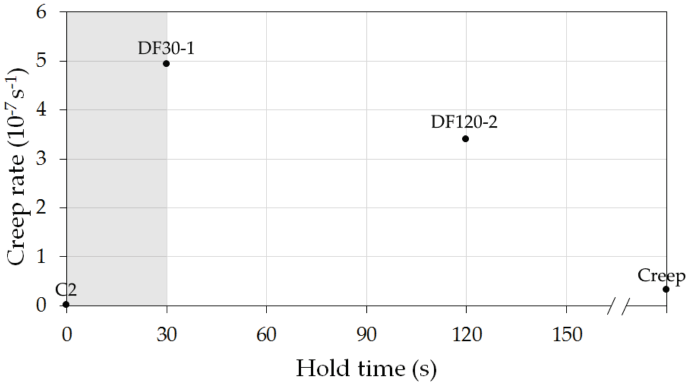

Figure 7-8: Creep rate as a function of the maximum load hold time for samples C2, DF30-1, DF120-2 and a creep test

Finally, it should be questioned which mechanisms are controlling the strain evolution during the maximum and minimum load holds. It has been observed that the strain increases during each maximum load hold, but that the increase rate decreases. This can be considered as normal primary creep behaviour, with the exception that the tests are done at room temperature. This behaviour can generally be explained by strain hardening, which involves a rapid multiplication of dislocations when the stress is initially applied. As the dislocation density increases, dislocations then act as barriers to the motion of other dislocations, which causes the decrease in strain rate.[15, 16] Additionally, the interaction of dislocations with interstitials is believed to play an important role in controlling room-temperature creep in titanium alloys.[17]

The explanation for the strain decrease during each minimum load hold, and the increased strain rate upon reloading, seems to be more complicated. A small decrease in strain after unloading has already been noticed by other authors.[18-20] Interestingly, in the current work this happens while there is still a small tensile load on the sample (corresponding to an initial stress level of 75 MPa). In other words, the material is slightly contracting, although it is under a small tensile load. The hold time at minimum load was chosen to be 5 s for all dwell fatigue tests (see section 3.2.1). However, interrupted creep tests by other authors have shown that this creep recovery is time-dependent.[20, 21] One extreme example is shown in Figure 7-8a, which presents the strain evolution of an interrupted creep test on a Ti-6242 sample, as performed by Thirumalai.[20] At point A the sample was unloaded, and stored at room temperature for 11 months. Afterwards, the creep test was continued, and it was observed that the creep rate was much higher than before the interruption. Barkia et al.[19] describe this behaviour as an "aging-induced rejuvenation of the creep potential". One possible explanation for this phenomenon has been proposed by Brandes and Mills,[21] who performed TEM measurements on Ti-6Al samples after creep loading. They observed screw dislocations in the grain interiors and planar dislocation pile-ups at grain boundaries, and suggested that after unloading, these pile-ups are locked by high frictional forces. This creates stress concentrations, which provide the driving force for continued local plasticity in the grain interiors, without an external load. This mechanism is thermally activated, as it is enhanced by longer aging periods or by a higher temperature, and would also depend on the degree of Al atom ordering.

The current results show that this driving force is apparently sufficiently large to cause a strain decrease even when there is still a small tensile load applied to the material. Similar "negative creep" behaviour has been observed by Brandes and Mills[21] when they reloaded a sample to a lower load immediately after creep loading. Additionally, Barkia et al.[19] suggested that the presence of hydrogen and oxygen could play a role in the strain recovery behaviour, because these interstitials also influence dislocation movement. They performed interrupted creep tests on pure Ti with different hydrogen contents, and found that the recovery process was more prominent for a higher hydrogen content (see Figure 7-8b). Hydrogen diffusion would then presumably explain the time-dependency. It has been reported elsewhere that hydrogen seems to favour dislocation pile-ups.[22] Oxygen, on the other hand, has the opposite effect of hydrogen, plausibly because it reduces the mobility of screw dislocations.[19]

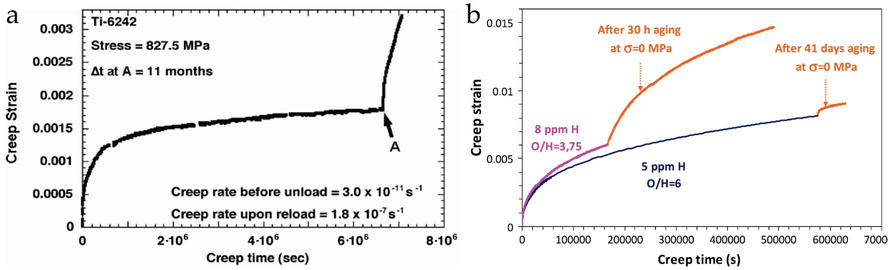

Figure 7-9: a) Strain as a function of time during a creep test of a Ti-6242 specimen at room temperature; Point A indicates a time gap of 11 months during which this specimen was kept unloaded, and after which it was reloaded again[20]; b) Strain as a function of time during interrupted creep tests of high purity Ti with different hydrogen contents[19]

It is clear that dislocation mechanisms are controlling the recovery phenomenon that occurs after unloading from a constant load hold, even though the details are not yet fully understood.[19, 21] However, the implications of this phenomenon on dwell fatigue are even less clear.[18, 23] The results in this work show that, for a constant minimum load hold time of 5 s, the strain decrease was also nearly constant (between 9.5 x 10^{-5} and 1.1 x 10^{-4} for sample DF30-1). It is possible that a longer hold time at minimum load would lead to a further decrease in strain, but, more importantly, could also lead to a faster increase in strain during the next maximum load hold, because of this recovery phenomenon. Therefore, increasing the hold time at minimum load might lead to a reduction in fatigue life (expressed as cycles to failure). This seems to be an interesting hypothesis for possible future work.

7.5 Conclusions

A limited number of dwell fatigue tests have been performed on drawn Ti-6Al-4V wires, because there appear to be similarities between the crack initiation behaviour during fatigue and dwell fatigue loading. More specifically, during dwell fatigue loading, which can be described as a trapezoidal waveform with a certain hold time at maximum and at minimum load, cracks are generally found to initiate internally by facet formation. However, in the current work it is observed that, in drawn wires, the introduction of load holds promotes crack initiation at the surface. Moreover, multiple surface crack initiation sites have been identified in several samples. The crystallographic texture is most probably the reason why there is no internal crack initiation in drawn wires during dwell fatigue loading. This is due to the fact that there are virtually no hard grains, with their c-axis parallel to a loading axis. For this reason, the phenomenon of load shedding is less pronounced, and there is no formation of internal facets. Instead, surface crack initiation occurs through the formation of a facet at the surface, in a grain that is presumably oriented for very easy slip. The introduction of load holds leads to a drastic reduction in the amount of cycles to failure in comparison to regular fatigue tests without load holds. However, the time to failure remains similar, and is even higher for some dwell fatigue tests. Four samples were subjected to an initial 1000 dwell fatigue cycles with a hold time of 120 s at maximum load, followed by regular fatigue testing until failure. The time to failure for these four samples was found to be nearly identical. It is suspected that damage localization occurs during the first 1000 dwell fatigue cycles, which means that the remaining fatigue life of these samples was mostly controlled by crack growth rather than crack initiation.

During dwell fatigue tests, there is a significant increase of the maximum strain over time. Additionally, the maximum strain increases more rapidly in tests with 30 s load holds than it does in tests with 120 s load holds at maximum load. This can be explained by the strain evolution during the maximum load holds and the recovery that occurs during the minimum load holds. It has been observed that the strain increases during each maximum load hold, but that the increase rate decreases. During each minimum load hold, the strain decreases, even though a small tensile load is still applied. This remarkable behaviour is believed to be the result of dislocation interactions, which are not yet fully understood. The recovery process during each minimum load hold leads to an increased initial strain rate during each following maximum load hold. Because this strain recovery is reported to be time-dependent, it is likely that the hold time at minimum load will also affect the fatigue life.

7.6 References

[1] M.R. Bache (2003). *A review of dwell sensitive fatigue in titanium alloys: the role of microstructure, texture and operating conditions.* International Journal of Fatigue, 25(9-11), p. 1079-1087.

[2] V. Doquet and V. De Greef (2012). *Dwell-fatigue of a titanium alloy at room temperature under uniaxial or biaxial tension.* International Journal of Fatigue, 38, p. 118-129.

[3] W.J. Evans (2004). *Time dependent effects in fatigue of titanium and nickel alloys.* Fatigue & Fracture of Engineering Materials & Structures, 27(7), p. 543-557.

[4] M.T. Whittaker, W.J. Evans, and W. Harrison (2009). *Time Dependent Fatigue Fractures of Titanium Alloys.* 12th International Conference on Fracture, Ottawa, 1, p. 2023-2031.

[5] R.R. Boyer (1996). *An overview on the use of titanium in the aerospace industry.* Materials Science and Engineering A, 213(1-2), p. 103-114.

[6] S. Ankem, H. Margolin, C.A. Greene, B.W. Neuberger, and P.G. Oberson (2006). *Mechanical properties of alloys consisting of two ductile phases.* Progress in Materials Science, 51(5), p. 632-709.

[7] W.J. Evans and M.R. Bache (1994). *Dwell-sensitive fatigue under biaxial loads in the near-alpha titanium alloy IMI685.* International Journal of Fatigue, 16(7), p. 443-452.

[8] A.L. Pilchak and J.C. Williams (2011). *Observations of Facet Formation in Near-alpha Titanium and Comments on the Role of Hydrogen.* Metallurgical and Materials Transactions a-Physical Metallurgy and Materials Science, 42A(4), p. 1000-1027.

[9] E.E. Sackett, L. Germain, and M.R. Bache (2007). *Crystal plasticity, fatigue crack initiation and fatigue performance of advanced titanium alloys.* International Journal of Fatigue, 29(9-11), p. 2015-2021.

[10] F.P.E. Dunne, D. Rugg, and A. Walker (2007). *Lengthscale-dependent, elastically anisotropic, physically-based hcp crystal plasticity: Application to cold-dwell fatigue in Ti alloys.* International Journal of Plasticity, 23(6), p. 1061-1083.

[11] F.P.E. Dunne and D. Rugg (2008). *On the mechanisms of fatigue facet nucleation in titanium alloys.* Fatigue & Fracture of Engineering Materials & Structures, 31(11), p. 949-958.

[12] M.H. Pourian, F. Bridier, P. Pilvin, and P. Bocher (2016). *Prediction of crack initiation sites in alpha Ti-alloys microstructures under dwell-fatigue using Cellular Automaton simulation method.* International Journal of Fatigue, 85, p. 85-97.

[13] W.J. Evans and M.R. Bache (1995). *Hydrogen and fatigue behavior in a near alpha-titanium alloy.* Scripta Metallurgica Et Materialia, 32(7), p. 1019-1024.

[14] M. Whittaker (2011). *Titanium in the Gas Turbine Engine.* Advances in Gas Turbine Technology, ed. E. Benini. InTech

[15] J.C. Gibeling (2000). *Creep deformation of metals, polymers, ceramics, and composites, Mechanical Testing and Evaluation.* ASM Handbook, ASM International, 8, p. 363-368.

[16] G.E. Dieter (1961). *Mechanical Metallurgy.* New York, USA. McGraw-Hill Book Company

[17] K. Stetina (1980). *Creep of titanium between 30 °C and 300 °C.* Proceedings of the International Conference on Engineering Aspects of Creep, Sheffield, 1, p. 19-24.

[18] G. Lütjering and J.C. Williams (2007). *Titanium.* 2nd ed, ed. B. Derby. Springer Berlin Heidelberg New York

[19] B. Barkia, V. Doquet, J.P. Couzinié, and I. Guillot (2015). *Room-temperature creep and stress relaxation in commercial purity titanium–Influence of the oxygen and hydrogen contents on incubation phenomena*

and aging-induced rejuvenation of the creep potential. Materials Science and Engineering: A, 624, p. 79-89.

[20] N. Thirumalai (2000). *Low temperature creep of titanium alloys : microstructure, deformation mechanisms and modeling.* Ph.D. Thesis, Ohio State University.

[21] M. Brandes and M.J. Mills (2004). *Static recovery in titanium alloys at lower temperatures.* Materials Science and Engineering a-Structural Materials Properties Microstructure and Processing, 387, p. 570-575.

[22] C. Sarrazin-Baudoux (2005). *Abnormal near-threshold fatigue crack propagation of Ti alloys: role of the microstructure.* International Journal of Fatigue, 27(7), p. 773-782.

[23] T.B. Britton, F.P.E. Dunne, and A.J. Wilkinson (2015). *On the mechanistic basis of deformation at the microscale in hexagonal close-packed metals.* Proceedings of the Royal Society A: Mathematical, Physical and Engineering Science, 471(2178).

8 Conclusions and suggestions for future research

In this work, the phenomenon of internal crack initiation in titanium alloys has been studied by performing fatigue tests on drawn Ti-6Al-4V wires. Most research on this phenomenon has been done on forged or rolled material, and **to the author's knowledge this is the first time that the fatigue behaviour of drawn Ti-6Al-4V wires has been investigated**. Internal crack initiation occurs because of the formation of facets, which are fractured α grains. The α grain size has been altered by applying various heat treatments, in order to investigate its effect on internal crack initiation and facet formation. The observed facets have been analysed in detail, in order to reveal how and why they were formed. Additionally, the effect of introducing a hold time at maximum load has been investigated by performing dwell fatigue tests. In this chapter, the most important results and conclusions of this work are summarized, and some suggestions for possible future work are provided.

8.1 Conclusions

From a literature study, it is found that the stress distribution at the microscale plays a central role in the formation of facets. This stress distribution depends on the local grain orientations, and is significant because the hcp α phase is highly anisotropic. More specifically, α grains that are loaded along the c-axis are both elastically and plastically difficult to deform. These grains are consequently considered as "hard" or strong grains, while easily deformable grains are called "soft" or weak grains. There is a lack of consensus in literature regarding the mechanism of facet formation, and the suggested mechanisms can generally be categorized in two groups. The first group of authors propose that facets are formed by cleavage of α grains, while the second group of authors believe that facets are the result of slip band formation. The crystallographic texture has an important influence on internal crack initiation and growth, because facets are found to grow on specific crystallographic planes. These are reported to be either a basal, near-basal, prismatic or in some cases pyramidal lattice plane.

Fatigue tests with a load ratio of 0.1 have been performed on drawn and electrochemically polished Ti-6Al-4V wires (diameter 1 mm) with four different microstructures. These four microstructures have been obtained by heat treating, and contain primary α grains with average sizes of approximately 1, 2, 5 and 10 μm. β phase regions with secondary α rods are present in between the primary α grains. The crystallographic texture is found to be different in comparison with forged or rolled Ti-6Al-4V, which is typically used for research on internal fatigue crack initiation. More specifically, texture measurements on cross-sections of the drawn wires show that there are virtually no "hard" grains, with their c-axis nearly parallel to the wire axis. Instead, there is a high tendency for grains to be oriented with the normal direction of the prismatic $\{10\bar{1}0\}$ planes parallel to the wire axis. The fatigue life is found to decrease if the primary α grain size is increased. The fatigue life data form two clusters for each microstructure. One group of samples has short fatigue lives because they contain surface defects, which lead to easy crack initiation. The second group of samples has longer fatigue lives, and includes samples with internal crack initiation and run-out samples. In total, four samples broke due to an internal crack: three samples with average alpha grain size 5 μm, which failed after 2.6 x 10^7, 5.7 x 10^7 and 9.6 x 10^7 cycles, and one sample with average alpha grain size 10 μm, which failed after 7.6 x 10^6 cycles. For these four samples there is no correlation between the depth of crack initiation and the fatigue life. The crack initiation areas contain numerous facets and are found to have a high roughness, which has been measured by digitally reconstructing the fracture surfaces in 3D. The projected size of these areas is nearly constant and not linked to the fatigue life. The estimated threshold stress intensity factor range ΔK_{th} is found to be between 6 and 8 MPa√m if an elliptical shape is used to approximate the area, which is consistent with literature. Lower values are obtained if a freeform approximation, which includes all facets, is used. Interestingly, **the actual surface area of the crack initiation and short crack growth region, which takes into account the roughness, is found to be correlated to the fatigue life. This suggests that the formation mechanisms of this area, rather than its projected threshold size, control the fatigue life in the VHCF regime.**

The facets at internal crack initiation sites have been analysed in detail in terms of their appearance, their spatial orientation and their crystallographic orientation. **Contrary to what is observed in literature, the facets are not smooth, but show roughness at the nanoscale.** This roughness has a linear appearance for nearly all facets, except for one anomalous facet in the sample with the largest grain size, which shows a fan-shaped pattern. The facets have inclination angles that are mostly between 50 and 70 degrees, which is higher than the values that are found in literature. Additionally, wear markings are observed in some cases, which are most probably the result of crack face sliding. This friction wear due to crack closure can be attributed to the fact that the facets are at relatively steep angles. From EBSD measurements on cross-sections of the fracture surfaces, which were made by FIB milling, it is found that nearly all of the examined facets are parallel to a prismatic plane. Additionally, the linear markings coincide with the slip direction of the prismatic slip system. Only the anomalous facet, in the sample with the largest grain size, has a near-basal orientation. **These observations show that facets can be formed by either a slip-based mechanism or a cleavage-based mechanism, and**

that the alpha grain size is plausibly one of the parameters that controls which mechanism occurs.

In order to explain why facets are formed in specific grains, the local texture has been analysed in terms of Schmid and Taylor factors. Although most facets are presumably formed as a result of prismatic slip band formation, no difference has been observed between the average prismatic Schmid factor of faceted grains and the total average prismatic Schmid factor. Additionally, the differences in prismatic Schmid factor between each faceted grain and its corresponding neighbouring grains do not follow a clear trend. Therefore, the Schmid factor is found to be inadequate in explaining why certain grains are susceptible to facet formation. The Schmid factor cannot account for possible stress redistribution between grains, because its calculation implies the assumption of equal stress in each grain. The Taylor factor, on the other hand, describes how difficult it is for grains to deform plastically, assuming that the strain is the same for each grain. Plastically "hard" grains have a high Taylor factor, while "soft" grains have a low Taylor factor. The average Taylor factor of faceted grains is found to be only slightly higher than the total average Taylor factor. However, **a local comparison shows that the Taylor of each faceted grain has a tendency towards being higher than the Taylor factors of its corresponding neighbouring grains. If a hard grain is surrounded by soft grains, it experiences a higher stress and is more susceptible to facet formation.** Although this analysis does not consider the differences in elastic stiffness between grains, it is suggested that the Taylor factor can provide an indication of the stress distribution, due to the fact that the differences in stiffness in this case are relatively small. **The use of Taylor factors is a novel approach to explain this behaviour**. The anomalous facet, on the other hand, has a lower Taylor factor compared to its neighbouring grains, because it is oriented for relatively easy slip on both prismatic and basal slip systems. This observation is another indication that the anomalous facet was formed by a different mechanism, which could be either basal slip band formation or cleavage. In the latter case, facet formation by cleavage could be caused by a dislocation pile-up on a prismatic plane, which would result in a high normal stress on the near-basal cleavage plane.

In some cross-sections, secondary facets are found below the fracture surface, as well as indications of early stage crack initiation and short crack growth. **These observations show that facets can extend through more than one grain, and that there is crack coalescence between facets.** The tilt and twist angles, which are generally used to describe how easily a crack can grow through a grain boundary, have been calculated for these short crack growth cases. However, the tilt and twist model is found to not be capable of explaining short crack transfer in the current work. This is due to the fact that multiple short cracks are present, and it is unclear when each of these short cracks initiated. Additionally, the morphology of the grain boundary cannot be defined correctly, because of the equiaxed microstructure and the lack of 3D information. **An alternative approach is suggested, which involves the calculation of an alignment factor. This factor describes the compatibility between specific slip systems in two grains, and is found to be high in case of crack transfer.** On the other hand, the effect of β and secondary α phase regions still remains unaccounted for, while these could act as barriers to short crack growth.

Finally, the effect of introducing a hold time at maximum load has been investigated by performing a limited number of dwell fatigue tests. In literature, this type of loading is generally found to lead to internal crack initiation in forged or rolled Ti-6Al-4V. However, **in the current work it is observed that dwell fatigue loading promotes surface crack initiation in drawn Ti-6Al-4V wires.** In some cases, multiple surface crack initiation locations can be identified, consisting of one or two facets. This different behaviour can be explained by the different crystallographic texture, because the phenomenon of load shedding is less pronounced in the absence of hard grains. Additionally, **the fatigue life, expressed as cycles to failure, is decreased by two to three orders of magnitude in comparison with regular fatigue tests.** However, the time to failure remains similar, and is even higher for some dwell fatigue tests. It is observed that there is an accumulation of strain during dwell fatigue. The maximum strain increases more rapidly in tests with 30 s load holds than it does in tests with 120 s load holds at maximum load. This behaviour can be understood by considering the strain evolution during the maximum and minimum load holds. Cold creep occurs at the maximum load, which causes an increase in strain. However, the strain rate decreases during each maximum load hold. During each minimum load hold, the strain slightly decreases, even though the minimum load is still a small tensile load. This recovery process leads to an increased initial strain rate during each following maximum load hold. This effect causes faster strain accumulation and a shorter fatigue life if the hold time at maximum load is 30 s instead of 120 s.

8.2 Suggestions for future research

This study has revealed that the internal crack initiation and facet formation behaviour in drawn Ti-6Al-4V wires is different compared to forged or rolled Ti-6Al-4V samples. The obtained knowledge can be used to provide suggestions for possible future research. The following topics could lead to new and interesting insights:

- Only a limited amount of samples with internal crack initiation have been obtained, due to the fact that the crystallographic texture of drawn wires leads to long fatigue lives and a relatively low probability of internal crack initiation. It seems advisable from a statistical point of view to produce more samples with internal crack initiation. Lowering the stress levels could increase the probability of internal crack initiation, but this would further increase the fatigue life. Therefore, the only sensible way to obtain more samples with internal crack initiation, is to perform ultrasonic fatigue tests at lower stress levels. Because the loading frequency is much higher during ultrasonic fatigue testing, the tests can be done within a reasonable timeframe.

- The results in chapter 6 show that the local texture affects the susceptibility to facet formation and the possibility of short crack growth. However, the analysis of both these observations has been restricted to two dimensions. A full 3D texture analysis could greatly improve the understanding of the influence of the local texture. This could be done by serial sectioning, which is rather time-consuming, or alternatively by 3D X-ray diffraction, which is faster but requires a synchrotron source and is still limited in resolution.[1]
- This work shows that, even in the absence of large orientation differences, facet formation and internal crack initiation is possible in Ti-6Al-4V. To the author's knowledge, this has not yet been taken into account in the computer models that have been described in literature, which only consider facet formation on basal planes of hard grains.[2, 3] It could be useful to implement this new knowledge into a finite element model, which can take into account both elasticity and crystal plasticity. Ideally, this should be coupled to experimental results, for example by using real texture data as input.
- This work provides new information that should be included in the search for an optimal texture for the fatigue performance of titanium alloys, as has been discussed for example by Bache.[4] However, determining this optimal texture is only useful if the texture can actually be controlled, which is generally rather difficult.[5] Recent developments in additive manufacturing show that this production process could possibly provide texture control to a certain degree. For example, the process parameters that are used during selective laser melting have been shown to affect the texture of parts made of an aluminium alloy[6] and a nickel based superalloy.[7] Local texture control of a nickel based superalloy has also been demonstrated during production by electron beam melting.[8] Therefore, it seems interesting to explore which textures can be obtained in Ti-6Al-4V parts that are produced by additive manufacturing, and to investigate how these textures affect the fatigue performance. Furthermore, if the local texture could somehow be controlled, texture gradients could be produced, which might also affect the fatigue behaviour.

- Finally, the phenomena of cold creep and recovery of creep that play an important role during dwell fatigue of Ti-6Al-4V, as discussed in chapter 7, are not yet fully understood. More research should be done to reveal the dislocation mechanisms that are causing this behaviour, and the possible involvement of hydrogen. Additionally, dwell fatigue tests with different hold times at maximum and at minimum load should be performed, in order to obtain a more comprehensive picture of the synergy between fatigue and creep in Ti-6Al-4V.

8.3 References

[1] H. Pirgazi (2015). *Wide Field 3D Orientation Contrast Microscopy.* Ph.D. Thesis, Ghent University.

[2] F.P.E. Dunne, D. Rugg, and A. Walker (2007). *Lengthscale-dependent, elastically anisotropic, physically-based hcp crystal plasticity: Application to cold-dwell fatigue in Ti alloys.* International Journal of Plasticity, 23(6), p. 1061-1083.

[3] M.H. Pourian, F. Bridier, P. Pilvin, and P. Bocher (2016). *Prediction of crack initiation sites in alpha Ti-alloys microstructures under dwell-fatigue using Cellular Automaton simulation method.* International Journal of Fatigue, 85, p. 85-97.

[4] M.R. Bache (1999). *Processing titanium alloys for optimum fatigue performance.* International Journal of Fatigue, 21, p. S105-S111.

[5] N.E. Paton, J.C. Williams, J.C. Chesnutt, and A.W. Thompson (1975). *The effects of microstructure on the fatigue and fracture of commercial titanium alloys.* AGARD Conference Proceedings, 185, p. 4-1 - 4-14.

[6] L. Thijs, K. Kempen, J.-P. Kruth, and J. Van Humbeeck (2013). *Fine-structured aluminium products with controllable texture by selective laser melting of pre-alloyed AlSi10Mg powder.* Acta Materialia, 61(5), p. 1809-1819.

[7] F. Geiger, K. Kunze, and T. Etter (2016). *Tailoring the texture of IN738LC processed by selective laser melting (SLM) by specific scanning strategies.* Materials Science and Engineering: A, 661, p. 240-246.

[8] R.R. Dehoff et al. (2015). *Site specific control of crystallographic grain orientation through electron beam additive manufacturing.* Materials Science and Technology, 31(8), p. 931-938.

Curriculum vitae

Joris Everaerts

Date of birth: January 30, 1989
Current address: Stevoortweg 26, 3540 Herk-de-Stad, Belgium
E-mail: joris.ev@gmail.com

Education background

PhD researcher 2012 – 2017
  Department of Materials Engineering (MTM)
  KU Leuven
  Belgium
  Thesis: "Fatigue crack initiation and facet formation in Ti-6Al-4V wires"

Master of Materials Engineering 2010 – 2012
  Department of Materials Engineering (MTM)
  KU Leuven
  Belgium
  Thesis: "Pulsed electric current sintering of tungsten composites for use as divertor material in a fusion reactor"

Academic bachelor of engineering 2007 – 2010
  Major in Chemical Engineering, Minor in Materials Engineering
  KU Leuven
  Belgium

Professional experience

Student research assistant July 2011
  Ceramics group, Department of Materials Engineering
  KU Leuven
  Belgium

Industrial internship Sep 2008, Sep 2009, Aug 2010
  Boflex nv
  Hasselt
  Belgium

List of publications

Peer reviewed journal papers

J. Everaerts, B. Verlinden, M. Wevers, “Investigation of fatigue crack initiation facets in Ti-6Al-4V using focused ion beam milling and electron backscatter diffraction”, Journal of Microscopy (2017), *Accepted for publication*

J. Everaerts, D. Gontcharov, B. Verlinden, M. Wevers, “The influence of load holds on the fatigue behaviour of drawn Ti-6Al-4V wires”, International Journal of Fatigue (2017), doi:10.1016/j.ijfatigue.2017.01.043

J. Everaerts, B. Verlinden, M. Wevers, “Internal fatigue crack initiation in drawn Ti-6Al-4V wires”, Materials Science and Technology (2016), vol. 32 (16), pp. 1639-1645

Full papers in international conference proceedings

J. Everaerts, B. Verlinden, M. Wevers, “The influence of the alpha grain size on internal fatigue crack initiation in drawn Ti-6Al-4V wires”, Procedia Structural Integrity (2016), vol. 2, pp. 1055-1062